THÈSE

En vue de l'obtention du

DOCTORAT DE L'UNIVERSITÉ DE TOULOUSE

Délivré par :

Institut National Polytechnique de Toulouse (Toulouse INP)

Discipline ou spécialité :

Dynamique des fluides

Présentée et soutenue par :

M. CARLOS MONTILLA ESTRELLA

le mardi 20 juillet 2021

Titre :

Electrostatic forces in fluidized bed reactors: numerical and experimental analysis

---

Ecole doctorale :

Mécanique, Energétique, Génie civil, Procédés (MEGeP)

Unité de recherche :

Laboratoire de Génie Chimique (LGC)

Directeur(s) de Thèse :

M. RENAUD ANSART

M. OLIVIER SIMONIN

Rapporteurs :

M. ALI OZEL, HERIOT WATT UNIVERSITY

MME CHRISTINE HRENYA, UNIVERSITY OF COLORADO AT BOULDER

Membre(s) du jury :

M. RODNEY FOX, IOWA STATE UNIVERSITY, Président

M. FOTOVAT FARZAM, UNIVERSITE DE TEHERAN, Membre

M. OLIVIER SIMONIN, TOULOUSE INP, Membre

M. RENAUD ANSART, TOULOUSE INP, Membre

Abstract

Fluidized bed reactors are one of the unit processes most commonly used in the industry. Plastic production, energy conversion, petroleum refining, and medicine manufacturing are just a few examples of the fields benefiting from this type of technology. Although important advances have been made towards the understanding and prediction of the dynamics of fluidized beds, many important questions remain unanswered. One of the most important open challenges is the study of the effects of electrostatic forces inside the reactor. This electrostatic interaction is known to be the cause of some important problems such as the accumulation of material at the reactor's wall, the risk of explosion, the perturbation of nearby electronic devices and even the complete loss of the fluidization state. Despite the important research efforts in the last few decades, many problems are still unsolved. Amongst these, we find the use of non-invasive measurements techniques to characterize the hydrodynamics effects of electrostatic forces inside the reactor; and the macroscopic mathematical modeling of the charging dynamics in the bed. These are the issues that this research program tries to address. As part of the project ANR-IPAF, this Ph.D. thesis aims at improving the understanding of the effects of electrostatic forces in a fluidized bed reactor. On the modeling front, we use the kinetic theory of rapid granular flow to derive the most complete Eulerian model of the particle electric charge dynamics in monodispersed gas-solid flow systems. In this work, we show how to lift some of the most restrictive hypotheses of previous models. We show that the transport equation for the mean particle electric charge can be obtained without assuming the shape of the particle electric charge probability density function. In addition to this, we also derive and close the transport equation for the second order terms: the particle charge-velocity covariance and the particle charge variance. Our results show that a correct modeling of the second order moments is needed in dilute or highly electrically charged regions. Given that this complete model also adds many more partial differential equations to be solved, we study possible simplifications. Two algebraic models, one neglecting the effects of the charge variance and one taking it into account are proposed. The former proved to be suitable in configurations with low electric potential energy. However, the latter must be use with caution as it can become nonphysical in high charged situations. Finally, a semi-algebraic model is also proposed to solve the important limitations of the coupled algebraic model. On the experimental front, we study the use of an ECVT system to characterize the dynamics inside the bed. We focus our attention to the image reconstruction algorithm. We test the traditional reconstruction algorithms found in the literature. However, our results show that they are, either too inaccurate, or too computationally expensive. For these reasons, we explore the use of a novel reconstruction technique using machine learning algorithms. In this thesis, we propose two different strategies to train a feed forward artificial neural network to handle the image reconstruction step in a ECVT device. The first strategy is based on CFD-generated data which is coupled with the sensitivity matrix model to deduce the capacitance measurements. The second approach relies exclusively on real experimental data and it seeks to reconstruct an image that could explain the capacitance measurements. Our results show that artificial neural networks can be as accurate as the best image reconstruction algorithms found in the literature. However, they can reduce the computational cost by several order of magnitudes.

Résumé

Les lits fluidisés représentent l'une des opérations unitaires les plus utilisées dans le génie des procèdes. L'industrie pétrolière, énergétique et pharmaceutique sont quelques exemples des domaines bénéficiant de cette technologie. Néanmoins, et malgré leur importance, certains aspects des lits fluidisés restent très mal compris. Parmi les défis qui restent à relever, nous trouvons les effets des forces électrostatiques dans la dynamique du réacteur. Il est bien connu que cette force inter-particulaires est à l'origine des nombreux problèmes industriels comme l'accumulation du matériel solide aux parois du réacteur, la perturbation des équipements électronique aux alentours, et même une perte complète de l'état de fluidisation. Malgré les nombreuses études consacrées à ce sujet, plusieurs questions restent toujours ouvertes. Parmi elles, nous trouvons l'utilisation des techniques des mesures non-intrusives pour caractériser le comportement du lit sous l'influence des forces électrostatiques; et la modélisation mathématique de la dynamique dans le réacteur d'un point de vue macroscopique. C'est dans cette perspective que ces travaux de recherches s'inscrivent. Dans le cadre du projet ANR-IPAF, cette thèse vise à améliorer la compréhension des effets électrostatiques dans la dynamique des lits fluidisés avec une approche numérique et expérimentale. Du point de vue de la modélisation, nous utilisons la théorie cinétique des milieux granulaires pour obtenir les équations gouvernant la dynamique de la charge des particules. Dans cette étude, nous modélisons non seulement l'équation de la charge moyenne des particules, mais aussi l'équation de la corrélation charge-vitesse et l'équation de la variance de la charge des particules. Nous proposons également deux modèles de fermeture algébriques pour les moments statistiques d'ordre trois. Cette modélisation représente, jusqu'à présent, la description Eulerienne la plus complète d'un écoulement gaz-particules monodisperse. L'analyse de ces équations nous permet d'établir les conditions dans lesquelles certains simplifications sont admissibles. Nous montrons qu'une modélisation correcte de la corrélation charge-vitesse est nécessaire dans les régions diluées pour bien pouvoir capturer le transport de charge dû aux mouvements aléatoires des particules. De la même façon, les effets de la variance de charge doivent être pris en compte lorsque l'énergie électrique du système est bien supérieure à l'énergie cinétique. Nous présentons aussi des simplifications possibles des modèles de fermetures des équations de transport avec leur plage de validité. Du côté expérimental, nous étudions un nouveau système de mesure non intrusive: l'ECVT. Nous nous focalisons sur l'un des points clé: l'algorithme de reconstruction d'image. Nous évaluons différentes algorithmes trouvées dans la littérature. Cependant, nos analyses montrent que les méthodes sont soit très imprécises soit très coûteuses en temps de calcul. Étant donnée ces limitations, nous nous intéressons à une nouvelle approche de reconstruction basée sur les techniques de l'intelligence artificielle. Nous proposons deux différentes solutions pour entraîner un réseau de neurones artificiels. La première approche s'appuie sur un apprentissage de type supervisée avec des données générées à partir des simulations numériques CFD. Tandis que la deuxième approche utilise une méthode d'apprentissage par renforcement en se servant uniquement des données expérimentales. Nous évaluons la qualité des ces approches avec des données simulées et des données réelles. Nos résultats montrent que les deux propositions sont aussi efficaces que les méthodes classiques de reconstruction. Mais elles peuvent réduire le temps de calcul par plusieurs ordres de grandeurs.

Acknowledgments

Although the achievement of a PhD is usually attributed to a single person, no research project is possible without the help and support of many people. So the next lines will be dedicated to all the people who helped me throughout the last 4 years.

First and foremost, I am extremely grateful to my supervisor Renaud Ansart for trusting me pretty much since the day we met more than 6 years ago and for having proposed me this incredibly interesting and rich research project. His advice, support, and goodwill will never be forgotten. I would also like to thank my co-supervisor, Olivier Simonin for sharing and teaching me part of his endless knowledge and experience. His expertise and patience reading my work were a crucial part of the success of this project. I would also like to express my gratitude to all the four members of my jury, professors Rodney Fox, Christine Hrenya, Ali Ozel, and Farzam Fotovat for taking the time to not only read my thesis but also for all the discussions, corrections, and insights they brought during the defense and the review process.

I would also like to thank all the different laboratories that were involved and helped me during my PhD. First of all, I'm very grateful to all the staff at the Chemical Engineering Laboratory of Toulouse (LGC), for welcoming and hosting me during these last 4 years. Special thanks goes to Emmanuel Cid for all his help and advice with the ECVT device and the image reconstruction problem. Also I would like to thank professor Stéphane Negny, for allowing us to form a collaboration between our laboratory and the Computer Science Research Institute of Toulouse (IRIT) that allowed us to open new research opportunities in a very interesting field like Artificial Intelligence. I would also like to express my gratitude to the technical staff of the LGC, more in particular to Jack Compain and Frédéric Da Costa, for all their help and support during the construction of the experimental setup. I would also like to mention my two teaching supervisors, professors Hugues Vergnes and Nataliya Shcherbakova for all their help and support during my teaching experience at ENSIACET. I would also like to thank the CoSiNus service, more in particular Hervé Neau and Maxime Pigou, of the Fluid Mechanics Institute of Toulouse (IMFT) for all their support and help with the code NEPTUNE_CFD. And finally, a big thank also goes to the Computer Science Research Institute of Toulouse (IRIT) and to David Simoncini for all his work, help and support with the artificial intelligence part of this research project.

Of course, a PhD project cannot be successful without the support of the colleagues one sees in a daily basis. It is for this reason that I would like to thank all the PhD students I had the pleasure to met. Given that making an extensive list risks of being too long and the danger of forgetting someone heavily outweighs any benefit, I will refrain from doing such thing. However, I do want to mention a few important names who stood out. First of all, a big thanks to Youssef and Florian, for welcoming and helping me during my first steps as

PhD student in their research group. Also big thanks to Claire for all the crazy ideas she had, but also, and more importantly, for her support during the last year of my PhD. And finally a huge thanks has to go to what became my LGC family: Eduardo, Florent and Michelle. Their companionship, jokes, help, support made this adventure more than worthwhile.

And last but not least, I would not be writing these lines if it weren't for the unconditional support that my family has given me during all these years. First of all, thanks to my mother and sister for their support and encouragement during this adventure in Europe. Also a big thanks to my father, for nourishing this passion I have for science and research and for all the time he took to help build the tools I needed to success. And finally a big thanks to my aunts and grandparents for their unconditional love and support during all these years.

Contents

1 Introduction **1**

1.1 Fluidized beds 1

1.1.1 What is a fluidized bed? 1

1.1.2 Fluidized bed parameters 3

1.2 Experimental techniques in fluidized beds 7

1.2.1 Probe-based measurement techniques 7

1.2.2 Gas pressure sensors 10

1.2.3 Particle tracking devices 10

1.2.4 Visualization techniques 12

1.2.5 Tomographic techniques 13

1.3 Mathematical modeling of fluidized beds 14

1.3.1 Direct Numerical Simulation (DNS) 14

1.3.2 Discrete Element Method (DEM) 15

1.3.3 Eulerian-Eulerian model 15

1.4 Effects of electrostatic forces in fluidized beds 16

1.4.1 Experimental research on the effects of electrostatic forces in fluidized beds 17

1.4.2 Modeling of electrostatic forces in fluidized beds 21

1.5 Thesis outline 24

2 Eulerian modeling of electrostatic force in mono-dispersed gas-solid flow 37

2.1 Introduction 40

2.2 Particle dynamics 42

2.2.1 Equation of motion for a single particle 42

2.2.2 Particle-particle collision dynamics 43

2.3 Eulerian modeling of electrostatic phenomenon 44

2.3.1 Boltzmann equation 45

2.3.2 General mean transport equation 46

2.4 Mean charge transport equation 48

2.5 Charge-velocity correlation modeling 51

2.5.1 Charge-velocity correlation equation 51

2.5.2 Charge-velocity correlation algebraic model 52

2.6 Electric charge dispersion 55

2.7 Triboconductivity effect 57

2.8 Conclusion 60

2.9 Acknowledgments 61

2.10 Appendix A. Integral collision coefficients 61

2.11 Appendix B. Electric charge covariance transport equation 62

3 Eulerian modeling of particle charge-velocity covariance and particle charge variance 67

3.1 Introduction 67

3.2 Particle velocity-charge covariance transport equation 67

3.3 Particle charge variance transport equation 70

3.4 Case of study 71

3.4.1 Dimensionless analysis 71

3.5 Two transport equations model 73

3.6 Three transport equation model 77

3.7 Coupled algebraic model 80

3.8 Semi-Algebraic model 84

3.9 Conclusions 84

Appendices **86**

3.A Algebraic gradient closure model for the third order moment $\langle \xi'_p c'_{p,i} c'_{p,j} \rangle$ . . . 87

3.B Algebraic gradient closure model for the third order moment $\langle \xi'_p \xi'_p c'_{p,i} \rangle$ 90

4 ECVT Image reconstruction algorithms for fluidized beds **95**

4.1 Experimental setup 95

4.2 Electrical Tomography Volume Capacitance 97

4.2.1 Physical principle and the sensitivity matrix approach 98

4.2.2 Image reconstruction algorithms for ECVT devices 100

4.3 Machine learning image reconstruction algorithms for ECVT systems 106

4.3.1 Artificial neural networks 106

4.4 CFD-Generated training database 108

4.4.1 Implementation 110

4.4.2 CFD Simulations 111

4.4.3 Training phase 112

4.4.4 Neural network evaluation 113

4.5 Experimental data-generated database 117

4.5.1 Experiments 118

4.6 Conclusion 123

5 Conclusions and perspectives **129**

General Bibliography **133**

Chapter 1

Introduction

1.1 Fluidized beds

1.1.1 What is a fluidized bed?

Let us imagine we have a container in which we put some granular material. The container also has a fluid inlet at the bottom and a fluid outlet at the top. If the solid density (ρ_p) is greater than the fluid density (ρ_f), the particles will settle at the bottom of the reactor, when the fluid is at rest. If we slightly increase the inlet velocity, the fluid will pass through the particles. These particles will not move while the upward force exerted by the fluid is less than the apparent weight of the particles. This state is called a *fix bed reactor* (figure 1.1a). If we keep increasing the fluid velocity, the upward force will eventually equate the apparent weight of the particles. At this moment, the particles will start moving around in a suspended state and the reactor is now called a *fluidized bed* (figure 1.1b). The term *fluidized* comes from the fact that, in this state, the dynamics of the system is very similar to a fluid-fluid system. For example, under some conditions, we can see the formation of clear distinguishable gas-only regions, very similar to a bubble column. Also, if we tilt the fluidized bed we would observe that the interface between the emulsion and the gas remains horizontal, exactly like a interface between air and water in a glass (Kunii and Levenspiel, 2003).

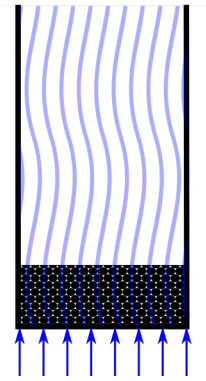

(a) Fix bed reactor illustration

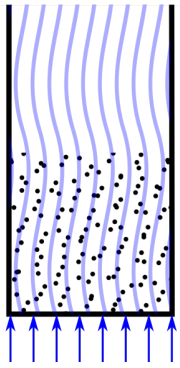

(b) Fluidized bed reactor illustration

Figure 1.1: Comparison between a fix bed reactor and a fluidized bed reactor

This constant movement of the solid phase inside the reactor creates an excellent mixing between the particles and the fluid. This leads to high mass and heat transfer coefficients. Moreover, this high quality mixing helps to maintain a constant temperature inside the bed. This greatly simplifies the control over the reactor making this technology easier to scale up. However, this same movement of particles is the cause of many of the downsides associated with this technology: erosion of the reactor's wall, entrainment of fines particles that need to be captured, and a poor control over the residence times of individual particles inside the bed. Overall, the benefits seem to overshadow the drawbacks, and fluidized bed reactors are used in many different industrial processes.

For example, they can be used as combustion reactors to generate heat. They are a particular interesting option to burn material with low calorific content or high moisture (Adanez et al., 2012; Koornneef et al., 2007). In the same process, fluidized beds can also be used as heat exchangers to recover part of the energy liberated in the combustion reactor (Zhang et al., 2012). Fluidized bed reactors are also a major actor in the gasification process (Xu et al., 2006). Here, solid fuel (either biomass or fossil fuel) is mixed with high temperature steam to generate a gas rich in hydrogen called syngas. This gas can later be burned to generate heat, or it can act as an intermediary to produce other products. Fluidized beds can be also extremely valuable in some green processes. For example, the high heat transfer coefficients in fluidized beds allow concentrated solar power plants to efficiently transfer the incoming heat flux to the solid particles. This allows to increase the working temperature to up 1000^{o}C (Almendros-Ibáñez et al., 2019)

Fluidization plays also an important role in the fabrication of the most consumed polymers such as polyethylene and polypropylene. In this process, a monomer in gaseous form is fed into a fluidized bed with a solid catalyst. This starts the polymerization reaction that forms the plastic granulates (Abbasi et al., 2019). In a similar process, fluidized beds can be used to break the complex oil molecules into smaller and more useful chains. This process, called cracking, requires to put in contact the gas containing the long hydrocarbon chains with solid particles that act as catalyst. Because the cracking reaction needs very high temperatures ($200 - 600\,^{o}$C) and it uses quite fine particles ($d_p \approx 60\,\mu$m), a fluidized bed reactor is a suitable solution for this process (Jiménez-García et al., 2011).

The pharmaceutical industry is also one of the great beneficiaries of fluidized bed reactors, especially in coating operations. Here, we use the fact that the particles are being suspended by the fluid to put a protective layer around them (Kulah and Kaya, 2011). In addition, the excellent mass and heat transfer properties of a fluidized bed make them a suitable option to dry solid granulates (Chandran et al., 1990). As we can see, fludized bed reactors are present in the most important fields of chemical engineering: plastic, pertroleum, pharmaceutical, etc.

1.1.2 Fluidized bed parameters

Particle types

One of the key parameters of any fluidization system is the types of particles used. Not all particles fluidize equally. Geldart (1973) reviewed the existent literature, and also conducted additional experiments to try to categorize the particles according to their fluidization behavior. He proposed that the particles can be divided into 4 different categories: A,B,C and D. Particles of type A are typically small particles and/or low density particles (less than $1400\,\mathrm{kg/m^3}$). They do not produce gas bubbles at the beginning of fluidization. But the solid circulation is still important despite this lack of bubbles. Particles with a diameter between $50\,\mu\mathrm{m}$ and $500\,\mu\mathrm{m}$ and density between $1400\,\mathrm{kg/m^3} < \rho_p < 4000\,\mathrm{kg/m^3}$ are categorized as B-type particles. For these particles, the presence of bubbles occurs almost immediately after fluidization starts. These bubbles are the main responsible for the solid mixing. C-type particles, also called cohesive particles, are very fine powder in which the cohesive forces (Van der Waals or electrostatic forces) are very strong. These particles are very hard to fluidize due to these inter-particular forces. We usually need some external mechanical system and/or chemical treatment to start and maintain a good fluidization state. Finally, D-type particles correspond to very large and/or heavy particles. Like B-type particles, we see the formation of bubbles even at low fluidization velocities. However, the bubbles rise at a slower pace. In fact the gas around the bubble rises faster than the bubble itself, unlike in B-type particles.

With these 4 definitions, and using already published data as well as in-house experiments, Geldart proposed a chart with boundaries between the particles types solely based on the particle diameter and density difference between the solid particles and the fluidization gas (figure 1.2). Although the Geldart's classification is widely known and used, it is by no means universal. Geldart's data only correspond to fludization at ambient conditions with air as fluidization gas. Adjustments need to be made to account for different gas conditions (Yang, 2007) or special particles properties (Yehuda and Kalman, 2020). Nonetheless, the 4 main categories proposed by Geldart seem to be still valid and only the transition between them might be affected in different conditions.

Pressure drop

One of the most studied characteristic relationships in a fluidized bed is the variation of the pressure drop across the bed as a function of the gas inlet velocity (superficial velocity). If we start with the fluid at rest and we slightly increase the velocity, the particles will not move because the gravity force is stronger than the upward forces. As we stated, this is a fix bed and the pressure drop across the reactor is equivalent to the pressure drop across a porous media. If we keep increasing the velocity, the pressure drop will also keep increasing, until

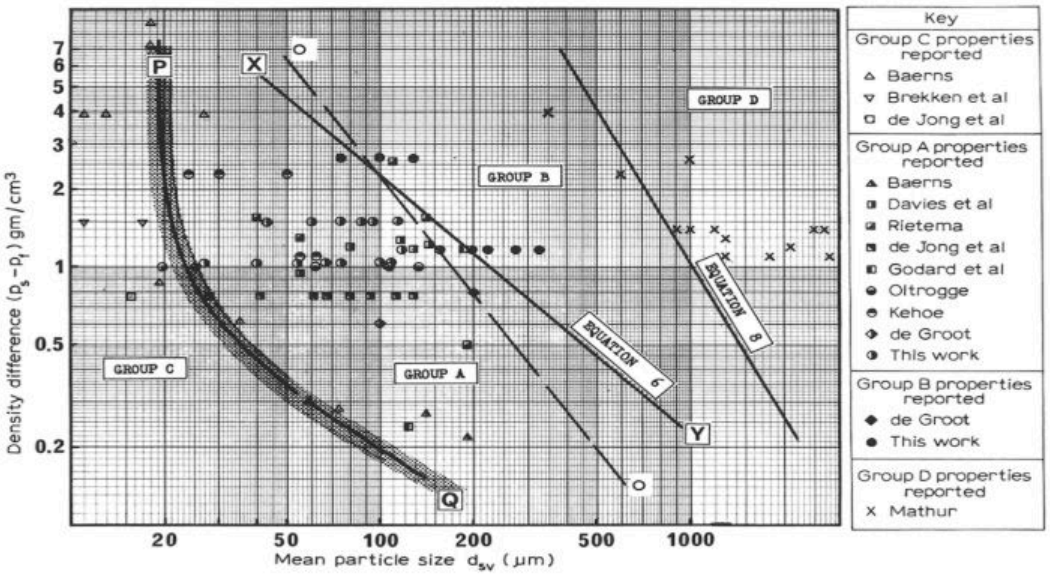

Figure 1.2: Original Geldart's chart proposing a powder classification according to their fluidization properties (Geldart, 1973)

the drag and buoyancy forces are equal to the gravity force. Here, the particles will start moving and they will be suspended by the fluid. The critical velocity at which we reach this moment is called the *minimum fluidization velocity* U_{mf}; this state is now called a fluidized bed. At this point, the pressure drop is roughly equal to the apparent weight of the particles (M'_{bed}) divided by cross sectional area of the reactor (A_{bed}). If we increase the fluid velocity even further, the bed height will increase and the global solid volume fraction inside the bed will decrease. Overall, the pressure drop will remain constant in this region. For very high gas velocities, the drag force become strong enough to start carrying the particles outside the reactor. This will decrease the solid material inside the bed and therefore reduce the pressure drop. Figure 1.3 shows an idealized version of the pressure drop plot as a function of the velocity. The actual pressure drop curve in a fluidized bed is more complex as it might depend on several factors like the shape of particles (Vollmari et al., 2016), the reactors dimensions (Vanni et al., 2015) and hysteresis effects (Weber and Hrenya, 2007).

Minimum fluidization velocity

As we have seen, the fluidization state is reached when the fluid velocity is strong enough to lift the particles in a suspended state. This critical velocity is called minimum fluidization velocity U_{mf}. Because U_{mf} signals the start of the fluidization state, it is very important to be able to accurately predict its value. For large columns, we can neglect the effect of the friction between the fluid and the walls (Ansart et al., 2017). In this case, a simple force balance inside the bed shows that, during fluidization, the pressure drop across the bed is

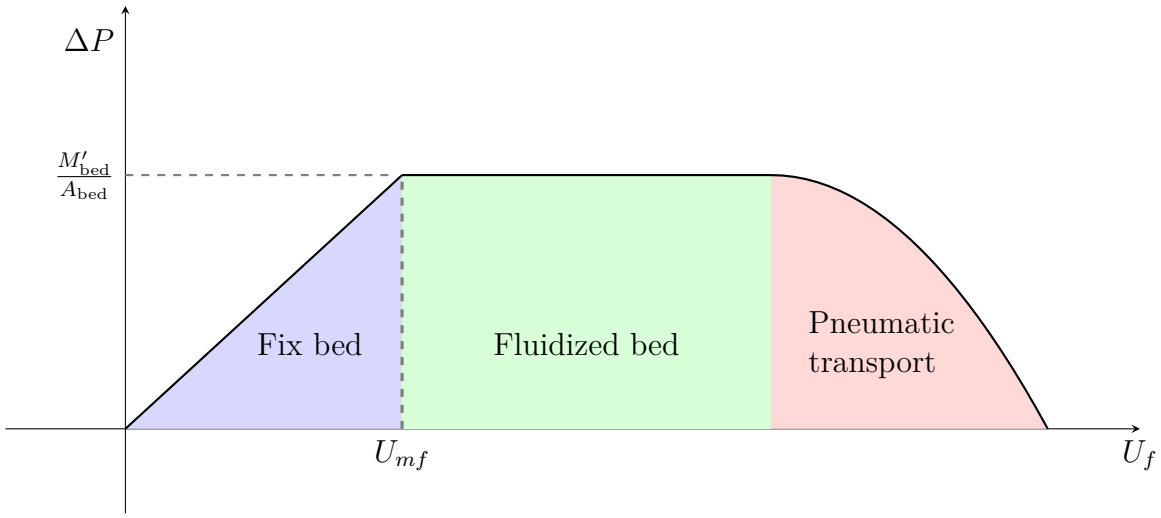

Figure 1.3: Idealized pressure drop curve as a function of the superficial velocity.

equal to the apparent weight of the particles divided by the cross sectional area of the reactor:

$$\Delta P \cdot A_{\text{bed}} = M'_{\text{bed}} \cdot g. \tag{1.1}$$

Where ΔP is the pressure drop across the bed and g is the gravitational acceleration.

Equation 1.1 can be rewritten as:

$$\frac{\Delta P}{L_{\text{bed},mf}} = \alpha_{p,mf} \left(\rho_p - \rho_f\right) g. \tag{1.2}$$

Where $L_{\text{bed},mf}$ is the height of the fluidized bed at the minimum fluidization state, and $\alpha_{p,mf}$ is the solid volume fraction inside the bed at the minimum fluidization state.

Because the minimum fluidization velocity sits at the boundary between a fix bed and a fluidized bed, we can use the theory of porous media to estimate ΔP. For example, Ergun and Orning (1949) proposed the following correlation between the fluid properties and the pressure drop in a fix bed of randomly packed spherical particles:

$$\frac{\Delta P}{L_{\text{bed},mf}} = \frac{150\mu_f}{d_p^2} \frac{\alpha_{p,mf}^2}{\left(1-\alpha_{p,mf}\right)^3} U_{mf} + \frac{1.75\rho_f}{d_p} \frac{\alpha_{p,mf}}{\left(1-\alpha_{p,mf}\right)^3} U_{mf}^2. \tag{1.3}$$

Here, μ_f is the fluid viscosity and d_p the particles diameter. Equating equation 1.2 with

equation 1.3, gives an expression whose only unknown is the minimum fluidization velocity.

This approach is, however, extremely simple and it does not take into account different important parameters such as the type and shape of particles or the influence of the fluid-wall friction. In practice, there is a large number of experimental research done for different types of particles under different conditions. Most of them proposed the use of correlations linking the minimum fluidization velocity with the particles and fluid properties. These correlations are usually written as:

$$Re_{mf} = f\left(Ar, \Phi, \alpha_{mf}\right). \tag{1.4}$$

Where Φ is the particles sphericity, and Ar is the Archimedes number, and Re_{mf} is the Reynolds number at the minimum fluidization state:

$$Re_{mf} = \left(1 - \alpha_{p,mf}\right) \frac{U_{mf} \rho_f d_p}{\mu_f}, \tag{1.5}$$

$$Ar = \frac{\rho_f \left(\rho_p - \rho_f\right) d_p^3 g}{\mu_f^2}. \tag{1.6}$$

For more details, Anantharaman et al. (2018) reviewed more than 150 different correlations found in the literature.

Fluidization regimes

The exact dynamics inside a fluidized bed reactor is extremely complex. However, there is an agreement that there are some common regimes present in almost all fluidization systems (Bi and Grace, 1995). These regimes are:

1. Smooth regime: Also called homogeneous fluidization, it occurs for liquid-solid systems or gas-solid systems with type A particles when the fluidization velocity is close to U_{mf}. It is characterized by the absence of any fluid bubble and the particles are homogeneously distributed in space. Despite the absence of bubbles in the emulsion, the particles do circulate inside the bed (Di Renzo and Di Maio, 2007).

2. Bubbling regime: Here some clear rising gas regions appear inside the bed. These structures look very much like air bubbles in a bubble column. For type B particles,

this regime starts almost after fluidization. But for type A particles this regime is observed when the superficial velocity reaches a critical value U_{mb} (minimum bubbling velocity $\approx 2U_{mf}$). The characteristics of the bed (transfer coefficients, or solid mixing) are mostly controlled by the bubble's dynamics. (Grace et al., 2020).

3. Slug regime: As we increase the gas superficial velocity in a bubbling fluidized bed, the bubble size will also increase. At some point the bubbles will be as big as the column diameter. This state is called slug regime. This condition is usually undesirable, as the solid mixing is impacted negatively because all the gas phase is concentrated in these slug regions (Baeyens and Geldart, 1974).

4. Turbulent regime: Further increase of the gas velocity after the slug regime (if it occurs) will lead to a fluidization dynamics where the bubbles or slugs break and coalesce continuously. Because of this, the void regions inside the bed have an irregular shape and they will burst violently in the free surface of the bed (Bi et al., 2002; Yerushalmi and Cankurt, 1979).

1.2 Experimental techniques in fluidized beds

Experimental techniques to characterize the hydrodynamic behavior in fluidized beds can be divided into two categories: intrusive and non-intrusive approaches. The first type involves the insertion of probes inside the reactor to directly measure the quantity of interest. This approach, however, can potentially disturb the internal dynamics of the flow, especially if many probes are inserted at the same time. Non-intrusive techniques, on the other hand, rely on the information gathered by devices placed outside the reactor like: cameras, tomographs, pressure sensors, radiation sensors, etc. The data obtained from these devices is then used to try to infer the bed's properties.

1.2.1 Probe-based measurement techniques

Probes are very common devices used to obtain local measurements inside the bed. Nowadays, we can find many different probing techniques: optical probes, capacitance probes, electrostatic probes, laser Doppler probes, extraction probes, etc. They allow us to obtain accurate data in very specific regions or locations of our reactor. Probes are also relative simple and small devices requiring little instrumentation to function. Their presence inside the bed can, however, impact the local dynamics of the bed making the data harder to interpret and extrapolate. There is also a risk of breaking the probe inside the bed due to the large number of particles colliding with it. Despite these shortcomings, they are still largely used to characterize the internal dynamics of fluidized beds.

Optical probes have one light emitting tip and one light receiving tip. The amount of light captured in the second tip is a function of the local solid volume fraction (figure 1.4). A low solid volume fraction zone is basically transparent, while a high solid volume fraction zone is basically opaque. This type of probes has been extensively used to measure the local solid volume fraction in a fluidized bed (Johnsson and Johnsson, 2001). They can also be combined in pairs to deduce key bubbles parameters, like size and rising velocity (Mainland and Welty, 1995; Rüdisüli et al., 2012). Optical probes are, however, very sensitive to particles deposition on the surface of the emitter or sensor (Werther and Hage, 1995).

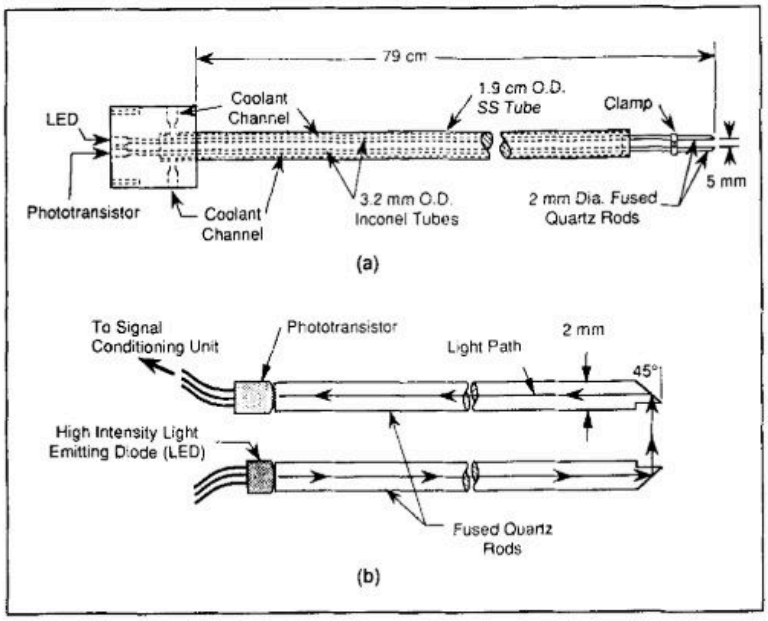

Figure 1.4: Optical probe diagram (Mainland and Welty, 1995).

The capacitance probe is similar to the optic probe, but instead of measuring the local opacity, it measures the local capacitance between the two tips (figure 1.5). This local capacitance is direct function the local permittivity which is function of the local solid volume fraction. Similarly to the optical probe, the capacitance probe can be used to monitor the local solid volume fraction of particles (Hage and Werther, 1997; Wiesendorf and Werther, 2000). This type of probe is more resilient against particle deposition in their surface. However, the capacitance measurements are sensitive to electromagnetic noise.

Electrostatic probes take advantage of the fact that there is a electric charge transfer when a particle collides with the tip of the probe (figure 1.6). This property can also be used to distinguish the emulsion phase from a bubble allowing us to deduce essential parameters like the bubble rising velocity (Li et al., 2020). An important advantage of electrostatic probes is that they can also be employed to measure the electric charge of particles without stopping the reactor or extracting samples from the bed (He et al., 2015).

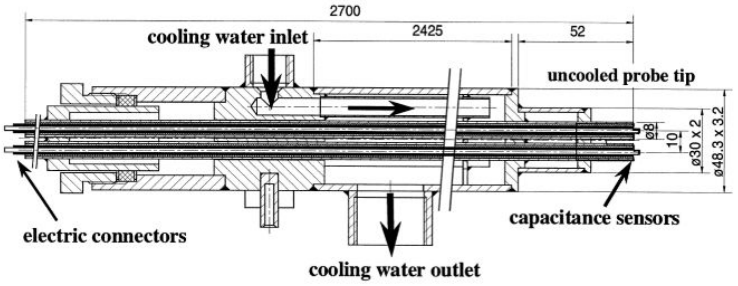

Figure 1.5: Capacitance probe diagram (Wiesendorf and Werther, 2000).

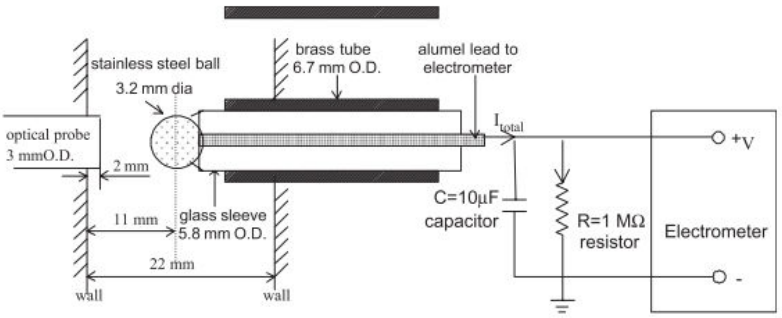

Figure 1.6: Electrostatic probe diagram (Chen et al., 2003).

All the previous probes are suitable for measuring the local presence of particles, however little information can be extracted about their dynamics. To solve this problem, Laser Doppler Probes have been developed. This device sends two beams of light into a region of the bed (figure 1.7). This light will be reflected by the particles in the region. However, the wave length of the reflected light will be shifted due to the Doppler effect. This information allows us to calculate the velocity of the particles (Werther et al., 1996). This technique is, nonetheless, restricted to the dilute regions of the bed.

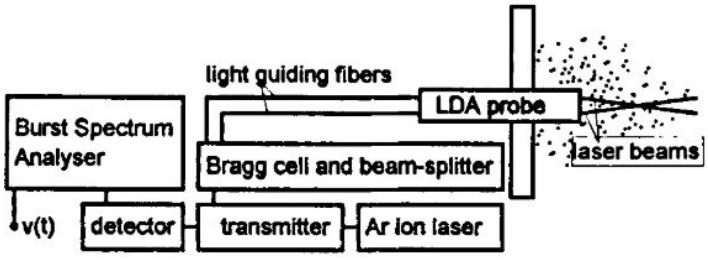

Figure 1.7: Laser Doppler probe diagram (Werther et al., 1996).

1.2.2 Gas pressure sensors

Gas pressure sensors are one of the most commonly used device to monitor the state of a fluidized bed. They are cheap and relatively easy to install at the walls of the reactor. However, extracting meaningful information from the pressure signals is far from straightforward. Pressure fluctuations can have different causes: the passage of a bubble, the local turbulence of the gas phase, or even the formation, breakup and coalescence of bubbles far away from the pressure sensor (Fan et al., 1981; Punčochář and Drahoš, 2005). Despite these challenges, pressure signals have been used to obtain important information about the dynamics and properties of the reactor such as: the minimum fluidization velocity (Punčochář et al., 1985), the bed's height (Zhang et al., 2008b), the current fluidization regime (Lee and Kim, 1988; Trnka et al., 2000), bubble's properties (Liu et al., 2010; Van Der Schaaf et al., 2002).

1.2.3 Particle tracking devices

Another approach to understand the dynamics of the solid phase is by tracking the position of one, or multiple, particles inside the bed. These techniques are based on the insertion of a radioactive tracer particle inside the bed. The motion information of this individual particle can provide valuable information to understand the solid mixing patterns inside the reactor. The main disadvantage of these techniques is that they rely on radioactive material. Therefore, special care is needed to ensure the safety of the installation. We also need to ensure that the shape and density of the tracer particle are similar to the bulk material.

Two main approaches have been developed so far: the Radioactive Particle Tracking system (RPT) and the Positron Emission Particle Tracking (PEPT). The RPT system relies on detecting the intensity of the gamma rays emitted by the radioactive tracer. Using multiple sensors placed around the reactor, we can determine the location of the tracer (figure 1.8). The main drawback is that RPT devices require a calibration step for every new geometry or material, because the γ rays are attenuated by the medium. This technique has allowed us to accurate map not only the solid mixing (Fotovat et al., 2015) in a fluidized bed, but also very important and detailed quantities such as the kinetic stress tensors and the turbulent kinetic energy (Ali et al., 2017; Kiared et al., 1997; Larachi et al., 1995; Rasouli et al., 2015)

The second approach is called the Positron Emission Particle Tracking (PEPT). This time, we use a radioactive tracer undergoing a β^+ decay. This type of radioactive decay produces a positron that will be annihilated as soon as it collides with a nearby electron. By energy and linear momentum conservation, the positron-electron annihilation produces two γ rays traveling in opposite directions. Detecting this pair of γ rays allows to infer the line in which the tracer particle must lie. This line is called Line of Response (LOR). If we detect a second pair of γ rays, we know that the particle is located near the interception of

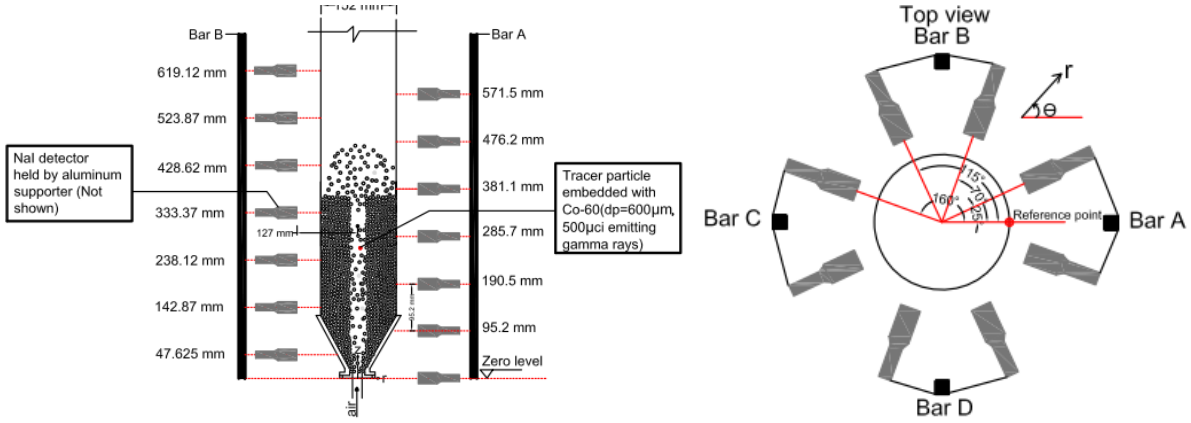

Figure 1.8: Radioactive Particle Tracking system (Ali et al., 2017).

the two measured LORs (figure 1.9). The main advantages of the PEPT technique is that calibration is not needed and the tracer particle can be chosen from the bulk material with the addition of a radioactive coating. However, the PEPT sensors and equipment are bigger and more expensive. Similarly to the RPT, this approach has been applied to fluidized beds to deduce key dynamic parameters of the solid phase: the motion patterns, mean velocity field, the particle velocity distribution, etc (Langford et al., 2016; Parker, 2017; Parker et al., 1993; Van de Velden et al., 2008).

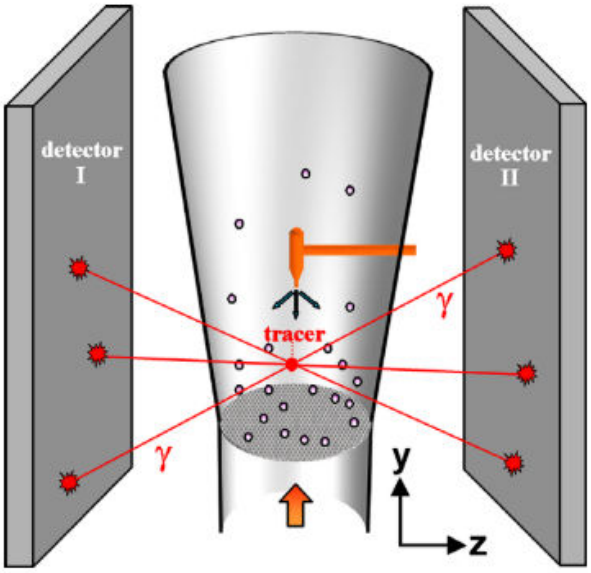

Figure 1.9: Positron Emission Particle Tracking system (Depypere et al., 2009).

1.2.4 Visualization techniques

If the fluidized bed column is transparent, an intuitive measurement approach is to record the dynamics of the bed with a camera and to use image analysis techniques to extract all the information we can. A simple setup consists in taking high resolution images of the dynamics and extracting flow patterns and bubble properties (figure 1.10). This exact same procedure has been employed to obtain important information about the bubble size and aspect ratio distribution, and breakup dynamics (Busciglio et al., 2008; Movahedirad et al., 2014).

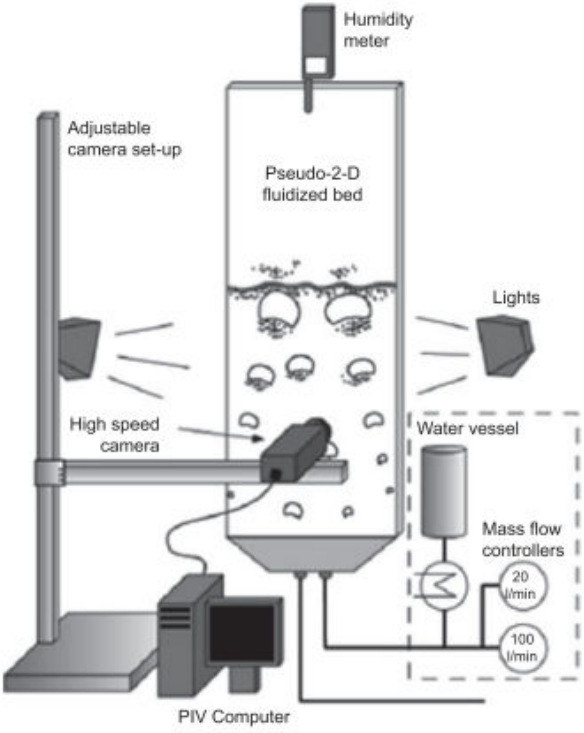

Figure 1.10: Image analysis technique (Movahedirad et al., 2014).

However, more data can be obtained if we take into account the temporal dimension of a series of images. This is the objective of the Particle Image Velocimetry (PIV) technique. In this approach, the cross-correlation between two consecutive images allows to compute the distance traveled by particles between the two images. Then, the velocity is calculated by dividing by the time delay between the two images. This strategy has been used to calculate not only the particles mean velocity, but also the particle shear stresses and turbulent kinetic energy (Dijkhuizen et al., 2007; Kashyap et al., 2011). The main disadvantage of the visualization techniques is the need for an optically transparent medium, which cannot always be achieved. Even more, even with a transparent column, we can only gather information about visible phenomena near the walls. The dynamics in the center of a fluidized bed is much harder to obtain.

1.2.5 Tomographic techniques

Tomography is a imaging technique that aims at reconstructing the internal composition of a object by measuring the effects of passing some wave through the body of the object. Tomographic devices rely on a series of sensors placed around the volume of interest. A wave is then emitted and forced to pass inside the domain. The sensors record the perturbations on the wave produced by the medium. This data is then used to deduce the internal properties of the volume inside the tomograph. Tomography can be categorized into two classes: hard-field tomography and soft-field tomography. In the first category, the perturbations measured only depend on the path between the emitter and the sensors. In the soft-field tomography, the perturbations are a function of the entire domain. This makes this approach harder to implement and it is, in general, less accurate.

Examples of hard field tomography are the X-ray or γ-ray tomography. In both cases a source emits a beam of either X or γ rays from one side, and sensors located on the other side measure the attenuation suffered by the beam (figure 1.11). This data is then used to reconstruct the volume fraction distribution along the line connecting the emitter and the sensor. By changing the position of the source and the sensors, we can reconstruct a 3D representation of the internal composition of the volume. These techniques have been used to obtain a more global representation of the solid volume fraction distribution inside a fluidized bed. But also, they have allowed us to observe more complex parameters/dynamics such as the bubble's shape and the coalescence between bubbles (Efhaima and Al-Dahhan, 2015; MacCuaig et al., 1985; Mudde, 2010a,b).

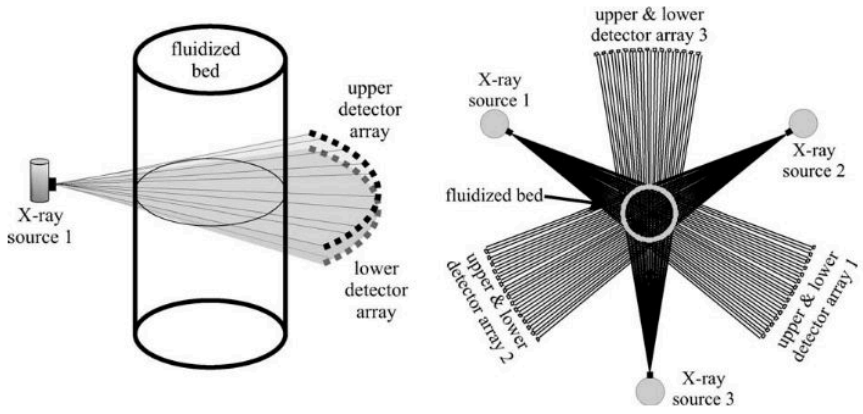

Figure 1.11: X-ray tomography system (Mudde, 2010b).

In the soft field tomography class, we find techniques such as the Electrical Capacitance Tomography (ECT) or the Electrical Resistance Tomography (ERT). They have a very similar operating principle: a series of electrodes are placed around the volume of interest and a small electric field is sent through the domain (figure 1.12). Using this electric field, we measure either the inter-plate capacitance or the inter-plate conductivity. This data allows us to

reconstruct an approximated image of the solid volume fraction distribution inside the bed. In comparison to the X or γ ray tomography, the ECT and ERT work with lower energy fields which makes them much safer and easy to install. However, we lose accuracy in the reconstructed image.

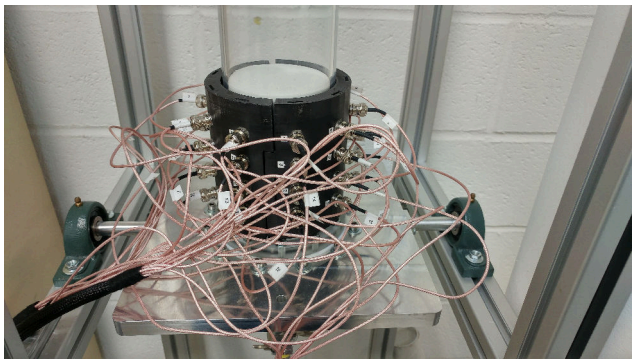

Figure 1.12: ECVT system around a laboratory scale fluidized bed.

1.3 Mathematical modeling of fluidized beds

By their very nature, fluidized beds involve physical phenomenon with very distinct length scales: particle-particle interactions ($\sim \mu$m); particle clusters and gas bubbles ($\sim$ cm); and macroscopic motions inside the reactor ($\sim$ m) For this reason, different mathematical modeling approaches have been developed, from an accurate representation of the dynamics at the particle scale to a macroscopic statistical representation of the phases involved.

1.3.1 Direct Numerical Simulation (DNS)

The Direct Numerical Simulation (DNS) is the most accurate modeling of a gas-solid flow system. In this approach, we solve for the smallest structures in the system. The fluid flow around each particle is accurately computed and the force exerted by the fluid on the particle is calculated using the fluid stress tensor at the surface of the particle. The high degree of precision required by this approach makes it very computationally expensive. The current computer power available is only enough to simulate configurations with only a few thousands of particles (Ozel et al., 2017).

Despite this limitation, DNS has proven to be a very valuable tool to obtain very detailed and accurate information about the dynamics of gas-particle flows. This approach has been used to validate and propose closure laws required by the other modeling strategies (Beetstra et al., 2007; Lu et al., 2017). A unique advantage of this approach is that it allows us

to simulate complex configurations like non-spherical particles (Zastawny et al., 2012) or non-smooth walls (Milici et al., 2014).

1.3.2 Discrete Element Method (DEM)

The discrete element method is based on the point-particle assumption to model the solid phase. In this approach, the particles are tracked individually and their positions are calculated using Newton's second law of motion. However, in the DEM method, we do not solve for the flow field around each particle. Instead, the coupled interactions between the particles and the fluid are taken into account using closure laws (Traoré et al., 2015). This reduces the computational costs compared to the previous approach, but it requires an accurate modeling of these closure laws to achieve meaningful results.

With the current computer power, we can simulate laboratory-scale systems containing many more particles than any DNS simulation. This allows us to study in fine detail important phenomena of larger systems like: particle interaction with the flow eddies (Ernst et al., 2019), the particle-wall interactions (Li et al., 2016), and the particle cluster formation (Zhang et al., 2008a). The DEM approach is very useful as it can be combined with particle tracking experimental technique to propose and validate closure laws for other modeling approaches (Kriebitzsch et al., 2013; Link et al., 2005). Although this strategy is very powerful, the computational cost is still too high to tackle industrial size problems.

1.3.3 Eulerian-Eulerian model

The last approach we will mention is the Euler-Euler model, also called the Two-Fluid Model (TFM). This is a hybrid approach, where the fluid phase is treated using the phase-averaged Navier-Stokes equations, and the solid phase is modeled using the kinetic theory of granular flows (Zhang and Prosperetti, 1994). In this model, the individual particles are not longer tracked. Instead, we take interest in the statistical moments of the probability density function of particles. This can give us crucial information such as the solid volume fraction, the mean particle velocity, the mean particle electric charge, the mean particle temperature, etc. Depending on the accuracy required, we can easily extend this to the higher order moments such as: the variance, covariance, skewness, etc.

Given that the particles are not longer individually followed, the TFM approach scales very well to large problems. Combustion reactors (Wang et al., 2014), gasification processes (Liu et al., 2013) and polymerization fluidized beds (Schneiderbauer et al., 2015) are some examples that shows the success and acceptance of the TFM model. On the negative side, this approach requires very complex and accurate closure models for many terms (Boëlle

et al., 1995; Sakiz and Simonin, 1999; Simonin et al., 2002). This model is further explained in chapter 2.

1.4 Effects of electrostatic forces in fluidized beds

Due to the numerous solid-solid interactions present in a fluidized bed, the particles can get electrically charged (Forward, 2009). The two main mechanisms responsible for the charging of the solid particles are: the collision of a particle with a charged or neutral wall (figure 1.13), or the collision between particles with different electric charge (figure 1.14). This electrification of the solid phase adds an extra particle-particle force due to the electromagnetic interaction between the particles. It is well known, since several decades ago, that this effect can have a significant impact in the dynamics and properties of the fluidized bed (Miller and Logwinuk, 1951; Wolny and Kaźmierczak, 1993). Fotovat et al. (2017) examined the magnitude of the electrostatic force compared with the other two major forces: drag and gravity. Their findings showed that the electrostatic force can be of the same order of magnitude as the other two for small particles.

(a) Particle-wall charge transfer. (b) Particle-wall charge separation.

Figure 1.13: Tribocharging of a solid particle due to the collision with a wall.

The presence of electrostatic forces could be undesirable in fluidized bed reactors. For example, in a polyethylene reactor, the particles might adhere to the walls due to electrostatic

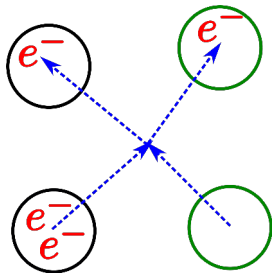

Figure 1.14: Tribocharging of a solid particle due to the collision with a charged particle.

attraction. If an exothermic reaction takes place inside the reactor, these particles will create hot regions that could force the complete shutdown of the reactor (Hendrickson, 2006). The presence of electrically charged particles can also be a safety concern. If the electric field generated by the particles is strong enough, a spark might occur which could lead to an explosion (Choi et al., 2011). However, electrostatic forces are not always a problem. They can be used to our advantage, like modifying the bed's dynamics to enhance the mass or heat transfer coefficient (Kleijn van Willigen et al., 2005). Also, the difference in electric charge between the particles can be exploited in conjunction with an external electric field as a separation technique (Calin et al., 2008).

However, due to their nature, research in electrostatic force is a highly complex task. From an experimental standpoint, the handling and transport of particles must be extremely careful, otherwise the particles might get charged before the experiment begins of after it ended. Also the net electric charge of particles it is very low, and we require very accurate measurement techniques. These problems have been the cause of reproducibility issues or even contradictory results. From a modeling point of view, the triboelectric charging is a microscopic phenomenon occurring at the particle scale. And the mechanisms involved in the transfer of charge between two colliding solid surfaces it is still up to debate. Nevertheless, and despite all these difficulties, very important advances and discoveries have been made in the last 70 years. In the following sections, we present a non-exhaustive historical summary of the advances in research of electrostatic forces in fluidized bed.

1.4.1 Experimental research on the effects of electrostatic forces in fluidized beds

The effects of electrostatic charges in fluidized beds were first recognized in the literature at the beginning of the 50s. A study on the heat transfer properties of fluidized beds revealed some, at first, inconsistent results for some types of particles (Miller and Logwinuk, 1951). In particular, their data showed that, contrary to all other particles tested, the heat transfer coefficient increased with particle diameter for silica gel powder. The cause of this discrepancy was attributed to the presence of electrostatic forces in the fluidized bed. More precisely, the silica gel particles adhere to the walls of the reactor adding an extra thermal resistance to the system, but bigger particles allow more inter-particle space, increasing the transfer surface area. These findings inspired the same authors to build a simple setup to assess the presence of electrostatic charges in the system. They proved that the transport of silica gel particles was able to electrically charge a copper tube. This work was one of the first to, not only point out the presence of electrostatic forces in gas-solid configurations, but also to highlight that they can modify the properties of a fluidized bed.

After this work, the presence of electrostatic effects was acknowledged and studied by many different researchers. Several works showed that the particles adhering to the walls

and sensors can become a serious problem for the experimental devices (Wen and Hashinger, 1960; Capes and McIlhinney, 1968). However, they all reported that increasing the fluidization gas humidity greatly diminished or completely solved this issue. It is also around these times where we find the first work dedicated to the characterization of the electrification phenomenon in fluidized beds. Ciborowski and Wlodarski (1962) introduced a probe in a fluidized bed to measure the electric potential in different conditions. They showed that high fluidization velocities or low gas humidity enhance the build up of high electric potentials inside the reactor. They also observed that the particle adhesion phenomenon is more pronounced when the voltages are higher. Ganzha (1967) also measured the voltage inside a fluidized bed using different column materials. They concluded that the electrification phenomenon must come from the contact between the walls and the particles. And the level of electrification is highly dependent on both materials.

Although these studies proved that the electrostatic force was indeed present inside a fluidized bed, little was still known about the effects they could have in the dynamics of the reactors. One of the key aspects that was still poorly understood was the role of humidity as a limiting factor for the charge build up. Many researchers reported that high humidity decreased the impact of electrostatic forces, however, no work in the literature formally addressed this problem. Bafrnec et al. (1972) confirmed that the humidity in the fluidization gas forms a small layer of water at the surface of the particle which increases the surface conductivity. If we consider a single solid particle as a capacitor, then increasing its surface conductivity will prevent the electric charge to accumulate in the particle. During this decade, we see also the first academic studies using the electrification phenomenon for control method or separation techniques. Inculet et al. (1977) and Kiewiet et al. (1978) took advantage of the fact that particles of different sizes get different electric charge, and they used an external electric field to separate them. Another favorable application of the electrostatic phenomenon was proposed by Colver (1977) who applied an external electric field to the fluidized bed to control the bubbles' size.

To this moment, the presence of an electrostatic phenomenon was acknowledged by the scientific community, but still no real measurement of the electric charge had been published. Tardos and Pfeffer (1980), however, introduced the use of a Faraday cup as an option to measure the total electric charge of the bulk material. They confirmed that the solid particles were indeed electrically charged of the order of a few microcoulombs per meter square. The intensity of the charge increased with the gas velocity but it decreased with the gas humidity. They also showed that the electrostatic probes must be used with caution, as they might not accurately reflect the particle electric charge. This is because the electric current generated on the probe depends on the particle electric charge and the relative velocity between the probe and the particle. This idea of a Faraday cup was also used by Fasso et al. (1982). They placed an extraction probe to capture and measure the electric charge of particles in the freeboard region of the fluidized bed. Their data showed that, like for the particles inside the bed, the particles in the freeboard region are more electrically charged for higher fluidization velocities. Baron et al. (1987) extended this analysis and studied the entrainment flux in the

freeboard region. They concluded that, for silica sand particles, the effect of electrostatic forces over the entrainment flux disappears for humidity rates higher than 30%, regardless of the fluidization velocity.

Although the Faraday cup was a useful method to directly measure the global electric charge inside the bed, it cannot measure the charge of an individual particle. This was the objective of the study conducted by Wolny and Kaźmierczak (1989). They used small air jets to eject and isolate single particles and then, they recorded their trajectory in a fixed electric field. This allowed them to determine the electric charge of the particle. They showed that, in a polystyrene bed, the particles do not necessarily charge with the same polarity. There are negatively and positively charged particles. They also confirmed that adding antistatic agents, like sodium chloride, does reduce the tribocharging effect in the solid phase. Another novel study on polystyrene particles was performed by Gajewski (1985). They placed a series of metallic rings around the bed in order to measure the electrification phenomenon at different heights. Their data highlighted that the charge generation occurs at the walls of the bed. Then the electric charge is transported to the rest of the domain by the motion of the particles or by the charge transfer due to particle-particle collisions.

During the last decade of the 20^{th} century, the research focused mainly on gathering a deeper understanding of the effects of electrostatic phenomenon in fluidized bed. Briens et al. (1992) continued the research on the elutriation phenomenon. They observed that, for polyethylene particles, the electrostatic forces greatly reduces the entrained flux by up to 2 order of magnitudes compared with the neutral case. They also showed that the particle size distribution of entrained particles does not vary significantly between the neutral and the charged case. During that same period, Wolny and Kaźmierczak (1993) studied the dependency between U_{mf} and U_{mb} as a function of the electrostatic forces. Their findings highlight that the electrostatic effects induce an important hysteresis effect in the pressure drop plot. And both U_{mf} and U_{mb} are higher for charged particles compared to their neutral case. Later, Zhang et al. (1996) used Laser Doppler Velocimetry (LDV) to measure the velocities of particles in a dilute system. In particular, they revealed that the electrostatic force does not modify the Maxwellian particle velocity probability density function.

From the years 2000s, we can see that the electrostatic forces became a very important topic in the studies of fluidized beds, as the number of publications increased. During this period, we witnessed the development of new measurements techniques that allowed us to gain a deeper understanding of the tribocharging phenomenon. Zhao et al. (2003) developed a sampling method of several Faraday cups vertically aligned to separate the particles by their size and then measure their electric charge. They showed that, for their polymer powder, there is a bipolar charging phenomenon taking place. The small particles charged negatively while the large particles were positively charged. In addition to this result, Mehrani et al. (2005) designed an online measurement system where the fluidized bed column forms part of a big Faraday cup. They concluded that, in an initially neutral poly-disperse system, the fines particles will get negatively charged and then leave the system. By the charge

conservation law, this means that the particles left in the bed must be positively charged. This system also allowed them to confirm that the gas-particle contact does not charge the solid phase; and the charging phenomenon is exclusively due to solid-solid contacts. Sowinski et al. (2009) developed a Faraday cup embedded inside the windbox to collect all the particles immediately after fluidization. This reduced the effect of tribocharging due to manual handling. Bi et al. (2007) adapted an electrostatic probe to monitor both the electric charge and the local hydrodynamics simultaneously based on the normalized instantaneous and time average signals. Chen et al. (2003) also developed a model that allowed them to extract the particle charge per unit of mass using a single electrostatic probe.

During this period, some researchers also tried to expand the experimental work to more complex configurations. Moughrabiah et al. (2009) studied the impact of gas pressure and temperature in charge generation. They concluded that the pressure contributes to the electrification of the bed, while temperature seems to be a neutralizing factor. We also found the first study involving gas-liquid-solid fluidized beds (Alissa Park and Fan, 2007). Similarly to the gas-solid systems, they concluded that particle-particle interactions are responsible for the electrification of the bed. They also showed that the addition of fines particles could be used to decrease the electric charge of the system.

The last decade of research in electrostatic in fluidized bed has brought us a deeper understanding of the physical phenomena taking place inside the bed. Sowinski et al. (2012) studied the wall sheeting effect for particles of different sizes. Their experiments showed that the smaller particles are more prone to attach to the wall. They also revealed that the magnitude electric charge of the particles stuck on the wall is much higher than the charge of particles in the bulk. Later, Salama et al. (2013) investigated in detail the electric charge distribution of the particles adhered to the wall. They found that, in fact, we have particles of different polarities in this region. This led them to hypothesize the following mechanism for the wall sheeting phenomenon: due to electric charge transfer between the wall and the particles, the wall acquires certain polarity. Then, the wall will attract particles of the opposite sign, which makes the first layer of particles to attach to the wall. This layer of particles will now attract particles of the opposite sign and this forms a second layer of particles. This process will continue forming consecutive layers of positive and negative particles, until the fluid and gravity forces are stronger than the electrostatic attraction. Further and more detailed studies seem to support this theory (Song and Mehrani, 2017; Song et al., 2016).

Dong et al. (2015) also investigated the dynamics inside the bed, but more focused in their effects on the gas dynamics. Using electrostatic probes, pressure sensors and Faraday cups, they showed that the more the particles are charged, the smaller the size of the bubbles. According to their findings, the particles inside the bed are mostly charged with the same polarity. This makes all the particles repeal each other, leaving less space for the bubbles to develop. Yang et al. (2016) also studied the presence of agglomerates inside the bed. As we previously discussed, the electrostatic force promotes the formation of wall fouling that could

dangerously fall into the reactor. Their study showed that these falling agglomerates, not only disturb the hydrodynamics of the bed, but also they also change the tribocharging dynamics of the particles. Most of the experimental studies in fluidized bed focused on initially neutral particles that get charged via the fluidization process. However, Manafi et al. (2019a,b) studied the effects of the fluidization of pre-charged particles. In particular, they showed that the minimum fluidization velocity of already charged particles is higher compared to the initially neutral case. They also observed that the bubble size could be smaller when the particles are already charged. This revealed that the initial fluidization condition can play an important role. More recently, Nasro Allah (2019) conducted an extensive analysis, coupling in-house experiments with 3D numerical simulations. They studied the charging dynamics for different types of particles under different fluidization conditions. Their results show that the temporal charging dynamics follows an exponential law. They also confirmed that the electric charge of particles stuck to the wall are several order of magnitudes higher than the charge of the bulk. This data allowed them to simulate a 3D laboratory scale fluidized bed reactor showing that indeed the electric charge of particle has a significant impact on the macroscopic quantities of the bed such as the solid volume fraction, mean particle velocity and particle agitation.

All this shows the evolution of more that 70 years of experimental research in the electrostatic effects in fluidized beds. From a mere qualitative acknowledgment of the presence of an electrostatic phenomenon, to accurate macro and microscopic measurements of the most important parameters of the fluidized bed under myriad of different conditions. We have now a good understanding of the triboelectric effects inside a fluidized bed. We know why the particles inside a fluidized bed get charged. And we have reliable techniques to measure it. In addition to this, we are aware of how this can modify the main properties of the fluidized bed. And we also know how to limit and control the effects of electrostatic forces. Nonetheless, the number of unanswered questions remains large, and new research seems to open more questions than it answers.

1.4.2 Modeling of electrostatic forces in fluidized beds

Modeling of the contact electrification phenomenon

Before trying to model the charge dynamics in a complex system like a fluidized bed, it is important to understand the electrification dynamics of a single particle. This is mainly done by the surface state theory which deals with the description of the electronic state of surfaces. This theory explains the charge transfer between two surfaces using the concept of work function, which is the energy required to remove an electron from the surface of an object. According the surface state theory, when two surfaces approach each other, the difference in work function creates an exchange of electron between the objects. For insulating

materials, it is assumed that electrons are exchanged at the interface to create an electrostatic field that balance the work function difference (Schein et al., 1992).

Based on this theory, Ali et al. (1998) developed a charge exchange model for two colliding spherical particles. In their proposition, they used a soft-sphere model to calculate the area of contact between the colliding particles. This information coupled with the surface state theory allowed them to calculate the amount of charge transferred during a collision. Later, Laurentie et al. (2013) extended this model by accurately solving the contact area between the particles as a function of time during the collision. Their model showed an excellent agreement with the experimental results. Finally, Kolehmainen et al. (2017) adapted this model to calculate the electric charge in a system with multiple particles, like a fluidized bed.

Modeling of fluidized beds with charged particles

Although the effects of the electrostatic forces in fluidized beds have been well studied experimentally. The mathematical modeling and simulation of this phenomenon in particle laden flows is still in its early stages. Different factors are responsible for this lag between the experimental and modeling research. First, even though the presence of electrostatic phenomenon is well known for many decades, the actual understanding of how the particles get charged at a microscopic level is not yet fully understood. Second, a fluidized bed reactor, even without electrostatic forces, involves phenomena of different length scales and physical nature, like particle-fluid, particle-wall and particle-particle interactions. It is not until very recently that we started having the necessary tools to correctly model the behavior of a neutral fluidized bed.

As we stated in section 1.3, the modeling and simulation of fluidized bed is done using either direct numerical simulation, discrete element method, or the two-fluid model. Although DNS is the most accurate approach available, to the best of our knowledge, there has been no published research involving the use of this technique to study the electrostatic effects in gas-solid flows. This might be due to two factors: firstly, the additional particle-particle force adds an extra layer of complexity to an already costly numerical simulation. Secondly, DNS might also require a detailed understanding of the electric charge distribution at the surface of the particle, which is still poorly understood to this day.

The DEM is much simpler to implement because the electric charge distribution around the particle can be neglected. However the electrostatic interaction between the particles still represents an important computing challenge. An exact computation of the electrostatic force between all the particles is proportional to the number of particles squared (this is called the n-body problem). It is for this reasons that part of the research work in this area has dealt with more efficient algorithms to solve this problem. Hassani et al. (2013) computed

the electrostatic interaction of each particles using only nearby particles. They were able to simulate a fluidized bed with particles with constant electric charge. They showed that as the electric charge of particles increases, the bubble diameter decreases (in agreement with Dong et al. (2015)). Their data also highlighted that adding identical particles but with the opposite polarity makes the bed behave like more like a neutral system. In particular, they observed that particles of different charge sign have the tendency to form clusters and this reduces the overall electrostatic effects. Pei et al. (2013) proposed a contact electrification model for the particle-particle and particle wall contacts. In their 2D fluidized bed, they showed that the charge generation happens due to the particle-wall contacts and then the electric charge propagates into the domain due to the particle mixing or the particle-particle collisions. Later, they extended this study to particles with different work functions (Pei et al., 2016). According to their model, having particles with different work function can lead to a bipolar charging phenomenon inside the fluidized bed. Given that this bipolar charging effect was already known from experiments. Yang et al. (2017) simulated a fluidized with large and fines particles with different polarity. Their results showed that the fines particles adhere to the big particles due to the electrostatic attraction and this greatly diminish the total entrainment rate of fines particles.

Finally, the two-fluid model approach can be easily extended to incorporate the electrostatic force. A very important advantage is that adding this extra interaction is not too computationally expensive, because the solid phase is not longer considered as a set of individual particles, but rather a continuum phase. The first use of the two fluid model to simulate a fluidized bed under electrostatic effects came by Shih et al. (1987). They simulated a fluidized bed with charged particles under the effect of an external electric fluid. They, however, neglected the local electric field generated by the particles themselves and the charge transfer between particle-particle or particle-wall contacts. Their results showed that an external electric field can indeed be used to modify and control the shape, size and velocity of rising bubbles. We would have to wait 15 years for the next modeling work, this time published by Al-Adel et al. (2002). They derived a steady state model from the momentum balance equations combined with the Maxwell's equation for the electric field. Solving this set of equations allowed them to predict the segregation of charged particles toward the wall in a riser. Later, Rokkam et al. (2010, 2013) extended Shih's study. They proposed a model to consider the electric field generated by the particles using Maxwell's equations. Their simulations showed that this approach was capable of predicting the wall sheeting effect in a fluidized bed reactor. During the same period, Jalalinejad et al. (2012) also used this same approach to study the deformation of a single rising bubble in a fluidized bed. According to their results, the bubble suffers an axial elongation. The reason behind this effects lies in the fact that the electric field pushes the charged particles towards the wall leaving less space for the bubble to grow radially.

The main drawback of all these previous studies was that the electric charge of particles is constant and it needs to be specified by the user. This data usually came from experimental results. Recently some efforts have been made to address this limitation. Kolehmainen et al.

(2018) use the kinetic theory of granular flow to derive a transport equation of the average electric charge of particles for mono-disperse configurations. Later, Ray et al. (2019) extended this model to take into account the mean electric charge flux term due to the random motion of particles, and in a later study they expanded to bi-disperse configurations (Ray et al., 2020). All of these works however consider that the particle velocity is not correlated with the particle electric charge.

This shows that the modeling of fludiized bed with charged particles it is a still a very open research topic. Although in the recent years some works have contributed with full 3D transient models that could predict the tribocharging phenomenon in fluidized beds, but further validity is still necessary. Moreover, the hypotheses used to derive the closure laws might be too restrictive and a more complex approach might be necessary.

1.5 Thesis outline

As we have exposed, the electrostatic effects in fluidized beds is a topic that has been studied for several decades. However, many questions remain unanswered. On the experimental front, most of the research on the hydrodynamic behavior has been conducted using intrusive probes techniques. Although they have proven to be very valuable, the information we can extract from them is also very limited. In addition to this, the tribocharging phenomenon is highly dependent on solid-solid contacts. Hence, the presence of a foreign material can modify the particle charging dynamics. It is for this reason, we wish to explore the use of a non-intrusive tomographic technique to study the effects of electrostatic interactions in a fluidized bed reactor. More in particular, we have chosen the Electrical Capacitance Volume Tomography (ECVT) which is a relative novel technology that promises to give a 3D representation of the solid volume fraction inside the bed. This represents an improvement over the old known Electrical Capacitance Tomography (ECT) which can only provide the solid volume fraction in a 2D slice. ECVT devices were conceived only 15 years ago, and their application to fluidized bed is still an open problem. So in this work, we want to explore the use of this technology in fluidized bed, laying the grounds for future work on electrostatic effects in our group.

On the modeling front, we wish to extend the current models used in the Eulerian approach. More in particular, we want to expand the current modeling for the mean electric charge transport equation. Previous works have proposed a simple approach where the correlation between the particle electric charge and velocity is neglected. In this thesis, we will show a strategy to take into account this correlation. In addition to this, we will also propose closure models not only for the second order moments: charge velocity covariance and charge variance, but also for some of the third order moments. To the best of our knowledge this will represent the most complete Eulerian description for monodisperse gas-solid flow with

electrostatic effects.

With these objectives in mind, the present thesis is structured as follow:

Chapter 2 addresses the Eulerian modeling of the particle mean electric charge transport equation. We show that a more general governing equation can be derived without imposing the full form for the particle density probability function. A simple linear modeling of the conditional mean of the particle electric charge proves to be enough to fully close the collision term. We also show that this linear model is also sufficient to derive the transport equation for the charge-velocity covariance. This transport equation is then simplified until obtaining an algebraic closure model.

Chapter 3 is dedicated to the extension of the previous chapter's model. Here, we propose a more complete mathematical model using the full transport equations not only for the particle charge-velocity covariance but also for the particle charge variance. We also propose closure laws for two of the third order statistical moments appearing in the second order moment transport equations. Given that this model greatly increases the number of partial differential equations to be solved, we study possible simplifications to this approach. An algebraic model coupling the particle charge-velocity covariance and the particle variance is proposed. And a semi-algebraic model, where the charge-velocity covariance is kept in its algebraic form, but the variance term is solved using its transport equation.

Chapter 4 tackles our study in the use of ECVT system in fluidized beds. More in particular, we assess the accuracy and performance of a state-of-the-art ECVT device. We primarily focus on the image reconstruction algorithm. We study the default strategy proposed by the system as well as two other algorithms found in the literature. However, the approaches studied were either too inaccurate or too computationally expensive. Given these limitation, we study the use of a feed forward artificial neural network as a image reconstruction technique. To train this network, we present two different strategies. The first one is based on CFD-generated data coupled with a supervised learning approach. The second strategy is based directly on experimental data coupled with a reinforcement learning approach. Both techniques are then tested against simulated and real experimental data.

Chapter 1. Bibliography

M. R. Abbasi, A. Shamiri, and M. A. Hussain. A review on modeling and control of olefin polymerization in fluidized-bed reactors. *Reviews in Chemical Engineering*, 35(3):311–333, 2019.

J. Adanez, A. Abad, F. Garcia-Labiano, P. Gayan, and L. F. De Diego. Progress in chemical-looping combustion and reforming technologies. *Progress in Energy and Combustion Science*, 38(2):215–282, 2012.

M. F. Al-Adel, D. A. Saville, and S. Sundaresan. The effect of static electrification on gas-solid flows in vertical risers. *Industrial and Engineering Chemistry Research*, 41(25):6224–6234, 2002.

F. S. Ali, M. A. Ali, P. Castle, and I. I. Inculet. Charge exchange model of a disperse system of spherical powder particles. In *Conference Record of 1998 IEEE Industry Applications Conference. Thirty-Third IAS Annual Meeting*, pages 1884–1891. IEEE, 1998.

N. Ali, T. Al-Juwaya, and M. Al-Dahhan. An advanced evaluation of spouted beds scale-up for coating TRISO nuclear fuel particles using Radioactive Particle Tracking (RPT). *Experimental Thermal and Fluid Science*, 80:90–104, 2017.

A. H. Alissa Park and L. S. Fan. Electrostatic charging phenomenon in gas-liquid-solid flow systems. *Chemical Engineering Science*, 62(1-2):371–386, 2007.

J. A. Almendros-Ibáñez, M. Fernández-Torrijos, M. Díaz-Heras, J. F. Belmonte, and C. Sobrino. A review of solar thermal energy storage in beds of particles: Packed and fluidized beds. *Solar Energy*, 192(January):193–237, 2019.

A. Anantharaman, R. A. Cocco, and J. W. Chew. Evaluation of correlations for minimum fluidization velocity (Umf) in gas-solid fluidization. *Powder Technology*, 323:454–485, 2018.

R. Ansart, F. Vanni, B. Caussat, C. Ablitzer, and M. Brothier. Effects of reducing the reactor diameter on the dense gas–solid fluidization of very heavy particles: 3D numerical simulations. *Chemical Engineering Research and Design*, 117:575–583, 2017.

J. Baeyens and D. Geldart. An investigation into slugging fluidized beds. *Chemical Engineering Science*, 29(1):255–265, 1974.

M. Bafrnec, J. Bena, and J. Beňa. Quantitative data on the lowering of electrostatic charge in a fluidized bed. *Chemical Engineering Science*, 27(5):1181–1183, 1972.

T. Baron, C. L. Briens, M. A. Bergougnou, J.D.Hazlett, and J. D. Hazlett. Electrostatic effects on entrainment from a fluidized bed. *Powder Technology*, 57(1):55–67, 1987.

R. Beetstra, M. A. van der Hoef, and J. A. M. Kuipers. Drag Force of Intermediate Reynolds Number Flow Past Mono- and Bidisperse Arrays of Spheres R. *AIChE Journal*, 53(2): 489–501, 2007.

H. T. Bi and J. R. Grace. Flow regime diagrams for gas-solid fluidization and upward transport. *International Journal of Multiphase Flow*, 21(6):1229–1236, 1995.

H. T. Bi, N. Ellis, I. A. Abba, and J. R. Grace. A state-of-the-art review of gas-solid turbulent fluidization. *Chemical Engineering Science*, 55:4789–4825, 2002.

X. T. Bi, A. Chen, and J. R. Grace. Monitoring Electrostatic Charges in Fluidized Beds Monitoring Electrostatic Charges in Fluidized Beds. In *The 12th International Conference on Fluidization - New Horizons in Fluidization Engineering*, pages 1001–1008. Curran Associates Inc, 2007.

A. Boëlle, G. Balzer, and O. Simonin. Second-order prediction of the particle-phase stress tensor of inelastic spheres in simple shear dense suspensions. In *ASME-Publications*, pages 9–18. ASME, 1995.

C. L. Briens, M. A. Bergougnou, I. I. Inculet, T. Baron, and J. D. Hazlett. Size distribution of particles entrained from fluidized beds: Electrostatic effects. *Powder Technology*, 70(1): 57–62, 1992.

A. Busciglio, G. Vella, G. Micale, and L. Rizzuti. Analysis of the bubbling behaviour of 2D gas solid fluidized beds. Part I. Digital image analysis technique. *Chemical Engineering Journal*, 140(1-3):398–413, 2008.

L. Calin, L. Caliap, V. Neamtu, R. Morar, A. Iuga, A. Samuila, and L. Dascalescu. Tribocharging of granular plastic mixtures in view of electrostatic separation. *IEEE Transactions on Industry Applications*, 44(4):1045–1051, 2008.

C. Capes and A. McIlhinney. The Pseudoparticulate Expansion of Screen-Packed Gas-Fluidized Beds. *AIChE Journal*, 14(6):917–922, 1968.

A. N. Chandran, S. S. Rao, and Y. B. Varma. Fluidized bed drying of solids. *AIChE Journal*, 36(1):29–38, 1990.

A. H. Chen, H. T. Bi, and J. R. Grace. Measurement of particle charge-to-mass ratios in a gas-solids fluidized bed by a collision probe. *Powder Technology*, 135-136:181–191, 2003.

K. S. Choi, K. T. Moon, J. H. Chung, X. Bi, and J. R. Grace. Electrostatic hazards of polypropylene powders in the fluidized bed reactor. In *IEEE International Conference on Industrial Engineering and Engineering Management*, pages 995–999. IEEE, 2011.

J. Ciborowski and A. Wlodarski. On electrostatic effects in fluidized beds. *Chemical Engineering Science*, 17(1):23–32, 1962.

G. M. Colver. Bubble control in gas-fluidized beds with applied electric fields. *Powder Technology*, 17(1):9–18, 1977.

F. Depypere, J. G. Pieters, and K. Dewettinck. PEPT visualisation of particle motion in a tapered fluidised bed coater. *Journal of Food Engineering*, 93(3):324–336, 2009.

A. Di Renzo and F. P. Di Maio. Homogeneous and bubbling fluidization regimes in DEM-CFD simulations: Hydrodynamic stability of gas and liquid fluidized beds. *Chemical Engineering Science*, 62(1-2):116–130, 2007.

W. Dijkhuizen, G. A. Bokkers, N. G. Deen, M. v. S. Annaland, and J. A. M. Kuipers. Extension of PIV for Measuring Granular Temperature Field in Dense Fluidized Beds. *AIChE Journal*, 53(1):108–118, 2007.

K. Dong, Q. Zhang, Z. Huang, Z. Liao, J. Wang, and Y. Yang. Experimental investigation of electrostatic effect on bubble behaviors in gas-solid fluidized bed. *AIChE Journal*, 61 (4):1160–1171, 2015.

A. Efhaima and M. H. Al-Dahhan. Local time-averaged gas holdup in fluidized bed reactor using gamma ray computed tomography technique (CT). *International Journal of Industrial Chemistry*, 6(3):143–152, 2015.

S. Ergun and A. A. Orning. Fluid Flow through Randomly Packed Columns and Fluidized Beds. *Industrial and Engineering Chemistry*, 41(6):1179–1184, 1949.

M. Ernst, M. Sommerfeld, and S. Laín. Quantification of preferential concentration of colliding particles in a homogeneous isotropic turbulent flow. *International Journal of Multiphase Flow*, 117:163–181, 2019.

L. T. Fan, T.-C. Ho, S. Hiraoka, and W. P. Walawender. Pressure Fluctuations in a Fluidized Bed. *AIChE Journal*, 27(3):388–396, 1981.

L. Fasso, B. T. Chao, and S. L. Soo. Measurement of Electrostatic Charges and Concentration of Particles in the Bed. *Powder Technology*, 33:211–221, 1982.

K. M. Forward. *Triboelectrification of Granular Materials*. PhD thesis, Case Western Reserve University, 2009.

F. Fotovat, R. Ansart, M. Hemati, O. Simonin, and J. Chaouki. Sand-assisted fluidization of large cylindrical and spherical biomass particles: Experiments and simulation. *Chemical Engineering Science*, 126:543–559, 2015.

F. Fotovat, X. T. Bi, and J. R. Grace. Electrostatics in gas-solid fluidized beds: A review. *Chemical Engineering Science*, 173:303–334, 2017.

A. Gajewski. Investigation of the electrification of polypropylene particles during the fluidization process. *Journal of Electrostatics*, 16(2-3):219, 1985.

V. Ganzha. The electrification mechanism in a fluidized bed. *Journal of Engineering Physics*, 13(3):243–249, 1967.

D. Geldart. Types of Gas Fluidization. *Powder Technology*, 7:285–292, 1973.

J. R. Grace, X. Bi, and N. Ellis. *Essentials of Fluidization Technology*. Wiley, 2020.

B. Hage and J. Werther. The guarded capacitance probe - A tool for the measurement of solids flow patterns in laboratory and industrial fluidized bed combustors. *Powder Technology*, 93(3):235–245, 1997.

M. A. Hassani, R. Zarghami, H. R. Norouzi, and N. Mostoufi. Numerical investigation of effect of electrostatic forces on the hydrodynamics of gas-solid fluidized beds. *Powder Technology*, 246:16–25, 2013.

C. He, X. T. Bi, and J. R. Grace. Simultaneous measurements of particle charge density and bubble properties in gas-solid fluidized beds by dual-tip electrostatic probes. *Chemical Engineering Science*, 123:11–21, 2015.

G. Hendrickson. Electrostatics and gas phase fluidized bed polymerization reactor wall sheeting. *Chemical Engineering Science*, 61(4):1041–1064, 2006.

I. I. Inculet, M. A. Bergougnou, and J. D. Brown. Electrostatic Separation of Particles Below 40 μm in a Dilute Phase Continuous Loop. *IEEE Transactions on Industry Applications*, IA-13(4):370–373, 1977.

F. Jalalinejad, X. T. Bi, and J. R. Grace. Effect of electrostatic charges on single bubble in gas-solid fluidized beds. *International Journal of Multiphase Flow*, 44:15–28, 2012.

G. Jiménez-García, R. Aguilar-López, and R. Maya-Yescas. The fluidized-bed catalytic cracking unit building its future environment. *Fuel*, 90(12):3531–3541, 2011.

H. Johnsson and F. Johnsson. Measurements of local solids volume-fraction in fluidized bed boilers. *Powder Technology*, 115(1):13–26, 2001.

M. Kashyap, B. Chalermsinsuwan, and D. Gidaspow. Measuring turbulence in a circulating fluidized bed using PIV techniques. *Particuology*, 9(6):572–588, 2011.

K. Kiared, F. Larachi, M. Cassanello, and J. Chaouki. Flow Structure of the Solids in a Three-Dimensional Liquid Fluidized Bed. *Industrial and Engineering Chemistry Research*, 36(11):4695–4704, 1997.

C. W. Kiewiet, M. A. Bergougnou, J. D. Brown, and I. I. Inculet. Electrostatic Separation of Fine Particles in Vibrated Fluidized Beds. *IEEE Transactions on Industry Applications*, IA-14(6):526–530, 1978.

F. Kleijn van Willigen, J. R. van Ommen, J. van Turnhout, and C. M. van den Bleek. Bubble size reduction in electric-field-enhanced fluidized beds. *Journal of Electrostatics*, 63(6-10): 943–948, 2005.

J. Kolehmainen, A. Ozel, C. M. Boyce, and S. Sundaresan. Triboelectric charging of monodisperse particles in fluidized beds. *AIChE Journal*, 63(6):1872–1891, 2017.

J. Kolehmainen, A. Ozel, and S. Sundaresan. Eulerian modelling of gas-solid flows with triboelectric charging. *Journal of Fluid Mechanics*, 848(June):340–369, 2018.

J. Koornneef, M. Junginger, and A. Faaij. Development of fluidized bed combustion-An overview of trends, performance and cost. *Progress in Energy and Combustion Science*, 33 (1):19–55, 2007.

S. H. Kriebitzsch, M. A. Van Der Hoef, and J. A. M. Kuipers. Fully resolved simulation of a gas-fluidized bed: A critical test of DEM models. *Chemical Engineering Science*, 91:1–4, 2013.

G. Kulah and O. Kaya. Investigation and scale-up of hot-melt coating of pharmaceuticals in fluidized beds. *Powder Technology*, 208(1):175–184, 2011.

D. Kunii and O. Levenspiel. *Fluidization Engineering*. Butterworth-Heinemann, 2003.

S. Langford, C. Wiggins, D. Tenpenny, and A. Ruggles. Positron Emission Particle Tracking (PEPT) for Fluid Flow Measurements. *Nuclear Engineering and Design*, 302:81–89, 2016.

F. Larachi, J. Chaouki, and G. Kennedy. 3-D Mapping of Solids Flow Fields in Multiphase Reactors with RPT. *AIChE Journal*, 41(2):439–443, 1995.

J. C. Laurentie, P. Traoré, and L. Dascalescu. Discrete element modeling of triboelectric charging of insulating materials in vibrated granular beds. *Journal of Electrostatics*, 71(6): 951–957, 2013.

G. S. Lee and S. D. Kim. Pressure fluctuations in turbulent fluidized beds. *Journal of Chemical Engineering of Japan*, 21(5):515–521, 1988.

T. Li, Y. Zhang, and F. Hernández-Jiménez. Investigation of particle-wall interaction in a pseudo-2D fluidized bed using CFD-DEM simulations. *Particuology*, 25:10–22, 2016.

Y. Li, M. Jahanmiri, F. S. Careaga, C. Briens, F. Berruti, and J. McMillan. Applications of electrostatic probes in fluidized beds. *Powder Technology*, 370:64–79, 2020.

J. M. Link, L. A. Cuypers, N. G. Deen, and J. A. Kuipers. Flow regimes in a spout-fluid bed: A combined experimental and simulation study. *Chemical Engineering Science*, 60 (13):3425–3442, 2005.

H. Liu, A. Elkamel, A. Lohi, and M. Biglari. Computational fluid dynamics modeling of biomass gasification in circulating fluidized-bed reactor using the eulerian-eulerian approach. *Industrial and Engineering Chemistry Research*, 52(51):18162–18174, 2013.

M. Liu, Y. Zhang, H. Bi, J. R. Grace, and Y. Zhu. Non-intrusive determination of bubble size in a gas-solid fluidized bed: An evaluation. *Chemical Engineering Science*, 65(11): 3485–3493, 2010.

L. Lu, X. Liu, T. Li, L. Wang, W. Ge, and S. Benyahia. Assessing the capability of continuum and discrete particle methods to simulate gas-solids flow using DNS predictions as a benchmark. *Powder Technology*, 321:301–309, 2017.

N. MacCuaig, J. P. K. Seville, W. B. Gilboy, and R. Clift. Application of gamma-ray tomography to gas fluidized beds. *Applied Optics*, 24(23):4083, 1985.

M. E. Mainland and J. R. Welty. Use of optical probes to characterize bubble behavior in gas-solid fluidized beds. *AIChE Journal*, 41(2):223–228, 1995.

M. Manafi, R. Zarghami, and N. Mostoufi. Effect of electrostatic charge of particles on hydrodynamics of gas-solid fluidized beds. *Advanced Powder Technology*, 30(4):815–828, 2019a.

M. Manafi, R. Zarghami, and N. Mostoufi. Fluidization of electrically charged particles. *Journal of Electrostatics*, 99(February):9–18, 2019b.

P. Mehrani, H. T. Bi, and J. R. Grace. Electrostatic charge generation in gas-solid fluidized beds. *Journal of Electrostatics*, 63(2):165–173, 2005.

B. Milici, M. D. Marchis, G. Sardina, and E. Napoli. Effects of roughness on density-weighted particle statistics in turbulent channel flows. *Journal of Fluid Mechanics*, 739:465–478, 2014.

C. O. Miller and A. K. Logwinuk. Fluidization Studies of Solid Particles. *Industrial and Engineering Chemistry*, 43(5):1220–1226, 1951.

W. O. Moughrabiah, J. R. Grace, and X. T. Bi. Effects of pressure, temperature, and gas velocity on electrostatics in gas-solid fluidized beds. *Industrial and Engineering Chemistry Research*, 48(1):320–325, 2009.

S. Movahedirad, A. M. Dehkordi, E. A. Molaei, M. Haghi, M. Banaei, and J. A. M. Kuipers. Bubble splitting in a pseudo-2D gas-solid fluidized bed for geldart B-type particles. *Chemical Engineering and Technology*, 37(12):2096–2102, 2014.

R. Mudde. Bubbles in a Fluidized Bed: A Fast X-Ray Scanner. *AIChE Journal*, 57(10): 2684–2690, 2010a.

R. F. Mudde. Time-resolved X-ray tomography of a fluidized bed. *Powder Technology*, 199 (1):55–59, 2010b.

Y. Nasro Allah. *Experimental and numerical investigation of electrostatic charges in gas-solid fluidized beds*. PhD thesis, Toulouse-INP, 2019.

A. Ozel, J. C. Brändle de Motta, M. Abbas, P. Fede, O. Masbernat, S. Vincent, J. L. Estivalezes, and O. Simonin. Particle resolved direct numerical simulation of a liquid–solid fluidized bed: Comparison with experimental data. *International Journal of Multiphase Flow*, 89:228–240, 2017.

D. J. Parker. Positron emission particle tracking and its application to granular media. *Review of Scientific Instruments*, 88(5):051803–1–8, 2017.

D. J. Parker, C. J. Broadbent, P. Fowles, M. R. Hawkesworth, and P. McNeil. Positron emission particle tracking - a technique for studying flow within engineering equipment. *Nuclear Inst. and Methods in Physics Research, A*, 326(3):592–607, 1993.

C. Pei, C. Y. Wu, D. England, S. Byard, H. Berchtold, and M. Adams. Numerical analysis of contact electrification using DEM-CFD. *Powder Technology*, 248:34–43, 2013.

C. Pei, C. Y. Wu, and M. Adams. DEM-CFD analysis of contact electrification and electrostatic interactions during fluidization. *Powder Technology*, 304(September):208–217, 2016.

M. Punčochář and J. Drahoš. Origin of pressure fluctuations in fluidized beds. *Chemical Engineering Science*, 60(5):1193–1197, 2005.

M. Punčochář, J. Drahoš, J. Cermak, and K. Selucky. Evaluation of minimum fluidizing velocity in gas fluidized bed from pressure fluctuations. *Chemical Engineering Communications*, 35(1-6):81–87, 1985.

M. Rasouli, F. Bertrand, and J. Chaouki. A multiple radioactive particle tracking technique to investigate particulate flows. *AIChE Journal*, 61(2):384–394, 2015.

M. Ray, F. Chowdhury, A. Sowinski, P. Mehrani, and A. Passalacqua. An Euler-Euler model for mono-dispersed gas-particle flows incorporating electrostatic charging due to particle-wall and particle-particle collisions. *Chemical Engineering Science*, 197:327–344, 2019.

M. Ray, F. Chowdhury, A. Sowinski, P. Mehrani, and A. Passalacqua. Eulerian modeling of charge transport in bi-disperse particulate flows due to triboelectrification. *Physics of Fluids*, 32(2):023302, 2020.

R. G. Rokkam, R. O. Fox, and M. E. Muhle. Computational fluid dynamics and electrostatic modeling of polymerization fluidized-bed reactors. *Powder Technology*, 203(2):109–124, 2010.

R. G. Rokkam, A. Sowinski, R. O. Fox, P. Mehrani, and M. E. Muhle. Computational and experimental study of electrostatics in gas-solid polymerization fluidized beds. *Chemical Engineering Science*, 92:146–156, 2013.

M. Rüdisüli, T. J. Schildhauer, S. M. Biollaz, and J. Ruud van Ommen. Bubble characterization in a fluidized bed by means of optical probes. *International Journal of Multiphase Flow*, 41:56–67, 2012.

M. Sakiz and O. Simonin. Development and validation of continuum particle wall boundary conditions using lagrangian simulation of a vertical gas/solid channel flow. In *3rd ASME/JSME Joint Fluids Engineering Conference*, pages 1–8. ASME, 1999.

F. Salama, A. Sowinski, K. Atieh, and P. Mehrani. Investigation of electrostatic charge distribution within the reactor wall fouling and bulk regions of a gas-solid fluidized bed. *Journal of Electrostatics*, 71(1):21–27, 2013.

L. B. Schein, M. LaHa, and D. Novotny. Theory of insulator charging. *Physics Letters A*, 167(1):79–83, 1992.

S. Schneiderbauer, S. Puttinger, S. Pirker, P. Aguayo, and V. Kanellopoulos. CFD modeling and simulation of industrial scale olefin polymerization fluidized bed reactors. *Chemical Engineering Journal*, 264:99–112, 2015.

Y. T. Shih, D. Gidaspow, and D. Wasan. Hydrodynamics of electroluidization: Separation of pyrites from coal. *AIChE Journal*, 33(8):1322–1333, 1987.

O. Simonin, P. Février, and J. Laviéville. On the spatial distribution of heavy-particle velocities in turbulent flow: from continuous field to particulate chaos. *Journal of Turbulence*, 3(40):1–18, 2002.

D. Song and P. Mehrani. Mechanism of particle build-up on gas-solid fluidization column wall due to electrostatic charge generation. *Powder Technology*, 316:166–170, 2017.

D. Song, F. Salama, J. Matta, and P. Mehrani. Implementation of Faraday cup electrostatic charge measurement technique in high-pressure gas-solid fluidized beds at pilot-scale. *Powder Technology*, 290:21–26, 2016.

A. Sowinski, F. Salama, and P. Mehrani. New technique for electrostatic charge measurement in gas-solid fluidized beds. *Journal of Electrostatics*, 67(4):568–573, 2009.

A. Sowinski, A. Mayne, and P. Mehrani. Effect of fluidizing particle size on electrostatic charge generation and reactor wall fouling in gas-solid fluidized beds. *Chemical Engineering Science*, 71:552–563, 2012.

G. Tardos and R. Pfeffer. A method to measure electrostatic charge on a granule in a fluidized bed. *Chemical Engineering Communications*, 4(6):665–671, 1980.

P. Traoré, J. C. Laurentie, and L. Dascalescu. An efficient 4 way coupling CFD-DEM model for dense gas-solid particulate flows simulations. *Computers and Fluids*, 113:65–76, 2015.

O. Trnka, V. Veselý, M. Hartman, and Z. Beran. Identification of the state of a fluidized bed by pressure fluctuations. *AIChE Journal*, 46(3):509–514, 2000.

M. Van de Velden, J. Baeyens, J. P. K. Seville, and X. Fan. The solids flow in the riser of a Circulating Fluidised Bed (CFB) viewed by Positron Emission Particle Tracking (PEPT). *Powder Technology*, 183(2):290–296, 2008.

J. Van Der Schaaf, J. C. Schouten, F. Johnsson, and C. M. Van Den Bleek. Non-intrusive determination of bubble and slug length scales in fluidized beds by decomposition of the power spectral density of pressure time series. *International Journal of Multiphase Flow*, 28(5):865–880, 2002.

F. Vanni, B. Caussat, C. Ablitzer, and M. Brothier. Effects of reducing the reactor diameter on the fluidization of a very dense powder. *Powder Technology*, 277:268–274, 2015.

K. Vollmari, R. Jasevičius, and H. Kruggel-Emden. Experimental and numerical study of fluidization and pressure drop of spherical and non-spherical particles in a model scale fluidized bed. *Powder Technology*, 291:506–521, 2016.

S. Wang, H. Lu, F. Zhao, and G. Liu. CFD studies of dual circulating fluidized bed reactors for chemical looping combustion processes. *Chemical Engineering Journal*, 236:121–130, 2014.

M. W. Weber and C. M. Hrenya. Computational study of pressure-drop hysteresis in fluidized beds. *Powder Technology*, 177(3):170–184, 2007.

C. Y. Wen and R. F. Hashinger. Elutriation of solid particles from a dense-phase fluidized bed. *AIChE Journal*, 6(2):220–226, 1960.

J. Werther and B. Hage. A fiber-optical sensor for high-temperature application in fluidized bed combustion. In *Fluidization VIII, International Symposium of the Engineering Foundation*, pages 577–584. Engineering Foundation, 1995.

J. Werther, B. Hage, and C. Rudnick. A comparison of laser Doppler and single-fibre reflection probes for the measurement of the velocity of solids in a gas-solid circulating fluidized bed. *Chemical Engineering and Processing: Process Intensification*, 35(5):381–391, 1996.

V. Wiesendorf and J. Werther. Capacitance probes for solids volume concentration and velocity measurements in industrial fluidized bed reactors. *Powder Technology*, 110(1-2): 143–157, 2000.

A. Wolny and W. Kaźmierczak. Triboelectrification in fluidized bed of polystyrene. *Chemical Engineering Science*, 44(11):2607–2610, 1989.

A. Wolny and W. Kaźmierczak. The influence of static electrification on dynamics and rheology of fluidized bed. *Chemical Engineering Science*, 48(20):3529–3534, 1993.

G. Xu, T. Murakami, T. Suda, Y. Matsuzawa, and H. Tani. The superior technical choice for dual fluidized bed gasification. *Industrial and Engineering Chemistry Research*, 45(7): 2281–2286, 2006.

W. C. Yang. Modification and re-interpretation of Geldart's classification of powders. *Powder Technology*, 171(2):69–74, 2007.

Y. Yang, Z. Huang, W. Zhang, J. Wang, M. Lungu, Z. Liao, F. Wang, Y. Yang, Y. Yan, and J. Yang. Effects of agglomerates on electrostatic behaviors in gas-solid fluidized beds. *Powder Technology*, 287:139–151, 2016.

Y. Yang, C. Zi, Z. Huang, J. Wang, M. Lungu, Z. Liao, Y. Y. Yang, and H. Su. CFD-DEM investigation of particle elutriation with electrostatic effects in gas-solid fluidized beds. *Powder Technology*, 308:422–433, 2017.

T. Yehuda and H. Kalman. Geldart classification for wet particles. *Powder Technology*, 362: 288–300, 2020.

J. Yerushalmi and N. T. Cankurt. Further Studies of the Regimes of Fluidization. *Powder Technology*, 24(2):187–205, 1979.

M. Zastawny, G. Mallouppas, F. Zhao, and B. van Wachem. Derivation of drag and lift force and torque coefficients for non-spherical particles in flows. *International Journal of Multiphase Flow*, 39:227–239, 2012.

D. Z. Zhang and A. Prosperetti. Averaged Equations for Inviscid Disperse Two-Phase Flowf. *Journal of Fluid Mechanics*, 267:185–219, 1994.

M. Zhang, H. Wu, Q. Lu, Y. Sun, and G. Song. Heat transfer characteristics of fluidized bed heat exchanger in a 300MW CFB boiler. *Powder Technology*, 222:1–7, 2012.

M. H. Zhang, K. W. Chu, F. Wei, and A. B. Yu. A CFD-DEM study of the cluster behavior in riser and downer reactors. *Powder Technology*, 184(2):151–165, 2008a.

Y. Zhang, C. Lu, and M. Shi. A practical method to estimate the bed height of a fluidized bed of fine particles. *Chemical Engineering and Technology*, 31(12):1735–1742, 2008b.

Y. F. Zhang, Y. Yang, and H. Arastoopour. Electrostatic Effect on the Flow Behavior of a Dilute Gas/Cohesive Particle Flow System. *AIChE Journal*, 42(6):1590–1599, 1996.

H. Zhao, G. S. Castle, I. I. Inculet, and A. G. Bailey. Bipolar charging of poly-disperse polymer powders in fluidized beds. *IEEE Transactions on Industry Applications*, 39(3): 612–618, 2003.

Chapter 2

Eulerian modeling of electrostatic force in mono-dispersed gas-solid flow

As stated in the introductory chapter, we will focus on the Eulerian modeling of fluidized beds. This is hybrid approach where the governing equations for both phases are obtained using different physical theories. On one hand, the fluid phase is governed by the phase-average Navier-Stokes equations. While on the other hand, the solid phase relies on a modification of the kinetic theory of gases to derive the dynamic equations (Zhang and Prosperetti, 1994). This modification is justified given the similarities between the movement of molecules in a gas and the movement of particles in a gas–solid flow. This extended theory is called the Kinetic Theory of Granular Flow (KTGF). In this work, we focus exclusively in the modeling of the charging dynamics of the solid phase. Hence, we will only present the governing equations for the granular phase.

The kinetic theory of granular flow tries to explain the macroscopic properties of a large set of identical particles. These particles can be subjected to body forces (gravity or electromagnetic forces), surface forces (drag, lift, buoyancy, etc.), and contact forces (collision with other particles or with the solid boundaries). The main objective of the KTGF formalism is to obtain the spatial and temporal evolution of the most important macroscopic quantities that can explain the dynamics of the particles. Some of these quantities are: the number of particles per unit of volume, the mean particle velocity and the mean particle fluctuating kinetic energy. However, we can easily extend the theory for other variables such as: the mean particle temperature or even the mean particle weight fraction of its constituents.

The main idea behind this theory is to define a distribution function $f\left(\vec{x}, \vec{c_p}, T_p, \cdots; t\right)$ (where $\vec{c_p}$ and T_p are the particle velocity and temperature, respectively). This particle distribution function can be used to derive a Boltzmann-like equation. From this equation, we can derive the governing conservation laws for some of the statistical moments of f, such as:

1. The particle number density conservation equation:

$$\frac{\partial m_p n_p}{\partial t} + \frac{\partial m_p n_p U_{p,i}}{\partial x_i} = 0 \tag{2.1}$$

2. The mean particle linear momentum conservation equation:

$$n_p \frac{\partial m_p U_{p,i}}{\partial t} + n_p U_{p,j} \frac{\partial m_p U_{p,i}}{\partial x_j} + \frac{\partial n_p m_p R_{p,ij}}{\partial x_j} = n_p \langle F_i \rangle + \mathcal{C} \langle m_p c_{p,i} \rangle \tag{2.2}$$

Here, $U_{p,i}$ is the mean particle velocity, $R_{p,ij}$ is the kinetic stress tensor, $\mathcal{C}\left(m_p c_{p,i}\right)$ is the mean rate of change in the particle linear momentum due to particle-particle collisions (Jenkins and Richman, 1985; Jenkins and Savage, 1983) and $\langle F_i \rangle$ is the mean surface and body force exerted on the particles.

Historically, the only forces considered were the gravity force, the drag force and the buoyancy force:

$$\begin{aligned} n_p \frac{\partial m_p U_{p,i}}{\partial t} + n_p U_{p,j} \frac{\partial m_p U_{p,i}}{\partial x_j} + \frac{\partial n_p m_p R_{p,ij}}{\partial x_j} = \\ - n_p V_p \frac{\partial P_{g@p}}{\partial x_i} - \frac{n_p m_p}{\overline{\tau_p}} \left(U_{p,i} - U_{g,i}\right) + n_p m_p g_i + \mathcal{C} \langle m_p c_{p,i} \rangle \end{aligned} \tag{2.3}$$

Where $P_{g@p}$ is the gas pressure at the particle position, $\overline{\tau_p}$ is the mean particle relaxation time, $U_{g,i}$ is the mean gas velocity and g_i is the gravitational acceleration.

If we wish to add the electrostatic force between the particles, we need to add an additional force term to equation 2.3:

$$\begin{aligned} n_p \frac{\partial m_p U_{p,i}}{\partial t} + n_p U_{p,j} \frac{\partial m_p U_{p,i}}{\partial x_j} + \frac{\partial n_p m_p R_{p,ij}}{\partial x_j} = \\ - n_p V_p \frac{\partial P_{g@p}}{\partial x_i} - \frac{n_p m_p}{\overline{\tau_p}} \left(U_{p,i} - U_{g,i}\right) + n_p m_p g_i + \boxed{n_p Q_p E_i} + \mathcal{C} \langle m_p c_{p,i} \rangle \end{aligned} \tag{2.4}$$

Where Q_p is the mean particle electric charge and E_i is the electric field. This electric field can be a combination of an external electric field and the electric field generated by the particles themselves.

Now, the main problem is how to determine the value of the mean particle electric charge. Previous works have chosen to consider Q_p as a constant value (Rokkam et al., 2010, 2013). Although useful, this approach is very limited, because any effect of the charge spatial distribution would be neglected. In addition to this, the charging phenomenon cannot be studied. And finally, the imposed value of Q_p is not easy to determine. Kolehmainen et al. (2018) and Ray et al. (2019) have taken a different approach, deriving a transport equation for the mean particle electric charge in the Eulerian framework. However, these modeling attempts

assumed no correlation between the particle electric charge and the particle velocity. To improve these formulations, we developed a more general model accounting for the correlation between the electric charge and the particle velocity. This research work was submitted to and accepted by the Journal of Fluid Mechanics (Montilla et al., 2020). What follows is the exact copy of that research paper[1].

[1]Only the original headers were removed and replaced with this document's headers

J. Fluid Mech. (2020), *vol*. 902, A12. © The Author(s), 2020.
Published by Cambridge University Press
doi:10.1017/jfm.2020.577

Modelling of the mean electric charge transport equation in a mono-dispersed gas–particle flow

Carlos Montilla[1], **Renaud Ansart**[1] **and Olivier Simonin**[2,†]

[1]Laboratoire de Génie Chimique, Université de Toulouse, CNRS, INPT, UPS, Toulouse, France

[2]Institut de Mécanique des Fluides de Toulouse (IMFT), Université de Toulouse, CNRS, Toulouse, France

(Received 15 October 2019; revised 21 April 2020; accepted 9 July 2020)

Due to triboelectric charging, the solid phase in gas–particle flows can become electrically charged, inducing an electrical interaction among all the particles in the system. Because this force decays rapidly, many of the current models neglect the contribution of this electrostatic interaction. In this work, an Eulerian particle model for gas–particle flow is proposed in order to take into consideration the electrostatic interaction among the particles. The kinetic theory of granular flows is used to derive the transport equation for the mean particle electric charge. The collision integrals are closed without presuming the form of the electric part for the particle probability density function. A linear model for the mean electric charge conditioned by the instantaneous particle velocity is proposed to account for the charge–velocity correlation. First, a transport equation is written for the charge–velocity correlation. Then, a gradient dispersion model is derived from this equation by using some simplifying hypotheses. The model is tested in a three-dimensional periodic box. The results show that the dispersion phenomenon has two contributions: a kinetic contribution due to the electric charge transport by the random motion of particles and a collisional contribution due to the electric charge transfer during particle–particle collisions. Another phenomenon that contributes to the mean electric charge transport is a triboelectrical current density due to the tribocharging effect by particle–particle collisions in the presence of a global electric field. The corresponding electric charge flux is written as equal to the product of the electric field by a triboconductivity coefficient.

Key words: kinetic theory, mixing and dispersion, fluidized beds

1. Introduction

Nowadays, gas–particle-laden flows play an extremely important role in many industrial technologies. Fluidized beds, cyclonic separators and the transport of air pollutants are just a few examples of this type of flow. In some configurations, the particles collide with other solid materials (either another particle or a solid boundary). During these interactions, the particles can get electrically charged due to the triboelectrification effect (Matsusaka & Masuda 2003). The electrically charged particles can now interact with other charged particles via the Lorentz force (electrostatic + magnetic forces). Because the

† Email address for correspondence: olivier.simonin@toulouse-inp.fr

particle velocity is very small compared to the speed of light, the magnetic contribution can be dropped, and only the Coulomb force is relevant.

The generation of electrical charges can be undesirable for many industrial processes. There are safety hazards such as the risk of explosions due to a spark, wall sheeting and the generation of an intense electric field. It is also known that the electrostatic force can have different effects on the dynamics of gas–particle flows, such as: modification of the minimum fluidization velocity, the entrainment rate and the heat transfer coefficient (Miller & Logwinuk 1951; Hendrickson 2006).

All these electrostatic effects are well documented in the literature. Sowinski, Salama & Mehrani (2009) and Sowinski, Miller & Mehrani (2010) built a fluidized bed with a Faraday cup to measure the total particle charge after fluidization. Their results showed that the particles get charged and the magnitude of the electric charge depends on the fluidization velocity. Moreover, the entrained fine particles and the remaining bed particles have an inverse polarity. Salama *et al.* (2013) focused their study on the particles inside the bed. They observed that, although globally the bed is charged negatively, there is a small percentage of particles with a positive charge. This suggests the wall sheet is formed by consecutive layers of negatively and positively charged particles. Zhou *et al.* (2013) introduced a moving probe inside a fluidized bed to map the electric potential inside the column. Their data reveal that the bed is negatively charged at the bottom and positively charged at the top. Moreover, they also found a difference in the radial profile; with the wall having a stronger potential than the centre of the bed. The entrainment rate is also impacted by the presence of an electrostatic force. Fotovat *et al.* (2017) showed that the entrainment rate is overestimated by the current correlations found in the literature. The gas dynamics can also be impacted. Dong *et al.* (2015) placed four electrostatic probes inside a fluidized bed to analyse the effect of the electrostatic force on the motion of bubbles. The authors observed that the bubble size decreases as the electrostatic force increases. They attributed this result to the fact that most of the particles have the same charge sign. This creates a repulsive force between them, leaving less space for the bubble to grow.

The modelling of gas–particle flows is a very complex topic due to the different scales involved. The most accurate approach is to fully resolve the dynamic equations in the gas–particle mixture. This would require us to accurately compute the flow field around each particle and to use the stress tensors to compute the force acting on the solid phase (Ozel *et al.* 2017). This approach is computationally expensive and can only be done for a few thousand particles. A less computational demanding approach is the so-called discrete element method (DEM). In this method, we use the simplification of the point particle to model the solid phase. The forces acting on the particles due to the flow field are computed using correlations based on the undisturbed flow field (Kriebitzsch, Van der Hoef & Kuipers 2013). This approach reduces the computational cost by allowing us to compute the fluid phase flow on a coarse mesh compared to the particle size. However, we still need to keep track of every particle in the system. With the current computing power, this method allows us to manipulate systems up to a few tens of millions of particles. This is still, at the present time, insufficient for most industrial problems. Finally, another method is called the Eulerian approach, in which we derived the governing equations for the mean properties of the phases (volume fraction, velocity, fluctuant kinetic energy, etc.). For the fluid phase we use the standard averaged Navier–Stokes equations. While the solid phase equations rely on the kinetic theory of granular flows.

The kinetic theory of granular flow (KTGF) is based on the analogy between the motion of particles in rapid granular flow and the motion of molecules in gases. At early stages, Jenkins & Savage (1983) and Jenkins & Richman (1985) derived closed mean momentum and granular temperature (random kinetic energy) transport equations in the frame of a

hard-sphere collision model by assuming a perturbed Maxwellian (or Gaussian) velocity distribution. Later, the KTGF was extended to gas–solid flow by accounting for the drag force in the macroscopic transport equations (Ding & Gidaspow 1990) and in the closure of the transport properties (Boelle, Balzer & Simonin 1995).

Currently, some efforts have been made in order to add the electrostatic force to Eulerian codes. Rokkam, Fox & Muhle (2010) developed a model in which the electrostatic effect is added as a body force in the solid momentum equation. Later, the same authors (Rokkam *et al.* 2013) tested this model in a fluidized bed reactor using the ANSYS Fluent software. Their model was in good agreement with the experimental observations, especially concerning the radial segregation of the solid phase. In this approach, however, the electrical charge is an input parameter and remains fixed throughout the simulation.

A more complex model was proposed by Kolehmainen, Ozel & Sundaresan (2018); they used the kinetic theory of granular flow to derive a transport equation for the particle charge. Using uncorrelated Maxwellian probability density distributions for the velocity and the particle charge, they were able to close the collision integral and to derive an electric charge collisional dispersion coefficient. However, this coefficient was found to represent only a part of the particle electric charge dispersion, therefore, they decided to add a kinetic dispersion coefficient following an analogy with the heat transfer coefficient (Hsiau & Hunt 1993). The results showed that this new formulation was in better agreement with DEM simulations. More recently, Ray *et al.* (2019) extended this modelling approach by accounting for the charge–velocity correlation in order to derive a kinetic dispersion coefficient. The authors also derived the charge variance equation in order to fully close the mean charge transport equation. They implemented their model using OpenFOAM and simulated a two-dimensional fluidized bed. The results showed that the proposed model was able to successfully predict the thickness of the particle layer formed at the wall of the reactor. It is worth noting that these previous studies were conducted with the assumption that the Coulomb force does not modify the dynamics of the particle–particle collisions. Although this hypothesis holds for rapid granular flows, it might be too restrictive for configurations where the electric potential energy is comparable to the kinetic energy.

In our work, we propose a closure for the collisional and kinetic electric charge dispersion terms in the mean charge transport equation derived in the framework of the kinetic theory of rapid granular flows, keeping the assumption that the electrostatic force does not affect the particle–particle hard-sphere collision model. In particular, we show that the closure assumption for the collisional contribution can be derived without assuming an uncorrelated charge and velocity probability distributions. In addition, we derive closures for the dispersion term and for the triboelectric current density, due to the transport of electric charges by the random motion of particles, from the transport equation of the charge–velocity correlation.

2. Particle dynamics

2.1. *Equation of motion for a single particle*

Assuming instantaneous particle–particle collisions, the motion equation for a single particle between two collisions is described by Newton's second law of motion (Gatignol 1983; Maxey & Riley 1983)

$$m_p \frac{\mathrm{d}u_{p,i}}{\mathrm{d}t} = -V_p \frac{\partial P_{g@p}}{\partial x_i} + F_{d,i} + m_p g_i + q_p E_i. \tag{2.1}$$

The right-hand side of the equation represents the sum of forces acting on the particles. There, we found in order: the generalized Archimedes force, the drag force, gravity and the last term is the electrostatic force due to the electric field generated by the presence of other charged particles.

Here, m_p is the mass of the particle, $u_{p,i}$ the particle velocity, V_p the particle volume, $\partial P_{g@p}/\partial x_i$ is the undisturbed pressure gradient at the particle centre, g_i is the gravity, $F_{d,i}$ is the drag force, E_i is the electric field and q_p is the particle electric charge. Hereinafter, all the equation are presented in tensor notation using the Einstein summation convection over all indices except p.

The drag force can be written as

$$\boldsymbol{F}_d = -m_p \frac{\rho_g}{\rho_p} \frac{3}{4} \frac{C_d}{d_p} |\boldsymbol{v_r}| \boldsymbol{v}_r = -\frac{m_p}{\tau_p} \boldsymbol{v_r}, \tag{2.2}$$

where ρ_g is the gas density, ρ_p is the particle density, d_p is the particle diameter, $\boldsymbol{v_r}$ is the relative velocity between the particle and the undisturbed fluid flow at the centre of the particle $\boldsymbol{v_r} = \boldsymbol{u_p} - \boldsymbol{u_{g@p}}$, C_d is the local drag coefficient and τ_p is the particle relaxation time:

$$\tau_p = \frac{4}{3} \frac{\rho_p}{\rho_g} \frac{d_p}{C_d |\boldsymbol{v_r}|}. \tag{2.3}$$

Following Maxwell's equation, we can find the electric field

$$\boldsymbol{\nabla}(\varepsilon \boldsymbol{\nabla} \varphi) = -\varrho, \tag{2.4}$$

$$E_i = -\boldsymbol{\nabla} \varphi, \tag{2.5}$$

where φ is the electrical potential, ϱ is the charge density and ε is the mixture permittivity.

2.2. *Particle–particle collision dynamics*

Some of the most important aspects of particle dynamics are the particle–particle collisions, and the exchange of momentum and electric charge during the collision. Following the hard-sphere collision model, we limit our study to binary collisions of frictionless inelastic spherical particles.

Let us consider two particles p_1 and p_2 with their centres located at $\boldsymbol{x}_{p1}$ and $\boldsymbol{x}_{p2}$. They have given velocities $\boldsymbol{c}_{p1}$ and $\boldsymbol{c}_{p2}$ and electric charges ξ_{p1} and ξ_{p2}. We define $\boldsymbol{k}$ as the unit vector going from the centre of p_1 to the centre of p_2, we also define $\boldsymbol{g_r}$ as the relative velocity of the particles $g_{r,i} = c_{p1,i} - c_{p2,i}$.

Previous studies (Kolehmainen *et al.* 2018; Ray *et al.* 2019) have chosen to neglect the effect of the Coulomb interaction when two particles are colliding. This assumption is valid for rapid granular flow where the kinetic energy of particles is much greater than their electric energy. This hypothesis also preserves all the models developed for the momentum conservation equation. In concordance with the previous work, we have chosen to keep this hypothesis. Therefore, the particle velocities after the collision, $\boldsymbol{c}^+_{\boldsymbol{p1}}$ and $\boldsymbol{c}^+_{\boldsymbol{p2}}$, are given by

$$c^+_{p1,i} = c_{p1,i} - \tfrac{1}{2}(1 + e_c)(g_{r,j} k_j) k_i, \tag{2.6}$$

$$c^+_{p2,i} = c_{p2,i} + \tfrac{1}{2}(1 + e_c)(g_{r,j} k_j) k_i, \tag{2.7}$$

where e_c is the collision restitution coefficient.

To take into account the triboelectrification phenomenon, we use the model developed by Kolehmainen *et al.* (2017). They used a Hertzian collision model to calculate the overlapping area $\mathcal{A}_{max}$ during a collision between two particles. Using the triboelectrification model proposed by Laurentie *et al.* (2013), they were able to compute the charge transfer during the impact

$$\xi_{p1}^{+} = \xi_{p1} - \varepsilon_0 \mathcal{A}_{max} E_i^* k_i, \tag{2.8}$$

$$\xi_{p2}^{+} = \xi_{p2} + \varepsilon_0 \mathcal{A}_{max} E_i^* k_i, \tag{2.9}$$

where E_i^* is the total electric field, which has the contribution of the resolved electric field plus the contribution of the electric field generated by the colliding particles

$$E_i^* = E_i - \frac{\xi_{p2} - \xi_{p1}}{\pi \varepsilon_0 d_p^2} k_i \tag{2.10}$$

The value of $\mathcal{A}_{max}$ is given by the Hertzian model

$$\mathcal{A}_{max} = \pi \frac{d_p}{2} \left(\frac{30 m_p (1 - \nu^2)}{32 Y \sqrt{d_p}} \right)^{2/5} (g_{r,m} k_m)^{4/5}, \tag{2.11}$$

where Y is the particle Young's modulus, and ν is the particle Poisson's ratio.

Finally, the charge transfer model by collision can be written as

$$\xi_{p1}^{+} = \xi_{p1} + \left[-\beta E_i k_i + \frac{\beta}{\gamma} (\xi_{p2} - \xi_{p1}) \right] (g_{r,m} k_m)^{4/5}, \tag{2.12}$$

$$\xi_{p2}^{+} = \xi_{p2} - \left[-\beta E_i k_i + \frac{\beta}{\gamma} (\xi_{p2} - \xi_{p1}) \right] (g_{r,m} k_m)^{4/5}. \tag{2.13}$$

With

$$\beta = \varepsilon_0 \pi \frac{d_p}{2} \left(\frac{30 m_p (1 - \nu^2)}{32 Y \sqrt{d_p}} \right)^{2/5}, \tag{2.14}$$

$$\gamma = \pi \varepsilon_0 d_p^2. \tag{2.15}$$

According to (2.12) and (2.13), we can point out that the electric charge transfer between colliding particles due to the triboelectric effect may be written as two separate contributions. The first one is directly proportional to the global electric field projection on the vector $\boldsymbol{k}$, while the second one is proportional to the electric charge difference between the two colliding particles. As shown below, these two contributions lead to very different modelled transport terms in the mean electric charge transport equation.

3. Eulerian modelling of the electrostatic phenomenon

In order to derive a continuum model for the solid phase, we use the fact that the motion of particles in a rapid granular flow is very similar to the motion of molecules in a gas. This allows us to use the kinetic theory to obtain the governing equation of the solid phase. Let $f(\boldsymbol{x}, \boldsymbol{c_p}, \xi_p, t) \delta \boldsymbol{x} \delta \boldsymbol{c_p} \delta \xi_p$ be the mean probable number of particles with their centre in

the volume element $[\boldsymbol{x}, \boldsymbol{x} + \delta\boldsymbol{x}]$ at time t, with a velocity in the range $[\boldsymbol{c_p}, \boldsymbol{c_p} + \delta\boldsymbol{c_p}]$ and an electric charge in the range $[\xi_p, \xi_p + \delta\xi_p]$. Using this function, we have the definition for the particle number density (n_p) and the mean value for any property ϕ_p

$$n_p = \int_{\mathbb{R}^3}\int_{\mathbb{R}} f \,\mathrm{d}\xi_p \,\mathrm{d}\boldsymbol{c}_p, \tag{3.1}$$

$$\Phi_p = \langle\phi_p\rangle = \frac{1}{n_p}\int_{\mathbb{R}^3}\int_{\mathbb{R}} \phi_p f \,\mathrm{d}\xi_p \,\mathrm{d}\boldsymbol{c}_p. \tag{3.2}$$

This allows us to define some useful quantities such as the particle mean velocity

$$U_{p,i} = \langle c_{p,i}\rangle = \frac{1}{n_p}\int_{\mathbb{R}^3}\int_{\mathbb{R}} c_{p,i} f \,\mathrm{d}\xi_p \,\mathrm{d}\boldsymbol{c}_p. \tag{3.3}$$

The particle velocity fluctuation

$$c'_{p,i} = c_{p,i} - U_{p,i}. \tag{3.4}$$

The particle kinetic stress tensor

$$R_{p,ij} = \langle c'_{p,i} c'_{p,j}\rangle = \frac{1}{n_p}\int_{\mathbb{R}^3}\int_{\mathbb{R}} c'_{p,i} c'_{p,j} f \,\mathrm{d}\xi_p \,\mathrm{d}\boldsymbol{c}_p. \tag{3.5}$$

Assuming an uncorrelated motion of particles (Fox 2014), the granular temperature can be defined as

$$\Theta_p = \frac{R_{p,ii}}{3}. \tag{3.6}$$

The particle mean electric charge

$$Q_p = \langle\xi_p\rangle = \frac{1}{n_p}\int_{\mathbb{R}^3}\int_{\mathbb{R}} \xi_p f \,\mathrm{d}\xi_p \,\mathrm{d}\boldsymbol{c}_p. \tag{3.7}$$

The particle electric charge fluctuation

$$\xi'_p = \xi_p - Q_p. \tag{3.8}$$

The particle electric charge covariance

$$\mathcal{Q}_p = \langle\xi'_p\xi'_p\rangle = \frac{1}{n_p}\int_{\mathbb{R}^3}\int_{\mathbb{R}} \xi'_p\xi'_p f \,\mathrm{d}\xi_p \,\mathrm{d}\boldsymbol{c}_p. \tag{3.9}$$

3.1. *Boltzmann equation*

The dynamic evolution of f is given by the Boltzmann equation

$$\frac{\partial f}{\partial t} + \frac{\partial}{\partial x_i}[c_{p,i} f] + \frac{\partial}{\partial c_{p,i}}\left[\left\langle \frac{\mathrm{d}u_{p,i}}{\mathrm{d}t}\middle| \boldsymbol{x}, \boldsymbol{c_p}, \xi_p\right\rangle f\right] + \frac{\partial}{\partial \xi_p}\left[\left\langle \frac{\mathrm{d}q_p}{\mathrm{d}t}\middle| \boldsymbol{x}, \boldsymbol{c_p}, \xi_p\right\rangle f\right] = \left(\frac{\partial f}{\partial t}\right)_{coll}. \tag{3.10}$$

The notation $\langle G|\boldsymbol{x}, \boldsymbol{c_p}, \xi_p\rangle$ is a short form for the conditional expectation $\langle G|\boldsymbol{x_p} = \boldsymbol{x}, \boldsymbol{u_p} = \boldsymbol{c_p}, q_p = \xi_p; t\rangle$.

The right-hand side of the Boltzmann equation accounts for the variation due to particle–particle collisions. We consider that the particle charge only changes due to the collisions with other particles, hence

$$\frac{\mathrm{d}q_p}{\mathrm{d}t} = 0. \tag{3.11}$$

3.2. *General mean transport equation*

From the Boltzmann equation, we can derive a general mean transport equation for any particle property ϕ_p (Chapman & Cowling 1970)

$$\begin{aligned}
&\frac{\mathrm{D}n_p\langle\phi_p\rangle}{\mathrm{D}t} + n_p\langle\phi_p\rangle\frac{\partial U_{p,i}}{\partial x_i} + \frac{\partial n_p\langle\phi_p c'_{p,i}\rangle}{\partial x_i} - n_p\left\langle\frac{\mathrm{D}\phi_p}{\mathrm{D}t}\right\rangle \\
&- n_p\left\langle c'_{p,i}\frac{\partial\phi_p}{\partial x_i}\right\rangle - n_p\left\langle\frac{1}{m_p}\langle F_i|\boldsymbol{x}, \boldsymbol{c_p}, \xi_p\rangle\frac{\partial\phi_p}{\partial c'_{p,i}}\right\rangle \\
&+ n_p\frac{\mathrm{D}U_{p,i}}{\mathrm{D}t}\left\langle\frac{\partial\phi_p}{\partial c'_{p,i}}\right\rangle + n_p\left\langle c'_{p,j}\frac{\partial\phi_p}{\partial c'_{p,i}}\right\rangle\frac{\partial U_{p,i}}{\partial x_j} = \mathcal{C}(\phi_p).
\end{aligned} \tag{3.12}$$

The right-hand side of the equation represents the mean rate of change for ϕ_p due to particle–particle collisions. Following the formulation proposed by Jenkins & Savage (1983) this term can be written as the contribution of a source term and a flux term

$$\mathcal{C}(\phi_p) = \chi(\phi_p) - \frac{\partial}{\partial x_i}\theta_i(\phi_p), \tag{3.13}$$

where

$$\chi = \frac{d_p^2}{2}\int_{\boldsymbol{g}\cdot\boldsymbol{k}>0} \Delta\phi_p(g_{r,i}k_i)f^{(2)}\,\mathrm{d}\boldsymbol{k}\,\mathrm{d}\xi_{p1}\,\mathrm{d}\xi_{p2}\,\mathrm{d}\boldsymbol{c}_{p1}\boldsymbol{c}_{p2}, \tag{3.14}$$

$$\theta_i = -\frac{d_p^3}{2}\int_{\boldsymbol{g}\cdot\boldsymbol{k}>0} \delta\phi_p(g_{r,i}k_i)f^{(2)}k_i\,\mathrm{d}\boldsymbol{k}\,\mathrm{d}\xi_{p1}\,\mathrm{d}\xi_{p2}\,\mathrm{d}\boldsymbol{c}_{p1}\boldsymbol{c}_{p2}, \tag{3.15}$$

where $f^{(2)} = f^{(2)}(\boldsymbol{x_{p1}}, \boldsymbol{c}_{p1}, \xi_{p1}, \boldsymbol{x}_{p1} + d_p\boldsymbol{k}, \boldsymbol{c}_{p2}, \xi_{p2}, t)$ is the two particle pair distribution.

Here, $\Delta\phi_p$ accounts for the total variation of the property ϕ_p during the collision

$$\Delta\phi_p = \phi_{p1}^+ - \phi_{p1} + \phi_{p2}^+ - \phi_{p2}. \tag{3.16}$$

Also, $\delta\phi_p$ is the variation of ϕ_p for the particle p_1

$$\delta\phi_p = \phi_{p1}^+ - \phi_{p1}. \tag{3.17}$$

In order to close the collision integrals in the mean charge equation, we need to give an expression for the joint charge–velocity two particle number density function $f^{(2)}$. Assuming uncorrelated colliding particle velocities and charges in the frame of the Enskog

theory of a dense gas (Chapman & Cowling 1970), Kolehmainen *et al.* (2018) and Ray *et al.* (2019) proposed the following model:

$$f^{(2)} = g_0 f(\boldsymbol{x}_{p1}, \boldsymbol{c}_{p1}, \xi_{p1}, t) f(\boldsymbol{x}_{p2}, \boldsymbol{c}_{p2}, \xi_{p2}, t), \tag{3.18}$$

where g_0 is the radial distribution function and $f(\boldsymbol{x}_p, \boldsymbol{c}_p, \xi_p, t)$ is given by uncorrelated charge and velocity Maxwellian distributions

$$f = \frac{1}{(2\pi\mathcal{Q}_p)^{1/2}} \frac{n_p}{(2\pi\Theta_p)^{3/2}} \exp(-\xi_p'^2/\mathcal{Q}_p)\ \exp(-\boldsymbol{c}_p'^2/\Theta_p). \tag{3.19}$$

This form for the particle number density function has the disadvantage of forcing a null correlation between the particle velocity and electric charge ($\langle c'_{p,i}\xi'_p\rangle = 0$). However, with such an assumption, the electric charge transport by the random motion of particles cannot be accounted for. In our study, we show that the particle electric charge probability distribution does not have to be assumed, and we show that the charge–velocity correlation can be accounted for by using the definition of the probability density function

$$\int_{-\infty}^{\infty}\int_{-\infty}^{\infty} \xi_{p1} f^{(2)}\, \mathrm{d}\xi_{p1}\, \mathrm{d}\xi_{p2} = \langle \xi_{p1} | \boldsymbol{x}_{p1}, \boldsymbol{c}_{p1}, \boldsymbol{x}_{p2}, \boldsymbol{c}_{p2}\rangle f^{*(2)}. \tag{3.20}$$

Here, $f^{*(2)} = f^{*(2)}(\boldsymbol{x}_{p1}, \boldsymbol{c}_{p1}, \boldsymbol{x}_{p2}, \boldsymbol{c}_{p2}, t)$ is the two particle velocity distribution, which does not depend on the electric charge of the particles.

Let us assume that the electric charge of the first particle is not conditioned by the presence of the second colliding particle, therefore

$$\langle \xi_{p1} | \boldsymbol{x}_{p1}, \boldsymbol{c}_{p1}, \boldsymbol{x}_{p2}, \boldsymbol{c}_{p2}\rangle = \langle \xi_{p1} | \boldsymbol{x}_{p1}, \boldsymbol{c}_{p1}\rangle. \tag{3.21}$$

To take into consideration the correlation between the property ξ_p and the particle velocity, we chose a linear model for the mean electric charge conditioned by the particle velocity of the form

$$\langle \xi_{p1} | \boldsymbol{x}_{p1}, \boldsymbol{c}_{p1}\rangle = \langle \xi_p\rangle(x_{p1}) + B_j c'_{p,j}, \tag{3.22}$$

where the vector components B_i are chosen so that the mean charge and charge–velocity correlations are correctly represented by (3.22)

$$B_i = R^{-1}_{p,ij}\langle \xi'_p c'_{p,j}\rangle, \tag{3.23}$$

which, in a hydrodynamic isotropic model, simplifies to

$$B_i = \frac{\langle \xi'_p c'_{p,i}\rangle}{\Theta_p}. \tag{3.24}$$

To close $f^{*(2)}$ we can use the standard assumptions of the kinetic theory of granular flow. In particular, we may assume that the colliding particle velocities are not correlated (molecular chaos)

$$f^{*(2)} = g_0 f^*(\boldsymbol{x}_{p1}, \boldsymbol{c}_{p1}, t) f^*(\boldsymbol{x}_{p2}, \boldsymbol{c}_{p2}, t). \tag{3.25}$$

We can notice that, in turbulent flows, this assumption is valid only for very inertial particles which are not affected by the local turbulent eddies (Simonin, Février & Laviéville 2002).

In order to fully close the electric charge collision term, we need to specify a form for the particle velocity distribution. We have chosen to use a Maxwellian distribution for the sake of simplicity (3.26).

$$f^* = \frac{n_p}{(2\pi\Theta_p)^{3/2}} \exp(-\boldsymbol{c}_p'^2/\Theta_p). \tag{3.26}$$

If the Maxwellian distribution happens to be too restrictive, we can easily extend our model by using more complex propositions (Grad 1949; Jenkins & Richman 1985).

With such a modelling approach, the collisions terms can be fully computed. It is worth noting that this joint velocity–charge probability density function is only necessary for the charge transport equation. So all the standard models developed for the particle momentum and granular temperature equations are still fully compatible with our proposition.

4. Mean charge transport equation

If we now use $\phi_p = \xi_p$ in equation (3.12), we find the following expression for the charge transport equation:

$$n_p \frac{\partial Q_p}{\partial t} + n_p U_{p,i} \frac{\partial Q_p}{\partial x_i} + \frac{\partial n_p \langle \xi_p' c_{p,i}' \rangle}{\partial x_i} = \mathcal{C}(\xi_p). \tag{4.1}$$

From this equation, two terms need to be closed: the last term on the left-hand side which accounts for the correlation between the charge and the velocity and the right-hand side term that represents the mean rate of change for the charge due to particle–particle collisions.

Due to the charge conservation law, it can be shown that the source term of the collision integral vanishes

$$\chi(\xi_p) = 0. \tag{4.2}$$

To compute the flux term, we use its definition (3.15) substituting ϕ_p by ξ_p

$$\theta_i = -\frac{d_p^3}{2} \int_{\mathbb{R}^3} \int_{\mathbb{R}^3} \int_{\mathbb{R}} \int_{\mathbb{R}} \int_{\boldsymbol{g}\cdot\boldsymbol{k}>0} (\xi_{p1}^+ - \xi_{p1})(g_{r,m}k_m) f^{(2)} k_i \, \mathrm{d}\boldsymbol{k} \, \mathrm{d}\xi_{p1} \, \mathrm{d}\xi_{p2} \, \mathrm{d}\boldsymbol{c}_{p1} \boldsymbol{c}_{p2}, \tag{4.3}$$

where the electric charge exchange during a collision is given by (2.8)

$$\begin{aligned}\theta_i = &-\frac{d_p^3}{2} \int_{\mathbb{R}^3} \int_{\mathbb{R}^3} \int_{\mathbb{R}} \int_{\mathbb{R}} \int_{\boldsymbol{g}\cdot\boldsymbol{k}>0} -\beta E_j k_j (g_{r,m}k_m)^{9/5} f^{(2)} k_i \, \mathrm{d}\boldsymbol{k} \, \mathrm{d}\xi_{p1} \, \mathrm{d}\xi_{p2} \, \mathrm{d}\boldsymbol{c}_{p1} \boldsymbol{c}_{p2} \\ &- \frac{d_p^3}{2} \int_{\mathbb{R}^3} \int_{\mathbb{R}^3} \int_{\mathbb{R}} \int_{\mathbb{R}} \int_{\boldsymbol{g}\cdot\boldsymbol{k}>0} \frac{\beta}{\gamma} (\xi_{p2} - \xi_{p1})(g_{r,m}k_m)^{9/5} f^{(2)} k_i \, \mathrm{d}\boldsymbol{k} \, \mathrm{d}\xi_{p1} \, \mathrm{d}\xi_{p2} \, \mathrm{d}\boldsymbol{c}_{p1} \boldsymbol{c}_{p2}.\end{aligned} \tag{4.4}$$

From the equation above, we can see that we have to solve the following integral:

$$\int_{-\infty}^{\infty} \int_{-\infty}^{\infty} (\xi_{p2} - \xi_{p1}) f^{(2)} \, \mathrm{d}\xi_{p1} \, \mathrm{d}\xi_{p2}. \tag{4.5}$$

This yields integrals similar to (3.20). These terms will be treated using the methodology explained in the previous section. This will allow us to fully compute the

collisional flux term

$$\theta_i(\xi_p) = d_p^3\beta E_i g_0 n_p^2(\Theta_p)^{9/10}\Upsilon^{(1.1)} - d_p^4\frac{\beta}{\gamma}\frac{\partial Q_p}{\partial x_i}g_0 n_p^2(\Theta_p)^{9/10}\Upsilon^{(1.2)} + g_0 d_p^5\frac{\partial U_t}{\partial x_j}\frac{\beta}{\gamma}\frac{\partial Q_p}{\partial x_l}(\Theta_p)^{2/5}n_p^2\Psi_{tlji}^{(1.3)}\Upsilon^{(1.3)} + d_p^3\frac{\beta}{\gamma}B_i g_0 n_p^2(\Theta_p)^{7/5}\Upsilon^{(1.4)} - d_p^4 g_0\frac{\partial U_t}{\partial x_j}\frac{\beta}{\gamma}B_l n_p^2(\Theta_p)^{9/10}\Psi_{ltji}^{(1.5)}\Upsilon^{(1.5)}, \tag{4.6}$$

where $\Upsilon^{(\cdot)}$ are constants (given in appendix A), and $\Psi_{tlji}^{(\cdot)}$ are known fourth-order constant tensors.

It is also worth noting that this equation is very similar to the one proposed by Kolehmainen *et al.* (2018). However, our model shows an additional contribution of the two last term on the right-hand side. These terms come from the charge–velocity correlation, which is neglected in the Kolehmainen *et al.* (2018) approach (corresponding to $B_i = 0$).

If we insert this last equation into the collision term definition, and we neglect any term proportional to the mean particle velocity gradient, we get

$$\mathcal{C}(\xi_p) = -\frac{\partial}{\partial x_i}(\sigma_p^{coll}E_i) + \frac{\partial}{\partial x_i}\left(n_p D_p^{coll}\frac{\partial Q_p}{\partial x_i}\right) - \frac{\partial}{\partial x_i}(n_p\eta_{coll}\langle\xi_p' c_{p,i}'\rangle), \tag{4.7}$$

$$D_p^{coll} = d_p^4\frac{\beta}{\gamma}g_0 n_p(\Theta_p)^{9/10}\Upsilon^{(1.2)}, \tag{4.8}$$

$$\sigma_p^{coll} = d_p^3\beta g_0 n_p^2(\Theta_p)^{9/10}\Upsilon^{(1.1)}, \tag{4.9}$$

$$\eta_{coll} = \frac{3}{2}d_p^3\frac{\beta}{\gamma}g_0 n_p\Theta_p^{2/5}\Upsilon^{(1.4)}. \tag{4.10}$$

The mean collision term given by (4.7) represents a mean electric charge transport due to the local triboelectric transfer of charge between colliding particles given by (2.12) and (2.13). The first contribution on the right-hand side is due to the tribocharging effect occurring during particle–particle collisions in the presence of a global electric field. This contribution is written as the divergence of a collisional triboelectrical current density obeying a mesoscopic Ohm's law. Indeed, the corresponding electric charge flux is given equal to the product of the global electric field by a collisional triboconductivity coefficient σ_p^{coll} depending on the particle number density squared and on the granular temperature at the power 9/10. The second contribution represents the triboelectric effect due to the difference of the electric charge between the colliding particles and is written as a dispersion term proportional to the mean charge gradient and a collisional dispersion coefficient D_p^{coll}. In addition, we remark that there is an extra term involving the charge–velocity correlation.

In order to have an idea of the behaviour of these coefficients, we can plot them for a common practical configuration. For this purpose, we choose polyethylene particles, the particle properties are described in table 1. In figures 1 and 2, we show the value of the collisional dispersion and triboconductivity coefficients in function of the solid volume fraction ($\alpha_p = n_p m_p/\rho_p$), for different values of the granular temperature. We can notice that both coefficients grow with the solid volume fraction. This is expected because the particle–particle collision frequency increases with the solid volume fraction. Also, both

Property	Value
d_p	1600 µm
ρ_p	850 kg m^{-3}
Y	2 GPa
ν	0.46
ρ_g	22 kg m^{-3}
μ_g	1.54×10^{-5} Pa s

TABLE 1. Polyethylene particle properties.

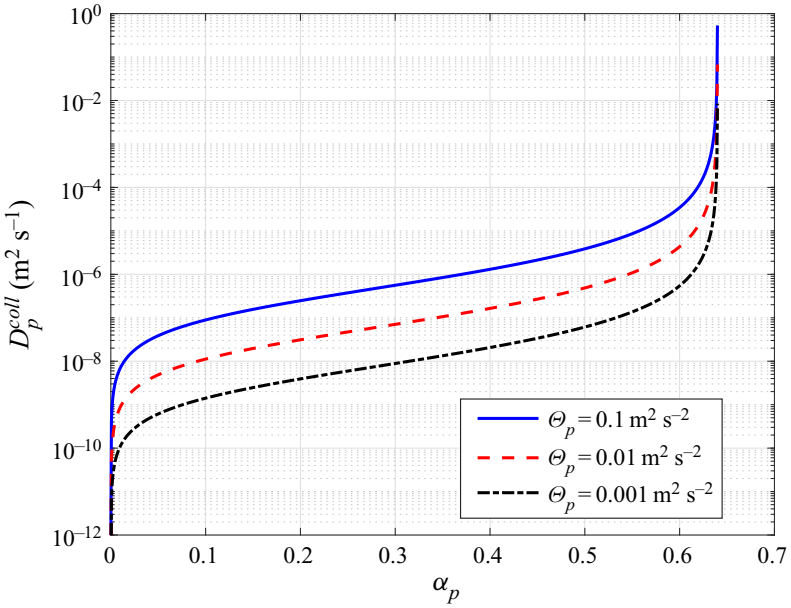

FIGURE 1. Electric charge collisional dispersion coefficient.

coefficients increase with the particle granular temperature. This is also due to the fact that the particle–particle collision frequency increases with the granular temperature.

Finally, the mean charge transport equation may be written as

$$n_p \frac{\partial Q_p}{\partial t} + n_p U_{p,i} \frac{\partial Q_p}{\partial x_i} + \frac{\partial}{\partial x_i}[n_p(1+\eta_{coll})\langle \xi_p' c_{p,i}' \rangle] = -\frac{\partial}{\partial x_i}(\sigma_p^{coll} E_i) + \frac{\partial}{\partial x_i}\left(n_p D_p^{coll} \frac{\partial Q_p}{\partial x_i} \right). \tag{4.11}$$

5. Charge–velocity correlation modelling

5.1. *Charge–velocity correlation equation*

The last term to be closed in the mean charge transport equation (4.11) is the charge velocity correlation $\langle \xi_p' c_p' \rangle$. To accomplish this, we write a transport equation for the correlation between the particle velocity and electric charge derived from the Boltzmann

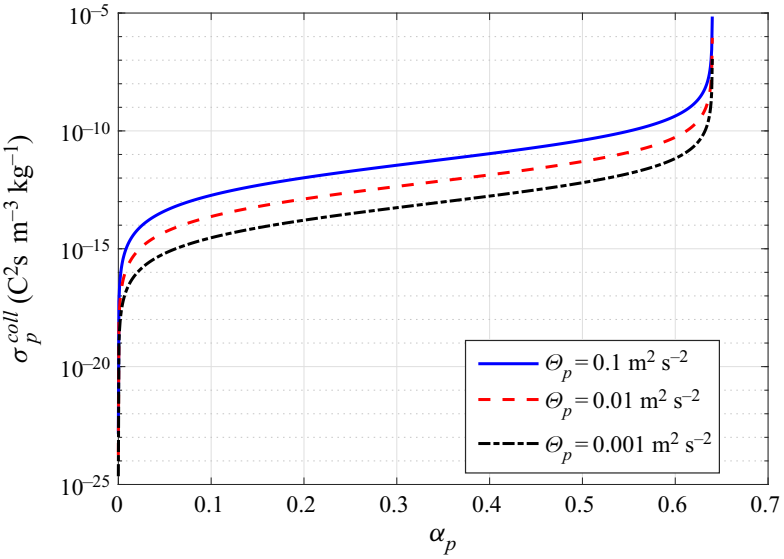

FIGURE 2. Collisional triboconductivity coefficient.

equation (3.10). Therefore, we set $\phi_p = \xi_p c'_{p,i}$ in the general mean transport equation (3.12)

$$n_p \frac{\mathrm{D}\langle \xi_p c'_{p,i}\rangle}{\mathrm{D}t} + \frac{\partial n_p \langle \xi'_p c'_{p,i} c'_{p,j}\rangle}{\partial x_j} + n_p \langle c'_{p,i} c'_{p,j}\rangle \frac{\partial Q_p}{\partial x_j} + n_p \langle c'_{p,j} \xi_p\rangle \frac{\partial U_{pi}}{\partial x_j}$$
$$= n_p \left\langle \frac{1}{m_p} \langle F_i | \boldsymbol{x}, \boldsymbol{c_p}, \xi_p\rangle \xi'_p \right\rangle + \mathcal{C}(\xi_p c'_{p,i}) - Q_p \mathcal{C}(c'_{p,i}). \tag{5.1}$$

If we develop the term $\langle F_i \xi'_p / m_p\rangle$ using particle Newton equation (2.1) we find

$$\left\langle \frac{1}{m_p} \langle F_i | \boldsymbol{x}, \boldsymbol{c_p}, \xi_p\rangle \xi'_p \right\rangle = -\left\langle \frac{V_p}{m_p} \left\langle \frac{\partial P_{g@p}}{\partial x_i} | \boldsymbol{x}, \boldsymbol{c_p}, \xi_p \right\rangle \xi'_p \right\rangle$$
$$- \left\langle \frac{1}{\tau_p} (c_{p,i} - \langle u_{g@p,i} | \boldsymbol{x}, \boldsymbol{c_p}, \xi_p\rangle) \xi'_p \right\rangle$$
$$+ \langle g_i \xi'_p\rangle + \left\langle \frac{1}{m_p} \xi'_p \xi_p E_i \right\rangle. \tag{5.2}$$

We simplify this expression by assuming that the fluid properties of the undisturbed flow at the particle position are not correlated with the particle electric charge. Additionally, we assume that the particle response time is not correlated with the particle velocity

$$\left\langle \frac{1}{m_p} \langle F_i | \boldsymbol{x}, \boldsymbol{c_p}, \xi_p\rangle \xi'_p \right\rangle = -\frac{1}{\overline{\tau_p}} \langle c'_{p,i} \xi'_p\rangle + \frac{1}{m_p} \langle \xi'_p \xi'_p E_i\rangle, \tag{5.3}$$

where

$$\overline{\tau_p} = \left\langle \frac{1}{\tau_p} \right\rangle^{-1}. \tag{5.4}$$

We have also used the following equalities: $\langle c_{p,i} \xi'_p\rangle = \langle c'_{p,i} \xi'_p\rangle$ and $\langle \xi'_p \xi_p\rangle = \langle \xi'_p \xi'_p\rangle$.

Now we can focus on the right-hand side of the charge–velocity correlation (5.1). In order to simplify the collision term, we neglect the mean velocity and granular temperature gradients. With these simplifications, the collision integrals can be computed

$$\begin{aligned}\mathcal{C}(\xi_p c'_{p,i}) - Q_p \mathcal{C}(c'_{p,i}) = &-\Upsilon^{(2.1)} \tfrac{1}{2}(1+e_c) d_p^2 g_0 B_i n_p^2 (\Theta_p)^{3/2} \\ &- \tfrac{1}{2}(3-e_c)\Upsilon^{(2.2)} d_p^2 \frac{\beta}{\gamma} g_0 n_p^2 B_i (\Theta_p)^{19/10} \\ &+ e_c \Upsilon^{(2.3)} d_p^2 \beta E_i g_0 (\Theta_p)^{7/5} n_p^2 \\ &- e_c \Upsilon^{(2.4)} d_p^3 g_0 \frac{\beta}{\gamma} \frac{\partial Q_p}{\partial x_i} (\Theta_p)^{7/5} n_p^2. \end{aligned} \tag{5.5}$$

The first two terms on the right-hand side of the equation are the destruction of the correlation due to the randomization of the particle velocities. The last two terms may lead to either a production or destruction of the charge–velocity correlation due to the charge transfer during the collision.

5.2. *Charge–velocity correlation algebraic model*

In order to close the charge transport equation, we should need to solve the charge–velocity correlation equation. This approach has different difficulties including the computation of three coupled new differential equations with specific wall boundary conditions and closure model assumptions for third-order charge–velocity correlations. A simpler way consists of deriving a model assuming the following hypothesis:

(i) Steady state.
(ii) The third-order moment $\langle \xi'_p c'_{p,i} c'_{p,j} \rangle$ is neglected.
(iii) The charge covariance term $\langle \xi'_p \xi'_p E_i \rangle$ is neglected.
(iv) The velocity gradient on the left-hand side of (5.1) is also neglected.

With these simplifications, we can derive an algebraic model for the charge–velocity correlation written as the sum of two contributions, a mean charge gradient contribution and a flux proportional to the global electric field

$$\begin{aligned}\langle \xi'_p c'_{p,i} \rangle = &- \frac{\Theta_p + \Upsilon^{(\xi)} \tau_\xi^{-1} d_p \Theta_p^{1/2}}{\frac{1}{3}(1+e_c)\tau_c^{-1} + \overline{\tau_p}^{-1} + \frac{2}{5}(3-e_c)\tau_\xi^{-1}} \frac{\partial Q_p}{\partial x_i} \\ &+ \frac{e_c \Upsilon^{(2.3)} d_p^2 \beta g_0 (\Theta_p)^{7/5} n_p}{\frac{1}{3}(1+e_c)\tau_c^{-1} + \overline{\tau_p}^{-1} + \frac{2}{5}(3-e_c)\tau_\xi^{-1}} E_i, \end{aligned} \tag{5.6}$$

where τ_c is the characteristic particle collision time

$$\tau_c = \left(n_p g_0 \pi d_p^2 \sqrt{\frac{16}{\pi} \Theta_p} \right)^{-1}. \tag{5.7}$$

Also, τ_ξ is the characteristic time of electric charge covariance destruction by collisions

$$\tau_\xi = \left(\Upsilon^{(3.2)} d_p^2 \frac{\beta}{\gamma} n_p g_0 \Theta_p^{9/10} \right)^{-1}. \tag{5.8}$$

This time can be found from the charge covariance transport equation (see appendix B).

We can also write the charge–velocity correlation (5.6) in a more compact form

$$n_p\langle\xi_p' c_{p,i}'\rangle = -n_p D_p^{kin}\frac{\partial Q_p}{\partial x_i} + \sigma_p^{kin} E_i. \tag{5.9}$$

Leading to a closed mean electric charge equation

$$n_p\frac{\partial Q_p}{\partial t} + n_p U_{pi}\frac{\partial Q_p}{\partial x_i} = -\frac{\partial}{\partial x_i}[(\sigma_p^{coll} + (1+\eta_{coll})\sigma_p^{\mathrm{kin}})E_i] + \frac{\partial}{\partial x_i}\left[n_p(D_p^{coll} + (1+\eta_{coll})D_p^{kin})\frac{\partial Q_p}{\partial x_i}\right]. \tag{5.10}$$

The above equation shows that accounting for the charge–velocity correlation leads to additional contributions for both the electric charge dispersion coefficient and the triboconductivity coefficient

$$D_p^{kin} = \frac{\Theta_p + \Upsilon^{(\xi)}\tau_\xi^{-1} d_p \Theta_p^{1/2}}{\frac{1}{3}(1+e_c)\tau_c^{-1} + \overline{\tau_p}^{-1} + \frac{2}{5}(3-e_c)\tau_\xi^{-1}} \tag{5.11}$$

$$\sigma_p^{kin} = \frac{e_c \Upsilon^{(2.3)} d_p^2 \beta g_0 (\Theta_p)^{7/5} n_p^2}{\frac{1}{3}(1+e_c)\tau_c^{-1} + \overline{\tau_p}^{-1} + \frac{2}{5}(3-e_c)\tau_\xi^{-1}}. \tag{5.12}$$

The first coefficient (D_p^{kin}) accounts for the dispersion of the electric charge due to transport by the random motion of particles. This dispersion coefficient has already been studied in a more simplified configuration, such as particle self-dispersion in particle-laden flows (Laviéville, Deutsch & Simonin 1995; Abbas, Climent & Simonin 2009). In particular, they found that the particle self-diffusion coefficient in homogeneous isotropic flows can be written as

$$D_p = \tau_p^L \Theta_p, \tag{5.13}$$

where τ_p^L, the particle Lagrangian integral time scale given by the integration of the particle velocity autocorrelation function, is written as

$$\frac{1}{\tau_p^L} = \frac{1+e_c}{3}\frac{1}{\tau_c} + \frac{1}{\overline{\tau_p}}. \tag{5.14}$$

And we can notice that, when the electric charge transfer by collisions is negligible ($\beta/\gamma \to 0$), the charge kinetic dispersion coefficient D_p^{kin} given by (5.11) is fully identical to the self-dispersion coefficient D_p given above (5.13) and (5.14).

Equation (5.11) reveals the three main limiting mechanisms for the particle electric charge kinetic dispersion: the particle–particle collisions, the drag force and the particle charge transfer. When there are many collisions (small values of τ_c) the mean free path of particles is very small, which prevents the particles from travelling long distances, diminishing the particle dispersion. The second mechanism pointed out by Laviéville *et al.* (1995) is the drag force ($\overline{\tau_p}$). Indeed, the effect of the fluid drag force slows down the particle fluctuating motion. This imposes a characteristic distance that a single particle can travel before being stopped due to the drag force. As we increase the effect of the drag force this distance will be smaller, therefore reducing the electric charge dispersion. Finally, the third term limiting the dispersion phenomenon is due to the electric charge

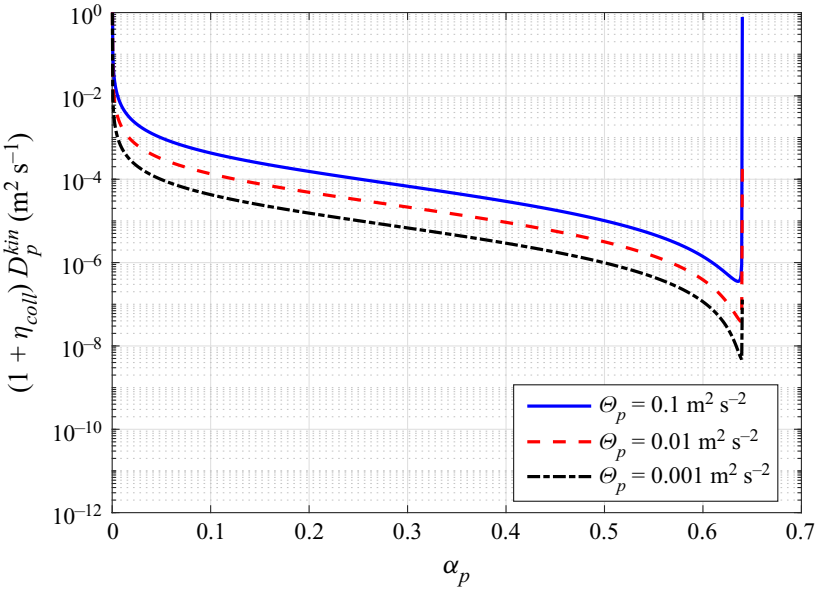

FIGURE 3. Kinetic dispersion coefficient D_p^{kin} weighted by $(1 + \eta_{coll})$ as a function of the solid volume fraction.

transfer during collisions. During its random motion, a single particle will encounter other particles and will transfer some of its electric charge to them. Therefore, the particle will gradually lose the information about its initial electric charge value. Hence, the electric charge dispersion will be impacted negatively. This effect can be characterized by the characteristic time of electric charge covariance destruction by collision (τ_ξ). Indeed, the destruction of the charge covariance and the decorrelation of the charge measured along the particle trajectory are both due to the same mechanism of exchange of charge between particles during collisions. This extra term is a new contribution that has not been remarked in previous works. In conclusion, the dispersion coefficient might be limited by three different factors: particle–particle collisions, the drag force and charge transfer during a collision. The phenomenon with the smallest characteristic time will be the limiting factor.

In the charge transport equation, the contribution of this dispersion coefficient is weighted by the factor $(1 + \eta_{coll})$, this contribution is represented in figure 3. For simplicity we have chosen to neglect the contribution of the drag term, which is effective only for very dilute flows. Because the driving mechanism for this dispersion phenomenon is the transport by the random motion of particles, it is expected that the dispersion coefficient increases with the particle granular temperature. This graph also shows that this term is high in both very dilute and very dense systems. However, as we will show later, for dense configurations, the collisional dispersion coefficient is always larger than the kinetic contribution.

In a previous study conducted by Kolehmainen *et al.* (2018), they suggested that the collisional dispersion coefficient is known to underestimate the dispersion process; and they added a kinetic dispersion coefficient by analogy with particle temperature dispersion in granular flows (Hsiau & Hunt 1993).

The dispersion coefficient used in their work is in fact identical to the self-diffusion coefficient given by (5.13) and (5.14) when the effect of the drag force is negligible ($\overline{\tau_p} \gg \tau_c$). Therefore, our proposed approach, based on the modelling of the particle charge–velocity correlation, leads to a more general expression for the kinetic dispersion

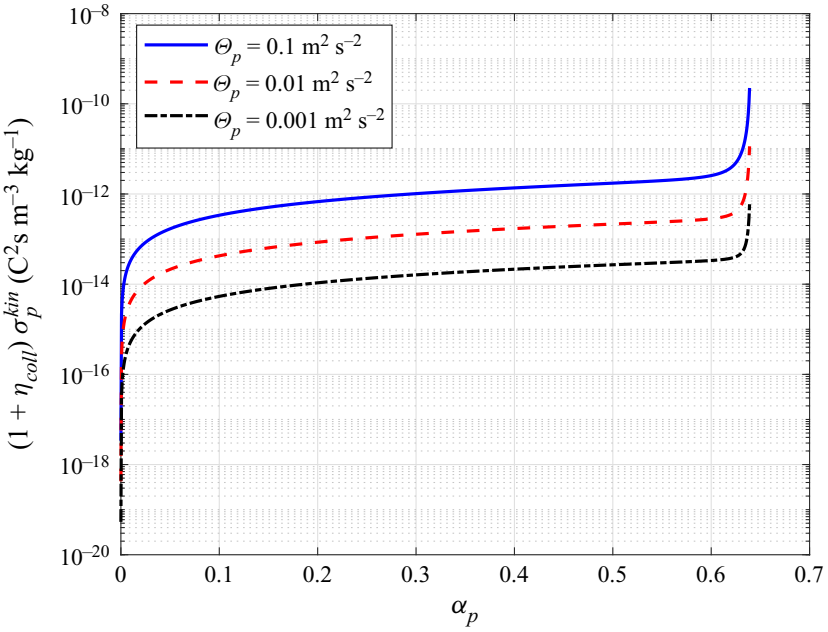

FIGURE 4. Kinetic triboconductivity coefficient weighted by $(1 + \eta_{coll})$ as a function of the solid volume fraction.

coefficients. Indeed, the kinetic dispersion coefficient is found to depend also on the effect of the drag force and of the electric charge transfer during particle–particle collisions.

In the frame of the derivation of the simplified model for the charge–velocity correlation (5.6), in addition to the kinetic dispersion contribution, we obtain a transport term by a kinetic triboelectrical current density obeying a mesoscopic Ohm's law. The corresponding electric charge flux is given as equal to the product of the global electric field and a kinetic triboconductivity coefficient σ_p^{kin}. The kinetic triboconductivity coefficient depends on the particle number density and granular temperature, and also on the different characteristic time scales of the limiting mechanisms of the charge kinetic dispersion: τ_c, $\overline{\tau_p}$ and τ_ξ. As an example, we represented this coefficient as a function of the solid volume fraction for different values of granular temperature in figure 4.

6. Electric charge dispersion

Our modelling approach shows that the dispersion of electric charge can be split into two different contributions: collisional and kinetic. In this part, we compare them both in different configurations. Figure 5 shows the value of the two dispersion coefficients as a function of α_p, for $\Theta_p = 0.01$ m^2 s^{-2}. As we can see, for the dilute system the kinetic contribution is the most important. However, for dense systems, the collisional term is dominant, despite the fact that the kinetic contribution also increases very rapidly. Also, it is worth noting that, for an intermediate value of α_p, the two terms have the same order of magnitude and therefore both have to be considered.

To see the effect of these dispersion coefficients, we study one of the test cases proposed by Kolehmainen *et al.* (2018). They studied a three-dimensional periodic box of $192d_p \times 8d_p \times 8d_p$. Initially, the particles at $x < 96d_p$ are charged positively $Q_p = Q_0$ and the particles at $x \geq 96d_p$ are charged negatively $Q_p = -Q_0$. An initial granular temperature is imposed, and it remains constant during the simulation. We also neglect

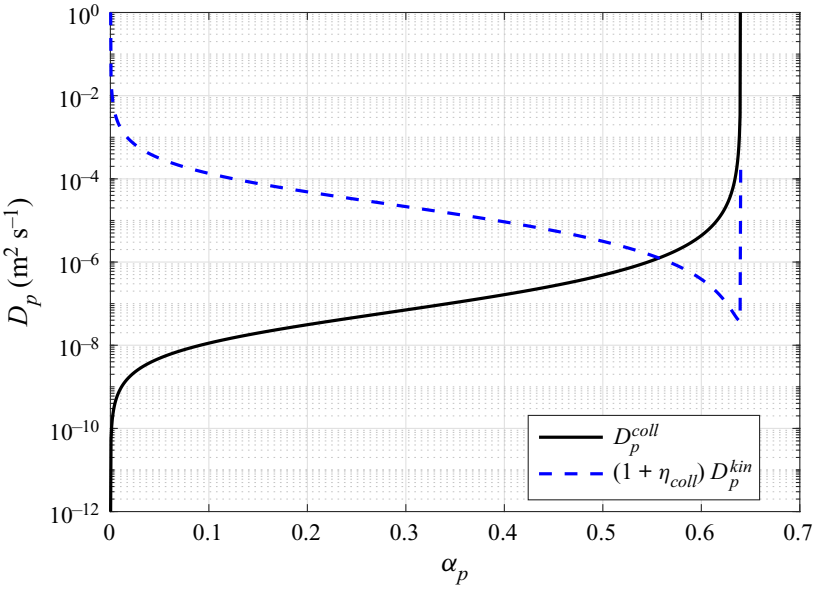

FIGURE 5. Collisional and kinetic dispersion coefficients as a function of the solid volume fraction for $\Theta_p = 0.01$ m^2 s^{-2}.

all the external forces (gravity, drag, electrostatic, etc.). For simplicity, in this part we also neglect the triboconductivity effect; this is analysed in the next section. Using these hypotheses, the charge transport equation can be simplified to a one-dimensional diffusion equation

$$n_p \frac{\partial Q_p}{\partial t} = n_p [D_p^{coll} + (1+\eta_{coll}) D_p^{kin}] \frac{\partial^2 Q_p}{\partial x^2}. \tag{6.1}$$

This equation can be solved analytically

$$Q_p = \sum_{n=1}^{\infty} \lambda_n \exp(-(D_p^{coll} + (1+\eta_{coll}) D_p^{kin})(2\pi n/L)^2 t) \sin\left(\frac{2\pi n x}{L}\right) \tag{6.2}$$

$$\lambda_n = \frac{2Q_0}{n\pi}(1-(-1)^n), \tag{6.3}$$

where $L = 192 d_p$ is the box length in the x direction.

This equation allows us to study the evolution of the electric charge as a function of time. For the simulation, we use the same type of particles as before and we set $\alpha_p = 0.60$. In figure 6 we plot the particle charge spatial profile for different values of the non-dimensional time $t^* = (\sqrt{\Theta}/d_p)t$. As we can see, the electric charge is dispersed inside the domain as the time passes and tends to reach the equilibrium value $Q_p = 0$.

A more interesting analysis can be performed if we separate the kinetic and collisional contributions to the dispersion mechanism. Figures 7, 8 and 9 show the particle charge profile for a dense system ($\alpha_p = 0.60$), a dilute system ($\alpha_p = 0.05$) and an intermediate system ($\alpha_p = 0.55$). The squares markers with a solid line represent the total dispersion, the solid line represents for the collisional contribution and the dashed line is the contribution of the kinetic term. As we can see, for dilute systems, the dispersion comes almost exclusively from the kinetic dispersion coefficient contribution. On the contrary, for dense systems, the collisional term accounts for most of the electric charge dispersion.

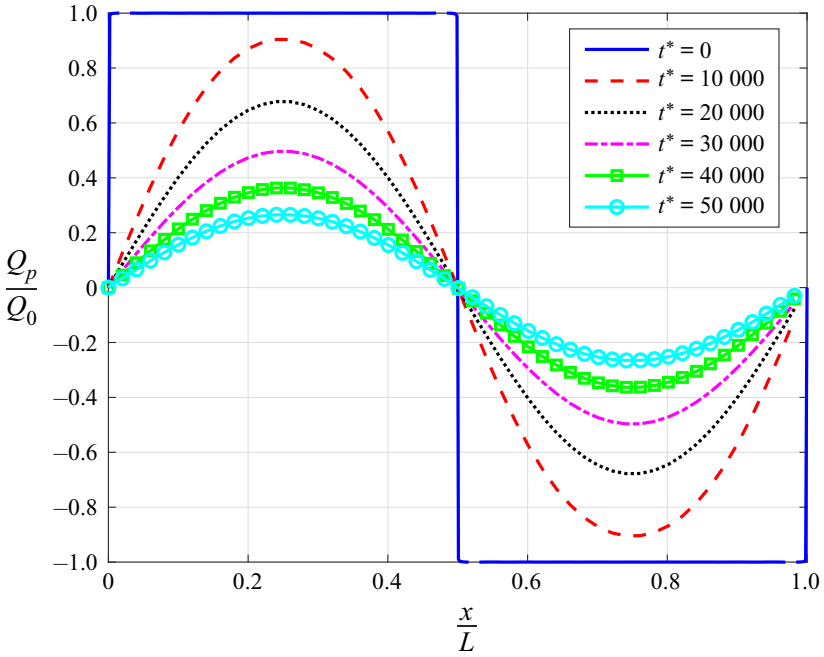

FIGURE 6. Particle charge profile as a function of x/L at different times $t^* = (\sqrt{\Theta}/d_p)t$.

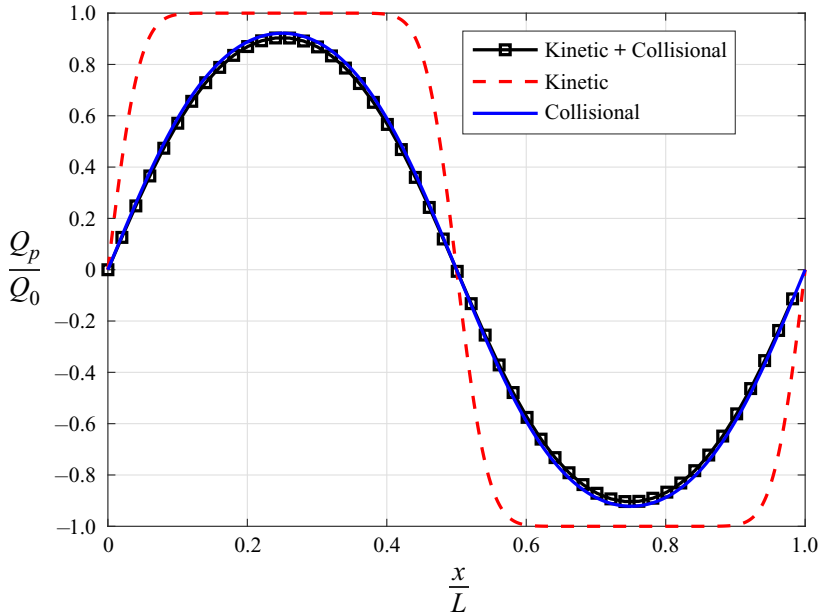

FIGURE 7. Particle charge profile at $t^* = 10\,000$ for $\alpha_p = 0.60$.

However, we can see that, for intermediate values, both coefficients are of the same order of magnitude; they both need to be taken into account in order to accurately predict the dispersion phenomenon.

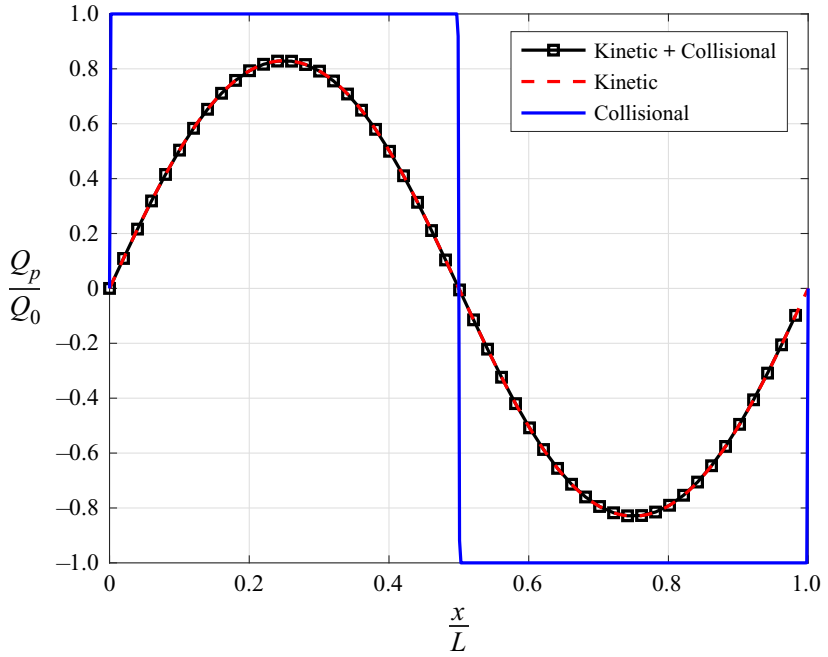

FIGURE 8. Particle charge profile at $t^* = 200$ for $\alpha_p = 0.05$.

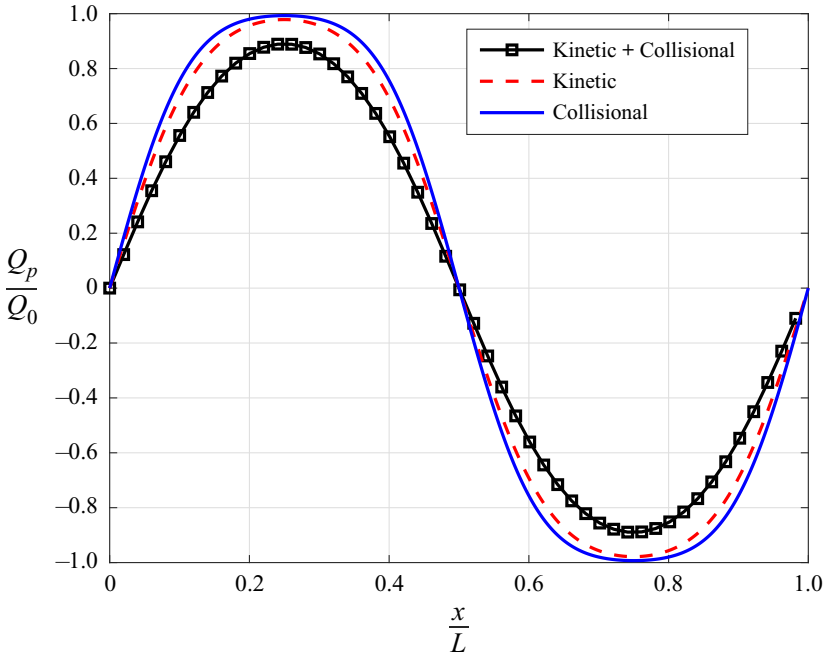

FIGURE 9. Particle charge profile at $t^* = 20\,000$ for $\alpha_p = 0.55$.

7. Triboconductivity effect

In addition to the dispersion phenomenon, we found that both the collision term (4.7) and the charge–velocity correlation (5.6) lead to electrical current density transport effects in the mean electric charge equation. These triboelectrical current density contributions obey separate mesoscopic Ohm's laws in terms of collisional and kinetic triboconductivity

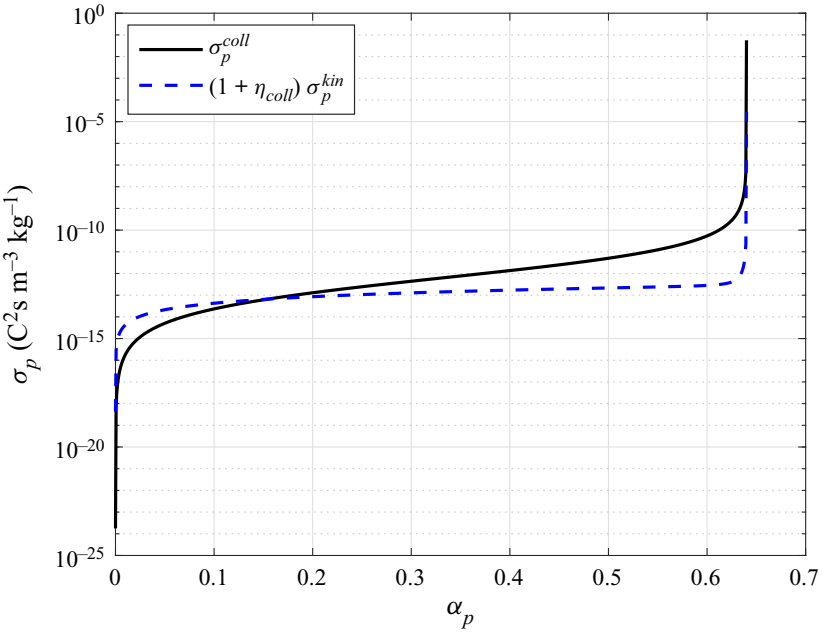

FIGURE 10. Collisional and kinetic triboconductivity coefficient.

coefficients, σ_p^{coll} and σ_p^{kin}, respectively. In figure 10, we represent both contributions as a function of the solid volume fraction. For this particular type of particle, we can see that the kinetic contribution can be dropped for high values of α_p.

The charge transport equation (5.10) for this simplified problem is written

$$n_p \frac{\partial Q_p}{\partial t} = -(\sigma_p^{coll} + (1+\eta_{coll})\sigma_p^{kin})\frac{\partial E}{\partial x} + \frac{\partial}{\partial x}\left[n_p D_p^{coll} + n_p(1+\eta_{coll})D_p^{kin}\frac{\partial Q_p}{\partial x}\right]. \quad (7.1)$$

Now, taking the divergence of (2.5), we have

$$\frac{\partial E}{\partial x} = -\frac{\partial^2 \varphi}{\partial x^2}. \quad (7.2)$$

Using (2.4), and given that the medium permittivity is constant, we obtain

$$\frac{\partial E}{\partial x} = \frac{\varrho}{\varepsilon_0}, \quad (7.3)$$

where, $\varrho = n_p Q_p$ is the volume charge density. Finally, the divergence of the electric field can be written as

$$\frac{\partial E}{\partial x} = \frac{n_p Q_p}{\varepsilon_0}. \quad (7.4)$$

This leads to a closed mean charge transport equation of the form

$$n_p \frac{\partial Q_p}{\partial t} = -n_p \frac{\sigma_p^{coll} + (1+\eta_{coll})\,\sigma_p^{kin}}{\varepsilon_0} Q_p + \frac{\partial}{\partial x}\left[n_p D_p^{coll} + n_p\,(1+\eta_{coll})\,D_p^{kin}\frac{\partial Q_p}{\partial x}\right]. \quad (7.5)$$

If we apply this equation to the simplified problem described before, we find the analytic solution (7.6). Using the same parameters as before, we can determine the dynamic

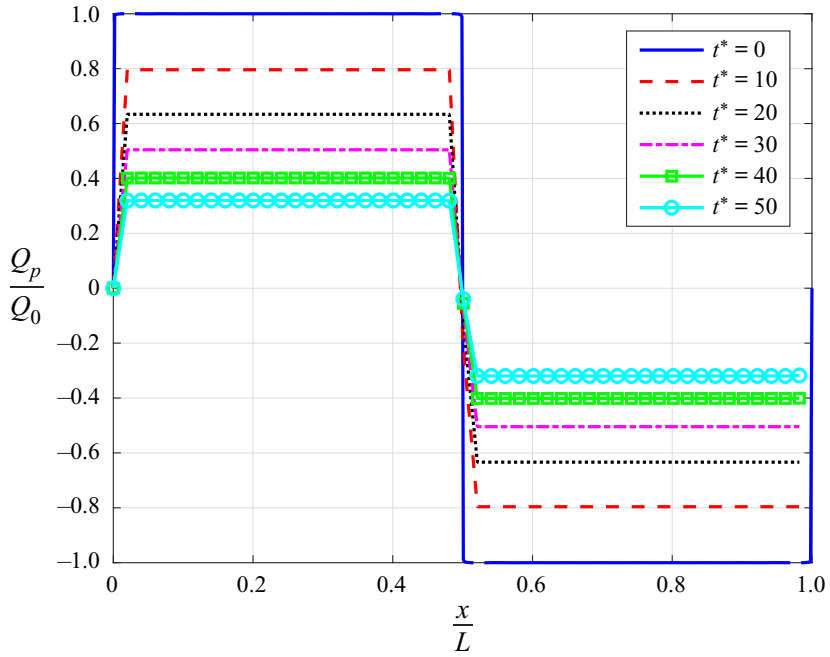

FIGURE 11. Particle charge profile as a function of x/L at different times $t^* = (\sqrt{\Theta}/d_p)t$.

evolution of the electric charge (figure 11). As we can see, the electric charge reaches the equilibrium value faster, which confirms the fact that the triboconductivity helps the redistribution of the electric charge. However, it is worth noting that the triboconductivity effect seems to be more important than the dispersion process, this was also reported in the literature (Kolehmainen *et al.* 2018).

$$Q_p = \sum_{n=1}^{\infty} \lambda_n \exp([-((\sigma_p^{coll} + (1+\eta_{coll})\sigma_p^{kin})/\varepsilon_0) - (D_p^{coll} + (1+\eta_{coll})D_p^{kin})(2\pi n/L)^2]t) \sin\left(\frac{2\pi n x}{L}\right). \tag{7.6}$$

In order to verify this, we rewrite the equation (7.5), so we make the characteristic times for the dispersion (τ_D) and the triboconductivity (τ_σ) appear. Taking l as the dispersion characteristic length, we have

$$\frac{\partial Q_p}{\partial t} = -\left((1+\eta_{coll})\frac{1}{\tau_\sigma^{kin}} + \frac{1}{\tau_\sigma^{coll}}\right) Q_p + l^2 \left((1+\eta_{coll})\frac{1}{\tau_D^{kin}} + \frac{1}{\tau_D^{coll}}\right) \frac{\partial^2 Q_p}{\partial x^2}, \tag{7.7}$$

$$\tau_\sigma = \frac{\varepsilon_0}{\sigma_p}, \tag{7.8}$$

$$\tau_D = \frac{l^2}{D_p}. \tag{7.9}$$

If we chose $l = L$, then we can represent them as a function of the solid volume fraction (figure 12). We remark that the triboconductivity characteristic time is much smaller than the dispersion characteristic time for almost all values of α_p. For dense regimes, where the

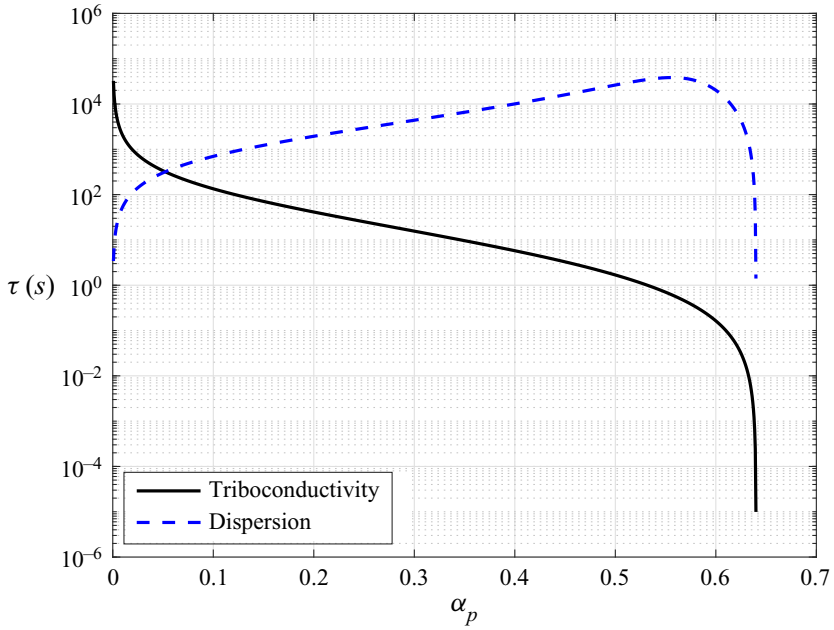

FIGURE 12. Triboconductivity and dispersion characteristic times as a function of solid volume fraction for $\Theta = 0.01$ m^2 s^{-2}.

collisional triboconductivity and dispersion coefficient are much larger than their kinetic counterparts, the ratio between these two characteristic times reduces to

$$\frac{\tau_\sigma^{coll}}{\tau_D^{coll}} \propto \left(\frac{d_p}{l}\right)^2. \tag{7.10}$$

This shows, that for dense systems, the dispersion effect is only comparable to the triboconductivity when the dispersion characteristic length scale is of the same order as the particle diameter.

8. Conclusions

In this work, we derived an Eulerian particle model for the mean electric charge equation in gas–solid flow using the framework provided by the kinetic theory of rapid granular flows. The transport equation for the mean electric charge was fully closed using less restrictive hypotheses than previous works found in the literature. The collision term in the transport equation was closed without assuming the electric charge probability density function explicitly. We proposed a linear model for the mean electric charge conditioned by the instantaneous particle velocity to account for the charge–velocity correlation. To close the charge–velocity correlation, we also derived the corresponding transport equation with the same set of hypotheses for the collision term modelling. Then, by using a series of additional hypotheses, we derived an algebraic model for the charge–velocity correlation from the corresponding transport equation. Finally, the modelled particle–particle collision term and electric charge–velocity correlation are considered in the electric charge transport equation, allowing us to identify their main effects. First of all, we found a charge dispersion phenomenon written as the sum of two separate contributions: a collisional contribution due to the electric charge transfer during particle–particle collisions and a kinetic contribution due to the transport of electric charge

by the random motion of particles. Each contribution was written using separate gradient model approximations, leading us to derive an electric charge dispersion coefficient as the sum of two separate collisional and kinetic contributions. We showed that the collisional dispersion coefficient is predominant in dense regimes and that the kinetic dispersion coefficient is the most important in dilute ones. There is, nevertheless, an intermediate region where both coefficients have to be taken into account in order to accurately predict the dispersion effect. In addition to the dispersion phenomenon, we found than both the collision term and the charge–velocity correlation lead to electrical current density transport effects in the mean electric charge transport equation. These triboelectrical current density contributions obey separate mesoscopic Ohm's laws in terms of collisional and kinetic triboconductivity coefficients, σ_p^{coll} and σ_p^{kin}, respectively. Finally, in order to determine which is more important between the dispersion and the triboelectrical current effects, we derived their characteristic times. These parameters allowed us to show that, for dense regimes, both mechanisms are of the same order of magnitude if the characteristic dispersion length scale is comparable with the particle diameter. For dilute regimes, the analysis is more complicated and depends on the particle size and physical properties, the solid fraction and the particle agitation.

Acknowledgements

This work was supported by the ANR–IPAF project, grant ANR-16-CE06-0008 of the French National Agency of Research (ANR).

Declaration of interests

The authors report no conflict of interest.

Appendix A. Integral collision coefficients

The coefficients appearing in the collision terms (4.6) and (5.5) have the following numerical values:

$$\Upsilon^{(1.1)} = \frac{2^{14/5}5}{3\times 7}\Gamma\left(\frac{3}{2}\right)\Gamma\left(\frac{12}{5}\right),$$

$$\Upsilon^{(1.2)} = \frac{2^{14/5}5}{3\times 7}\Gamma\left(\frac{12}{5}\right)\Gamma\left(\frac{3}{2}\right),$$

$$\Upsilon^{(1.3)} = \frac{2^{4/5}}{\pi^2}\Gamma\left(\frac{29}{10}\right)\Gamma\left(\frac{3}{2}\right),$$

$$\Upsilon^{(1.4)} = \frac{2^{24/5}5}{3\times 19}\Gamma\left(\frac{29}{10}\right)\Gamma\left(\frac{3}{2}\right),$$

$$\Upsilon^{(1.5)} = \frac{2^{9/5}}{\pi^2}\Gamma\left(\frac{34}{10}\right)\Gamma\left(\frac{3}{2}\right),$$

$$\Upsilon^{(2.1)} = \frac{2^3}{3}\Gamma(3)\Gamma\left(\frac{3}{2}\right),$$

$$\Upsilon^{(2.2)} = \frac{2^{24/5}5}{3\times 7}\Gamma\left(\frac{34}{10}\right)\Gamma\left(\frac{3}{2}\right),$$

$$\Upsilon^{(2.3)} = \frac{2^{14/5}5}{3\times 19}\Gamma\left(\frac{29}{10}\right)\Gamma\left(\frac{3}{2}\right),$$
$$\Upsilon^{(2.4)} = \frac{2^{14/5}5}{3\times 19}\Gamma\left(\frac{29}{10}\right)\Gamma\left(\frac{3}{2}\right),$$
$$\Upsilon^{(3.2)} = \frac{2^{24/5}5}{7}\Gamma\left(\frac{24}{10}\right)\Gamma\left(\frac{3}{2}\right),$$
$$\Upsilon^{(\xi)} = \frac{\Upsilon^{(2.4)}}{\Upsilon^{(3.2)}},$$

where Γ is the gamma function.

Appendix B. Electric charge covariance transport equation

Following the mean general transport equation (3.12), we set $\phi_p = \xi_p'\xi_p'$

$$n_p\frac{\mathrm{D}\langle\xi_p'\xi_p'\rangle}{\mathrm{D}t} + 2n_p\langle\xi_p'c_{p,i}'\rangle\frac{\partial Q_p}{\partial x_i} + \frac{\partial}{\partial x_i}(n_p\langle\xi_p'\xi_p'c_{p,i}'\rangle) = \mathcal{C}(\xi_p\xi_p) - 2Q_p\mathcal{C}(\xi_p), \tag{B 1}$$

$$\begin{aligned}\mathcal{C}(\xi_p\xi_p) = {} & d_p^3\beta E_j\frac{\partial Q_p}{\partial x_j}(\Theta_p)^{9/10}n_p^2g_0\Upsilon^{(3.1)}\\ & - d_p^2\frac{\beta}{\gamma}\langle\xi_p'\xi_p'\rangle n_p^2g_0(\Theta_p)^{9/10}\Upsilon^{(3.2)}\\ & - d_p^2\frac{\beta}{\gamma}Q_p^2n_p^2g_0(\Theta_p)^{9/10}\Upsilon^{(3.2)}\\ & + d_p^2\beta^2E_lE_jn_p^2g_0(\Theta_p)^{13/10}\Upsilon_{lj}^{(3.4)}\\ & - d_p^2E_l\frac{\beta^2}{\gamma}d_p\frac{\partial Q_p}{\partial x_j}(\Theta_p)^{13/10}n_p^2g_0\Upsilon_{lj}^{(3.5)}\\ & + d_p^2E_l\frac{\beta^2}{B}B_s(\Theta_p)^{18/10}n_p^2g_0\Upsilon_{ls}^{(3.6)}\\ & + d_p^2\left(\frac{\beta}{\gamma}\right)^2Q_pB_j(\Theta_p)^{18/10}n_p^2g_0\Upsilon_j^{(3.7)}\\ & - \frac{\partial}{\partial x_i}(-d_p^3\beta E_iQ_pn_p^2(\Theta_p)^{9/10}g_0\Upsilon^{(3.8)})\\ & + \frac{\partial}{\partial x_i}\left(d_p^3\left(\frac{\beta}{\gamma}\right)^2Q_pB_j(\Theta_p)^{18/10}g_0n_p^2\Upsilon_{ij}^{(3.9)}\right).\end{aligned} \tag{B 2}$$

Therefore, we can identify a destruction term of the electric charge covariance due to particle–particle interactions

$$n_p\frac{\partial\langle\xi_p'\xi_p'\rangle}{\partial t} + \cdots = -n_p\frac{1}{\tau_\xi}\langle\xi_p'\xi_p'\rangle + \cdots, \tag{B 3}$$

where τ_ξ is the characteristic time of electric charge covariance destruction by collisions

$$\tau_\xi = \left(\Upsilon^{(3.2)} d_p^2 \frac{\beta}{\gamma} n_p g_0 \Theta_p^{9/10} \right)^{-1}. \tag{B 4}$$

With

$$\Upsilon^{(3.2)} = \frac{2^{24/5}5}{7} \Gamma\left(\frac{24}{10}\right) \Gamma\left(\frac{3}{2}\right). \tag{B 5}$$

REFERENCES

ABBAS, M., CLIMENT, E. & SIMONIN, O. 2009 Shear-induced self-diffusion of inertial particles in a viscous fluid. *Phys. Rev.* E **79** (3), 036313.

BOELLE, A., BALZER, G. & SIMONIN, O. 1995 Second-order prediction of the particle-phase stress tensor of inelastic spheres in simple shear dense suspensions. *ASME Publications* **228**, 9–18.

CHAPMAN, S. & COWLING, T. 1970 *The Mathematical Theory of Non-Uniform Gases*, 3rd edn. Cambridge University Press.

DING, J. & GIDASPOW, D. 1990 A bubbling fluidization model using kinetic theory of granular flow. *AIChE J.* **36** (4), 523–538.

DONG, K., ZHANG, Q., HUANG, Z., LIAO, Z., WANG, J. & YANG, Y. 2015 Experimental investigation of electrostatic effect on bubble behaviors in gas-solid fluidized bed. *AIChE J.* **61** (4), 1160–1171.

FOTOVAT, F., ALSMARI, T., GRACE, J. & BI, X. 2017 The relationship between fluidized bed electrostatics and entrainment. *Powder Technol.* **316**, 157–165.

FOX, R. 2014 On multiphase turbulence models for collisional fluid–particle flows. *J. Fluid Mech.* **742**, 368–424.

GATIGNOL, R. 1983 The Faxén formulae for a rigid particle in an unsteady non-uniform Stokes flow. *Journal de Mécanique théorique et appliquée* **1** (2), 143–160.

GRAD, H. 1949 On the kinetic theory of rarefied gases. *Commun. Pure Appl. Maths* **2** (4), 331–407.

HENDRICKSON, G. 2006 Electrostatics and gas phase fluidized bed polymerization reactor wall sheeting. *Chem. Engng Sci.* **61** (4), 1041–1064.

HSIAU, S. S. & HUNT, M. L. 1993 Kinetic theory analysis of flow-induced particle diffusion and thermal conduction in granular material flows. *Trans. ASME: J. Heat Transfer* **115** (3), 541–548.

JENKINS, J. & RICHMAN, M. 1985 Grad's 13-moment system for a dense gas of inelastic spheres. *Arch Rat. Mech. Anal.* **87** (4), 355–377.

JENKINS, J. & SAVAGE, S. B. 1983 A theory for the rapid flow of identical, smooth, nearly elastic, spherical particles. *J. Fluid Mech.* **130**, 187–202.

KOLEHMAINEN, J., OZEL, A., BOYCE, C. & SUNDARESAN, S. 2017 Triboelectric charging of monodisperse particles in fluidized beds. *AIChE J.* **63** (6), 1872–1891.

KOLEHMAINEN, J., OZEL, A. & SUNDARESAN, S. 2018 Eulerian modelling of gas–solid flows with triboelectric charging. *J. Fluid Mech.* **848**, 340–369.

KRIEBITZSCH, S., VAN DER HOEF, M. & KUIPERS, J. A. M. 2013 Fully resolved simulation of a gas-fluidized bed: a critical test of DEM models. *Chem. Engng Sci.* **91**, 1–4.

LAURENTIE, J., TRAORÉ, P., DRAGAN, C. & DASCALESCU, L. 2013 Discrete element modeling of triboelectric charging of granular materials in vibrated beds. *J. Electrostat.* **71**, 951–957.

LAVIÉVILLE, J., DEUTSCH, E. & SIMONIN, O. 1995 Large eddy simulation of interactions between colliding particles and a homogeneous isotropic turbulence field. *ASME, Fluids Engng Div. (Publication) FED* **228**, 347–357.

MATSUSAKA, S. & MASUDA, H. 2003 Electrostatics of particles. *Adv. Powder Technol.* **14** (2), 143–166.

MAXEY, M. & RILEY, J. 1983 Equation of motion for a small rigid sphere in a nonuniform flow. *Phys. Fluids* **26** (10), 883–51704.

MILLER, C. & LOGWINUK, A. K. 1951 Fluidization studies of solid particles. *Ind. Engng Chem.* **43** (5), 1220–1226.

OZEL, A., DE MOTTA, J. C., ABBAS, M., FEDE, P., MASBERNAT, O., VINCENT, S., ESTIVALEZES, J-L. & SIMONIN, O. 2017 Particle resolved direct numerical simulation of a liquid–solid fluidized bed: comparison with experimental data. *Intl J. Multiphase Flow* **89**, 228–240.

RAY, M., CHOWDHURY, F., SOWINSKI, A., MEHRANI, P. & PASSALACQUA, A. 2019 An Euler-Euler model for mono-dispersed gas-particle flows incorporating electrostatic charging due to particle-wall and particle-particle collisions. *Chem. Engng Sci.* **197**, 327–344.

ROKKAM, R., FOX, R. & MUHLE, M. 2010 Computational fluid dynamics and electrostatic modeling of polymerization fluidized-bed reactors. *Powder Technol.* **203** (2), 109–124.

ROKKAM, R., SOWINSKI, A., FOX, R., MEHRANI, P. & MUHLE, M. 2013 Computational and experimental study of electrostatics in gas-solid polymerization fluidized beds. *Chem. Engng Sci.* **92**, 146–156.

SALAMA, F., SOWINSKI, A., ATIEH, K. & MEHRANI, P. 2013 Investigation of electrostatic charge distribution within the reactor wall fouling and bulk regions of a gas-solid fluidized bed. *J. Electrostat.* **71** (1), 21–27.

SIMONIN, O., FÉVRIER, P. & LAVIÉVILLE, J. 2002 On the spatial distribution of heavy-particle velocities in turbulent flow: from continuous field to particulate chaos. *J. Turbul.* **3** (1), 1–40.

SOWINSKI, A., MILLER, L. & MEHRANI, P. 2010 Investigation of electrostatic charge distribution in gas-solid fluidized beds. *Chem. Engng Sci.* **65** (9), 2771–2781.

SOWINSKI, A., SALAMA, F. & MEHRANI, P. 2009 New technique for electrostatic charge measurement in gas-solid fluidized beds. *J. Electrostat.* **67** (4), 568–573.

ZHOU, Y., REN, C., WANG, J., YANG, Y. & DONG, K. 2013 Effect of hydrodynamic behavior on electrostatic potential distribution in gas-solid fluidized bed. *Powder Technol.* **235**, 9–17.

Chapter 3

Eulerian modeling of particle charge-velocity covariance and particle charge variance

3.1 Introduction

In the previous section, we derived the transport equation for the mean electric charge of particles. The particle charge-velocity covariance term in this equation was closed using a simple algebraic model. However, in order to derive this algebraic model, we had to neglect several terms that could be important in certain situations. More specifically, we dropped the terms related to the particle mean velocity gradient and the covariance transport due to the random motion of particles. These terms could become dominant in high shear flow or in high dilute configurations (Simonin et al., 1995; Wang et al., 1998). In addition to this, the charge variance term was completely neglected, without evaluating in which situations this assumption is valid.

Therefore, in this chapter, we extend the previous approach to a more complete description. In particular, we will study a model retaining the full transport equations for the two second order moments: the charge-velocity covariance and the charge variance. In addition to this, we will show that the kinetic theory of granular flow can be used to derive simple algebraic closure law for the third order moments.

3.2 Particle velocity-charge covariance transport equation

The particle velocity-charge covariance transport equation can be derived using the general mean transport equation for a property ϕ with $\phi = \xi_p' c_{p,i}'$.

$$
\begin{aligned}
n_p \frac{D\left\langle \xi_p' c_{p,i}' \right\rangle}{Dt} + \frac{\partial n_p \left\langle \xi_p' c_{p,i}' c_{p,j}' \right\rangle}{\partial x_j} + n_p R_{p,ij} \frac{\partial Q_p}{\partial x_j} + n_p \left\langle c_{p,j}' \xi_p' \right\rangle \frac{\partial U_{p,i}}{\partial x_j} \\
= n_p \left\langle \frac{1}{m_p} \left\langle F_i \mid \mathbf{x}, \mathbf{c_p}, \xi_p \right\rangle \xi_p' \right\rangle + \mathcal{C}\left(\xi_p c_{p,i}'\right) - Q_p \mathcal{C}\left(c_{p,i}'\right),
\end{aligned}
\tag{3.1}
$$

Similarly to the previous chapter, the force term is expanded as:

$$
\begin{aligned}
\left\langle \frac{1}{m_p} \left\langle F_i \mid \mathbf{x}, \mathbf{c_p}, \xi_p \right\rangle \xi_p' \right\rangle = & - \left\langle \frac{V_p}{m_p} \left\langle \frac{\partial P_{g@p}}{\partial x_i} \mid \mathbf{x}, \mathbf{c_p}, \xi_p \right\rangle \xi_p' \right\rangle \\
& - \left\langle \frac{1}{\tau_p} \left(c_{p,i} - \left\langle u_{g@p,i} \mid \mathbf{x}, \mathbf{c_p}, \xi_p \right\rangle \right) \xi_p' \right\rangle \\
& + \left\langle g_i \xi_p' \right\rangle + \left\langle \frac{1}{m_p} \xi_p' \xi_p E_i \right\rangle.
\end{aligned}
\tag{3.2}
$$

We will assume that the fluid pressure and velocity are not correlated with the particles electric charge and velocity. We will also consider that the macroscopic electric field is not correlated with the particle fluctuant electric charge. With these hypotheses, the force term reduces to:

$$
\left\langle \frac{1}{m_p} \left\langle F_i \mid \mathbf{x}, \mathbf{c_p}, \xi_p \right\rangle \xi_p' \right\rangle = -\frac{1}{\overline{\tau_p}} \left\langle c_{p,i}' \xi_p' \right\rangle + \frac{1}{m_p} \left\langle \xi_p' \xi_p' \right\rangle E_i,
\tag{3.3}
$$

The collision terms in the RHS of equation 3.1 were already derived in the previous chapter:

$$
\begin{aligned}
\mathcal{C}\left(\xi_p c_{p,i}'\right) - Q_p \mathcal{C}\left(c_{p,i}'\right) = & -\frac{1+e_c}{3} \frac{1}{\tau_c} n_p \langle \xi_p' c_{p,i}' \rangle - \frac{3-e_c}{5} \frac{1}{\tau_\xi} n_p \langle \xi_p' c_{p,i}' \rangle \\
& + \lambda_{2.1} e_c \frac{\sqrt{\Theta_p}}{d_p} \sigma_p^{coll} E_i - \lambda_{2.2} e_c n_p \frac{\sqrt{\Theta_p}}{d_p} D_p^{coll} \frac{\partial Q_p}{\partial x_i}.
\end{aligned}
\tag{3.4}
$$

With $\lambda_{2.1} \approx 0.5422$ and $\lambda_{2.2} \approx 0.5422$

We recall that τ_c is the characteristic particle-particle collision time and τ_ξ is the characteristic time of destruction of the particle charge variance:

$$
\tau_c = \left(4\sqrt{\pi} n_p g_0 d_p^2 \sqrt{\Theta_p}\right)^{-1}
\tag{3.5}
$$

$$\tau_\xi = \left(\lambda_{2.3} n_p g_0 d_p^2 \gamma \Theta_p^{9/10}\right)^{-1} \tag{3.6}$$

with $\lambda_{2.3} \approx 21.90$

Similarly to the mean charge transport equation, the covariance transport equation depends on a higher order statistical moment: $\langle \xi_p' c_{p,i}' c_{p,j}' \rangle$, which represents the transport of the charge-velocity covariance due to the random motion of particles. In this study, we propose a simple closure modeling for this term based on a simplification of its transport equation, following the methodology developed by Sakiz and Olivier (1999). First, we set $\phi = \xi_p' c_{p,i}' c_{p,j}'$ in the general mean transport equation. Then, after solving the collision integrals, we reduce the transport equation to an algebraic equation using a series of simplifying hypotheses. From this equation, we can deduce an simple algebraic model for the third order moment (see appendix 3.A for a detailed derivation):

$$\langle \xi_p' c_{p,i}' c_{p,j}' \rangle = \frac{1}{K_1} D_{ij} - \frac{K_2}{K_1 \left(K_1 + 3K_2\right)} D_{mm} \delta_{ij} \tag{3.7}$$

with

$$K_1 = n_p \left[\frac{1}{\tau_c} \left(\lambda_{2.4} \left(1 + e_c\right) - \lambda_{2.5} \left(1 + e_c\right)^2 \right) + \frac{1}{\tau_p} + \lambda_{2.6} \frac{1}{\tau_\xi} \right], \tag{3.8}$$

$$K_2 = -\frac{n_p}{\tau_c} \left[-\lambda_{2.7} \left(1 + e_c\right) + \lambda_{2.8} \left(1 + e_c\right)^2 \right], \tag{3.9}$$

$$\begin{aligned} D_{ij} = & -n_p R_{p,jk} \frac{\partial \langle \xi_p' c_{p,i}' \rangle}{\partial x_k} - n_p R_{p,ik} \frac{\partial \langle \xi_p' c_{p,j}' \rangle}{\partial x_k} \\ & - n_p d_p \Theta_p^{1/2} \left(1 + e_c\right) \frac{1}{\tau_\xi} \left[\lambda_{2.9} \frac{\partial \left\langle \xi_p' c_{p,i}' \right\rangle}{\partial x_j} + \lambda_{2.9} \frac{\partial \left\langle \xi_p' c_{p,j}' \right\rangle}{\partial x_i} + \lambda_{2.10} \frac{\partial \left\langle \xi_p' c_{pn}' \right\rangle}{\partial x_n} \delta_{ij} \right] \\ & - \lambda_{2.11} n_p d_p \Theta_p^{1/2} \left(1 + e_c\right)^2 \frac{1}{\tau_\xi} \left[\frac{\partial \left\langle \xi_p' c_{pn}' \right\rangle}{\partial x_n} \delta_{ij} + \frac{\partial \left\langle \xi_p' c_{p,i}' \right\rangle}{\partial x_j} + \frac{\partial \left\langle \xi_p' c_{p,j}' \right\rangle}{\partial x_i} \right]. \end{aligned} \tag{3.10}$$

With $\lambda_{2.4} \approx 6.667$, $\lambda_{2.5} \approx 1.387$, $\lambda_{2.6} \approx 3.201$, $\lambda_{2.7} \approx 0.2667$, $\lambda_{2.8} \approx 0.2607$, $\lambda_{2.9} \approx 10.68$, $\lambda_{2.10} \approx 208.2$, and $\lambda_{2.11} \approx 0.2048$

We remark that, according to this algebraic model, the third order moment $\langle \xi_p' c_{p,i}' c_{p,j}' \rangle$ contains a term involving product between some characteristic time, the kinetic stress tensor and the gradient of the lower moments $\langle \xi_p' c_{p,i}' \rangle$ and $\langle \xi_p' c_{p,j}' \rangle$. This shows that, using some simplifying hypothesis, a high order moment can be modeled as being proportional to the gradient of the lower order moment.

3.3 Particle charge variance transport equation

The electrostatic force in the particle velocity-charge covariance equation introduces a second term that needs to be modeled: the particle charge variance $\langle \xi'_p \xi'_p \rangle$. Similarly to the covariance term, we can model the variance by writing its transport equation. Using the general mean transport equation with $\phi = \xi'_p \xi'_p$, we obtain:

$$n_p \frac{D\left\langle \xi'_p \xi'_p \right\rangle}{Dt} + 2n_p \left\langle \xi'_p c'_{p,i} \right\rangle \frac{\partial Q_p}{\partial x_i} + \frac{\partial n_p \left\langle \xi'_p \xi'_p c'_{p,i} \right\rangle}{\partial x_i} = \mathcal{C}\left(\xi_p \xi_p\right) - 2Q_p \mathcal{C}\left(\xi_p\right). \tag{3.11}$$

To be consistent with the covariance equation, we calculated the collision terms in the above equation neglecting the mean particle velocity gradient, the granular temperature gradients and any cross product term between Q_p, E_i, $\langle \xi'_p c'_{p,i} \rangle$. This led us to the following expression:

$$\begin{aligned} \mathcal{C}\left(\xi_p \xi_p\right) - 2Q_p \mathcal{C}\left(\xi_p\right) = n_p \left(-\frac{1}{\tau_\xi} + \lambda_{3.1} \left(D_p^{coll}\right)^2 \frac{\tau_c}{d_p^4} \right) \left\langle \xi'_p \xi'_p \right\rangle \\ + \lambda_{3.2} \left(\sigma_p^{coll}\right)^2 \frac{\tau_c}{n_p d_p^2} E_i E_i + \frac{\partial}{\partial x_i} \left[\lambda_{3.3} n_p \left(D_p^{coll}\right)^2 \frac{\tau_c}{d_p^2} \frac{\partial \left\langle \xi'_p \xi'_p \right\rangle}{\partial x_i} \right]. \end{aligned} \tag{3.12}$$

Where $\lambda_{3.1} \approx 21.29$, $\lambda_{3.2} \approx 14.20$ and $\lambda_{3.3} \approx 0.6278$

Like the particle velocity-charge covariance transport equation, the charge variance equation depends on the higher order moment $\langle \xi'_p \xi'_p c'_{p,i} \rangle$, which represents the transport of the electric charge variance due to the random motion of particles. Using the approach taken to model $\langle \xi'_p c'_{p,i} c'_{p,j} \rangle$, we can also derive an algebraic model for this high order moment (see appendix 3.B)

$$n_p \langle \xi'_p \xi'_p c'_{p,i} \rangle = -\frac{n_p R_{p,ij}}{\frac{1}{3}\left(1+e_c\right)\frac{1}{\tau_c} + \frac{1}{\tau_p} + \left(\lambda_{3.4} - \lambda_{3.5}\gamma\Theta_p^{2/5}\right)\frac{1}{\tau_\xi}} \frac{\partial \langle \xi'_p \xi'_p \rangle}{\partial x_j} \tag{3.13}$$

with $\lambda_{3.4} \approx 2.806$ and $\lambda_{3.5} \approx 1.017$

As stated before, we can model this third order moment $\langle \xi'_p \xi'_p c'_{p,i} \rangle$ as being proportional to the gradient of the second order moment $\langle \xi'_p \xi'_p \rangle$.

Equations 3.1, 3.7, 3.11, and 3.13 give us a more complete closure modeling for the covariance term in the mean electric charge transport equation. This approach uses the full transport equations for the two second order moments $\langle \xi_p' c_{p,i}' \rangle$ and $\langle \xi_p' \xi_p' \rangle$ coupled with two algebraic closure laws for the thrid order moments $\langle \xi_p' c_{p,i}' c_{p,j}' \rangle$ and $\langle \xi_p' \xi_p' c_{p,i}' \rangle$.

3.4 Case of study

In order to gain a better understanding of the dynamics imposed by this set of equations, we will solve these equation in the simple configuration already used in the previous chapter. As a reminder, this test case consists in a 3D periodic box of length L. The particle density number is constant and uniform inside the domain. The mean fluid and particle velocities are zero. And the particles have an uniform constant granular temperature Θ_p. At $t = 0$ the particles have a non-uniform electric charge distribution with particle positively charged on the left and negatively charge on the right (equation 3.14). If needed, the initial condition for particle velocity-charge covariance ($\langle c_{p,i}' \xi_p' \rangle$) and particle charge variance ($\langle \xi_p' \xi_p' \rangle$) are set to 0.

$$Q_p\left(t = 0s\right) = -Q_{p,0} \sin\left(2\pi \frac{x}{L}\right) \tag{3.14}$$

3.4.1 Dimensionless analysis

Given the simplicity of this system, we can rewrite the governing equations in a simpler dimensionless form. We can choose $L_{\text{ref}} = L$ as reference length, $Q_{p,\text{ref}} = Q_{p,0}$ as reference electric charge, $U_{p,\text{ref}} = \sqrt{\Theta_p}$ as reference velocity, $t_{\text{ref}} = {}^{L}/\sqrt{\Theta_p}$ as reference time, and $E_{\text{ref}} = {}^{n_p Q_{p,\text{ref}} L}/_{\varepsilon_0}$ as reference electric field. Using these characteristic scales, we can express the governing equations as:

1. The dimensionless mean particle charge transport equation:

$$\frac{\partial Q_p^*}{\partial t^*} + \left(1 + \eta_{coll}\right) \frac{\partial \left\langle c_p^{*\prime} \xi_p^{*\prime} \right\rangle}{\partial x^*} = -\frac{1}{\tau_\sigma^*} \frac{\partial E^*}{\partial x^*} + \frac{1}{Pe} \frac{\partial^2 Q_p^*}{\partial x^{*2}} \tag{3.15}$$

2. The dimensionless particle velocity-charge covariance transport equation:

$$\frac{\partial \left\langle c_p^{*\prime} \xi_p^{*\prime} \right\rangle}{\partial t^*} + \left(1 + \lambda_{2.2} e_c \frac{1}{Pe} \frac{L}{d_p}\right) \frac{\partial Q_p^*}{\partial x^*} - \lambda_{2.1} e_c \frac{1}{\tau_\sigma^*} \frac{L}{d_p} E^* - \frac{u_e}{u_k} \langle \xi_p^{*\prime} \xi_p^{*\prime} \rangle E^* = \\ - \left(\frac{1+e_c}{3} \frac{1}{\tau_c^*} + \frac{1}{\tau_p^*} + \frac{3-e_c}{5} \frac{1}{\tau_\xi^*} \right) \left\langle c_p^{*\prime} \xi_p^{*\prime} \right\rangle + \left[2 + \frac{1}{\tau_\xi^*} \frac{L}{d_p} \left(2\lambda_{2.9} + \lambda_{2.10}\right)(1+e_c) \right. \\ \left. + 3\lambda_{2.11} \frac{1}{\tau_\xi^*} \frac{L}{d_p} (1+e_c)^2 \right] \frac{1}{K_1 + K_2} \frac{\partial^2 \langle \xi_p^{*\prime} c_p^{*\prime} \rangle}{\partial x^{*2}} \tag{3.16}$$

3. The dimensionless particle charge variance transport equation:

$$\frac{\partial \left\langle \xi_p^{*\prime} \xi_p^{*\prime} \right\rangle}{\partial t^*} + 2 \left\langle \xi_p^{*\prime} c_p^{*\prime} \right\rangle \frac{\partial Q_p^*}{\partial x^*} = \left(-\frac{1}{\tau_\xi^*} + \lambda_7 \frac{1}{Pe^2} \tau_c^* \left(\frac{L}{d_p}\right)^4 \right) \left\langle \xi_p^{*\prime} \xi_p^{*\prime} \right\rangle \\ + \lambda_8 \frac{\tau_c^*}{\tau_\sigma^2} \left(\frac{L}{d_p}\right)^2 |E^*|^2 + \lambda_9 \frac{1}{Pe^2} \tau_c^* \left(\frac{L}{d_p}\right)^2 \frac{\partial^2 \left\langle \xi_p^{*\prime} \xi_p^{*\prime} \right\rangle}{\partial x^{*2}} \\ + \left[\frac{1+e_c}{3} \frac{1}{\tau_c^*} + \frac{1}{\tau_p^*} + \frac{1}{\tau_\xi^*} \left(2.8 - 20.39 \frac{1}{Pe} \tau_c^* \left(\frac{L}{d_p}\right)^2 \right) \right]^{-1} \frac{\partial^2 \left\langle \xi_p^{*\prime} \xi_p^{*\prime} \right\rangle}{\partial x^{*2}} \tag{3.17}$$

And the dimensionless Maxwell equations can be written as:

$$E^* = -\nabla \phi^* \tag{3.18}$$

$$\nabla^2 \phi^* = -Q_p^* \tag{3.19}$$

Where the dimensionless variables Q_p^*, E^*, x^* and t^* are given by:

$$Q_p^* = \frac{Q_p}{Q_{p,0}} \tag{3.20}$$

$$x^* = \frac{x}{L} \tag{3.21}$$

$$t^* = t \frac{\sqrt{\Theta_p}}{L} \tag{3.22}$$

$$E^* = \frac{E}{E_{\text{ref}}} \tag{3.23}$$

And the 7 dimensionless parameters are expressed as:

$$Pe = \frac{L\sqrt{\Theta_p}}{D_p^{coll}} \quad (3.24) \qquad \tau_\sigma^* = \frac{\varepsilon_0}{\sigma_p^{coll}}\frac{\sqrt{\Theta_p}}{L} \quad (3.25)$$

$$\tau_c^* = \tau_c\frac{\sqrt{\Theta_p}}{L} \quad (3.26) \qquad \tau_p^* = \tau_p\frac{\sqrt{\Theta_p}}{L} \quad (3.27)$$

$$\frac{u_e}{u_k} = \frac{\frac{1}{2}\varepsilon_0 E_{ref}^2}{\frac{1}{2}n_p m_p \Theta_p} \quad (3.28) \qquad \frac{L}{d_p} \quad (3.29)$$

$$e_c \quad (3.30)$$

This non-dimensionalization process have revealed that the original system of equations can be expressed as a function of 7 independent dimensionless parameters: Pe, τ_c^*, τ_p^*, τ_σ^*, L/d_p, u_e/u_k and e_c. The dimensionless parameters τ_ξ^* and η_{coll} can be written as a function of the previous dimensionless parameters:

$$\tau_\xi^* = \lambda' Pe \left(\frac{d_p}{L}\right)^2 \quad (3.31)$$

$$\eta_{coll} = \lambda'' \frac{1}{Pe}\frac{L}{d_p} \quad (3.32)$$

with $\lambda' = 12$ and $\lambda'' \approx 3.256$

Contrary to the previous chapter's model, an analytical solution cannot be derived for this more complex approach. Therefore, we solve these equations using an explicit adaptive Runge-Kutta method of 7th order (Fehlberg, 1968). All the spatial derivatives are approximated with a 8th central finite difference scheme.

3.5 Two transport equations model

Analyzing equation 3.16, we notice that the charge variance term could be neglected if the fluctuant kinetic energy is much higher than the electrostatic potential energy. In this case, the particle charge variance equation is not longer needed and the system is governed only by equations 3.15 and 3.16. We will start by analyzing this simpler configuration.

Previous works have already proposed an simpler model to take into account the particle velocity-charge covariance. Their formulation consisted in a simpler algebraic gradient model

derived by analogy with the temperature kinetic dispersion coefficient (Kolehmainen et al., 2018) or by simplifying the covariance transport equation (Montilla et al., 2020; Ray et al., 2019). As stated before, the formulation proposed by Montilla et al. (2020) is, to the best of our knowledge, the most general formulation proposed until now. Because it is based on a less strict formulation for the particle probability density function. So we will compare our formulation against their algebraic gradient model.

We will study when this algebraic model can be considered as a valid simplification. We recall that, in order to obtain the charge-velocity covariance algebraic model, we have to assume an instantaneous steady state and we also have to neglect the effect of the mean shear stress and the covariance kinetic dispersion effects. By definition, our test case has no mean shear stress. However, the other two effects could not be negligible in some configurations. Analyzing the dimensionless covariance transport equation (equation 3.16), we can rewrite it as:

$$\frac{\partial \langle c_p^{*\prime} \xi_p^{*\prime} \rangle}{\partial t^*} + \frac{1}{\tau_{cov}^*} \langle c_p^{*\prime} \xi_p^{*\prime} \rangle = D_p^{cov} \frac{\partial^2 \langle c_p^{*\prime} \xi_p^{*\prime} \rangle}{\partial x^{*2}} + \mathcal{H} \tag{3.33}$$

Here, τ_{cov}^* is the covariance characteristic time, D_p^{cov} is the covariance dispersion coefficient, and $\mathcal{H}$ are the covariance production or destruction terms associated with the mean electric charge gradient and the macroscopic electric field. As we mentioned, the algebraic gradient model is derived assuming an instantaneous steady state. This is equivalent to say that the covariance characteristic time is very small ($\tau_{cov}^* \ll 1$). Also the algebraic model neglects the effects of the covariance transport due to the random motion of particles ($D_p^{cov} \ll 1$). We can express these conditions as:

$$\left(\frac{1 + e_c}{3} \frac{1}{\tau_c^*} + \frac{1}{\tau_p^*} + \frac{3 - e_c}{5} \frac{1}{\tau_\xi^*} \right) \gg 1 \tag{3.34}$$

$$\left[2 + \frac{1}{\tau_\xi^*} \frac{L}{d_p} \left(2\lambda_{2.9} + \lambda_{2.10} \right) (1 + e_c) + 3\lambda_{2.11} \frac{1}{\tau_\xi^*} \frac{L}{d_p} (1 + e_c)^2 \right] \frac{1}{K_1 + K_2} \ll 1 \tag{3.35}$$

This was confirmed by comparing the solution given by the two models when the dimensionless parameters are set to: $\tau_c^* = 10^{-4}$, $Pe = 10^2$, $\tau_\sigma^* = \infty$, $\tau_p = \infty$, $e_c = 1$, and $L/d_p = 192$. Figures 3.1 and 3.2 show how the particle electric charge and the velocity charge covariance evolve as function of time. The dashed line represents the solution given when solving the two transport equations, while the round markers show the solution given the algebraic gradient model. As we can see both model predict the same electric charge and covariance profiles for all time steps, except the initial condition. The initial condition when

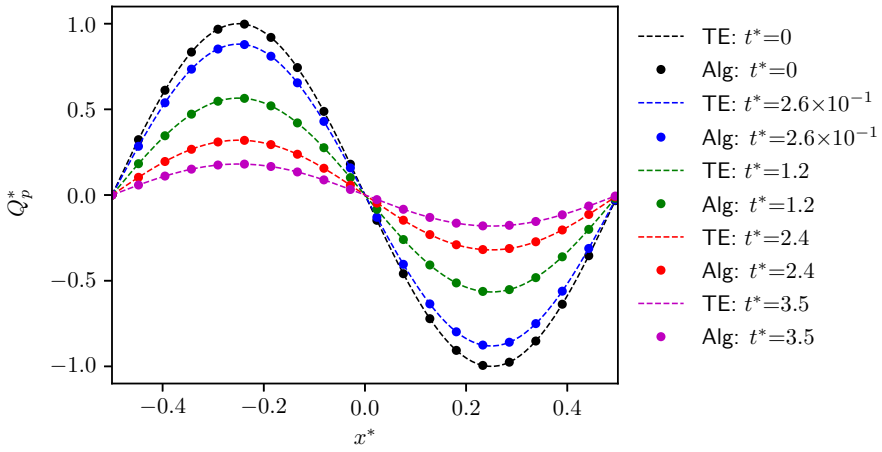

Figure 3.1: Particle dimensionless electric charge evolution as a function of time. Comparison between the algebraic model and the two transport equations model

solving the full transport equation is set to $\langle \xi_p^{*\prime} c_p^{*\prime} \rangle = 0$ while the covariance initial condition when using the algebraic model is given by the algebraic model itself. We can study the first time steps of the simulation to see how these two system become equivalent. Figure 3.3 the covariance evolution during the first 5 time steps. Again, the dashed line represents the solution of the two transport equation and the marker represents the solution of the algebraic model, which remains almost constant during those time steps. This figure shows that the transport equation model reaches the steady state very quickly compared to the particle electric charge characteristic response time. After this equilibrium is reached the two model behave identically.

The covariance algebraic model can fail due to two different reasons: either the equilibrium is not reached fast enough, or the covariance dispersion term is not negligible. This can be achieved by setting the system's dimensionless parameters to: $Pe = 100$, $\tau_c^* = 100$, $\tau_\sigma^* = 100,000$, $e_c = 1$, $\tau_p^* = \infty$, and $^L/_{d_p} = 192$ Figures 3.4 and 3.5 illustrate the system's dynamics for this configuration. In this case, the covariance transport equation response time is comparable to the electric charge response time. We appreciate, in the covariance figure, that the rising velocity of the covariance profile is not fast enough to reach the equilibrium condition quickly. In addition to this, the dispersion effect, given by the modeling of the third order moment, decreases the maximum covariance value. In conclusion, we can say that, when used outside its validity region, defined by equations 3.34 and 3.35, the algebraic model could overestimate the charge-velocity covariance profile by neglecting the kinetic dispersion term and assuming a quasi-steady state. This overestimation of the covariance

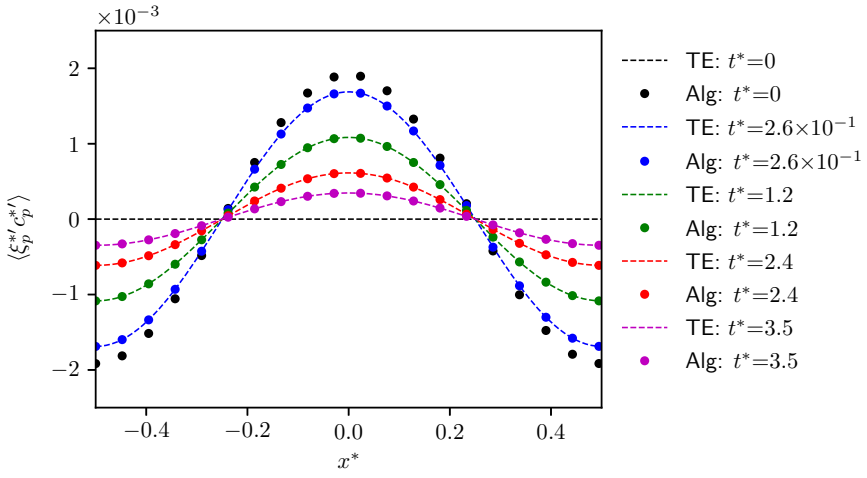

Figure 3.2: Particle dimensionless velocity-charge covariance evolution as a function of time. Comparison between the algebraic model and the two transport equations model.

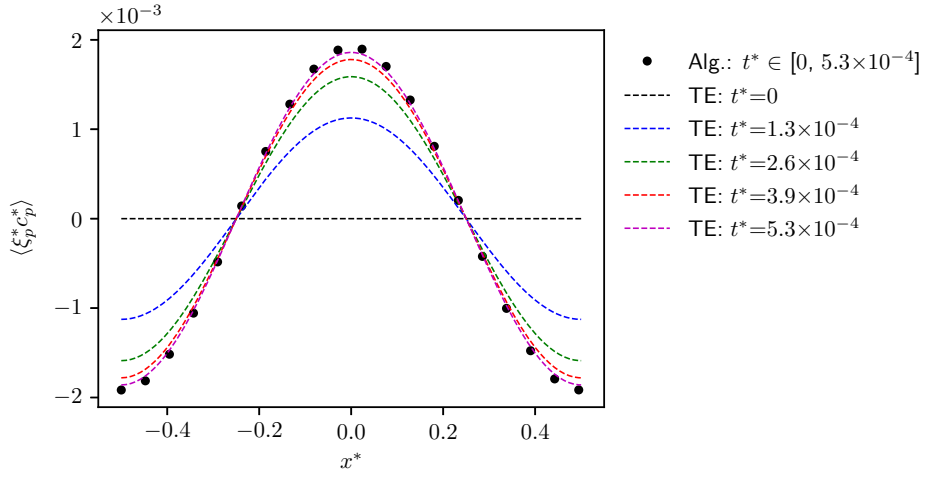

Figure 3.3: Particle dimensionless velocity-charge covariance evolution during the first time steps.

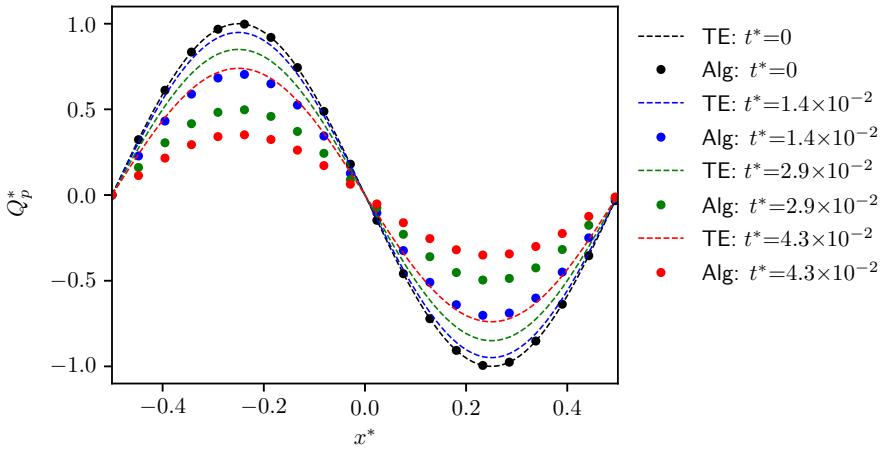

Figure 3.4: Dimensionless particle electric charge evolution as a function of time.

term leads also to an overestimation of the kinetic dispersion of the mean electric charge.

3.6 Three transport equation model

As stated at the beginning of the previous section, the particle electric charge variance term could become important as the potential electric density energy increases. Under these circumstances, the three equations must be solved in order to correctly predict the mean particle electric charge dynamics. To illustrate the effect of the charge variance, we will study a system with the following parameter $Pe = 10^5$, $\tau_\sigma^* = \infty$, $\tau_c^* = 10^{-4}$, ${}^{u_e}/_{u_k} = 300$, $\tau_p^* = \infty$, $e_c = 1$ and ${}^{L}/_{d_p} = 192$. We will compare the full three transport equations model and the simpler model where the charge variance is neglected ($\langle \xi_p^{*\prime} \xi_p^{*\prime} \rangle = 0$) and therefore only 2 transport equations are needed.

Figure 3.6 shows a snapshot of the particle mean electric charge, the macroscopic electric field, the velocity-charge covariance and the electric charge variance at $t^* = 30$. We can observe that taking into account the variance effects significantly changes the system's dynamics. Starting with the electric charge variance, we observe a profile with several peaks. Analyzing the contribution of each term in equation 3.17, we found that the most important production term is the second term in the left-hand side. Indeed, we remark in figure 3.6d, that the regions with high electric charge variance correspond to the zones with high particle velocity-charge covariance and high particle charge gradient. Conversely, the regions with

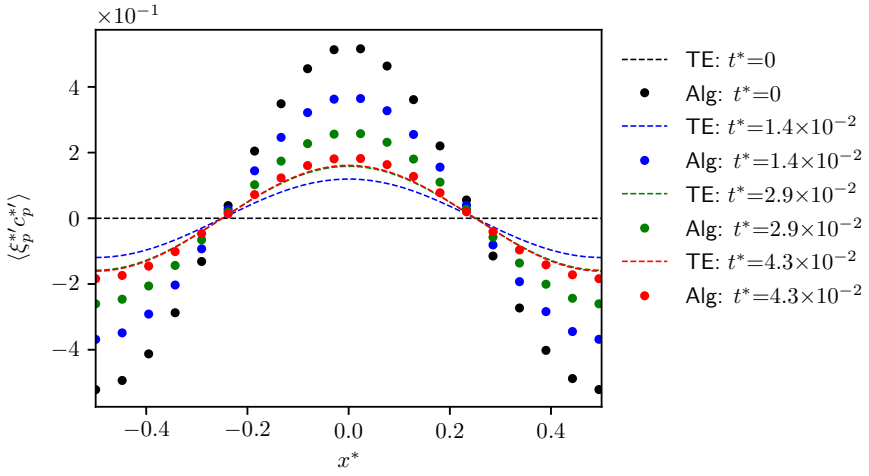

Figure 3.5: Dimensionless particle velocity-charge covariance evolution as a function of time.

low particle charge variance are found where the velocity-charge covariance or the charge gradient are zero.

This variance term has a noticeable effect in the covariance profile. Equation 3.16 shows that the electrostatic force term can produce or destroy the particle velocity-charge covariance depending on the alignment of the macroscopic electric field with the covariance vector. If the electric field is aligned with the covariance, we will have an increase in the particle electric charge flux due to the transport generated by the electrostatic force. Figure 3.6c shows that the charge variance term enhances the particle velocity-charge covariance profile, especially in the zones where the electric field is strong. The effect of this additional flux term are also clear in the electric charge profile (figure 3.6a). We can see that the charge has dispersed faster compared with a simpler no variance model.

This more complete model approach has revealed the importance of the correct modeling of the electric charge variance, specifically when the potential electric energy of the system is much higher than the fluctuant kinetic energy. The electric charge flux created by the electrostatic forces should not be neglected in this situation if we want to correctly predict the electric charge dynamics. However, the mathematical model presented here, is much more complex as it requires to simultaneously solve multiple coupled partial differential equations. In the following sections, we would like to explore possible simplifications to this model while keeping charge variance effects.

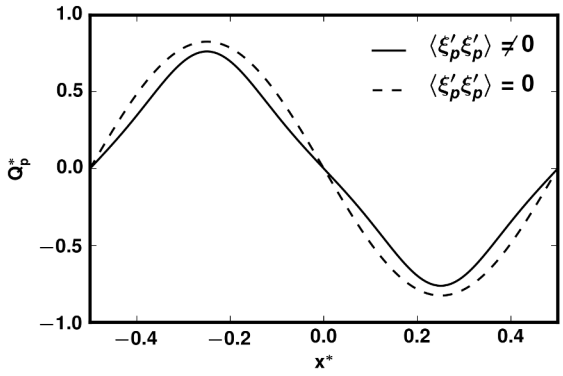

(a) Dimensionless particle electric charge

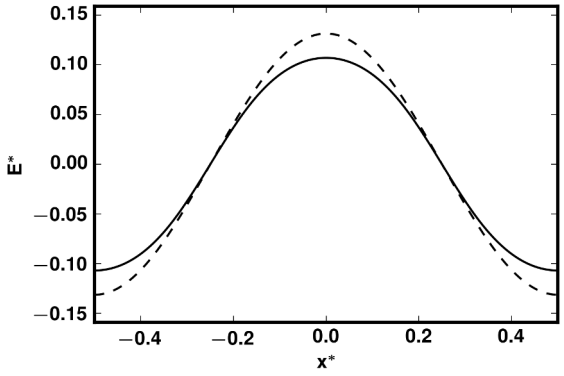

(b) Dimensionless electric field

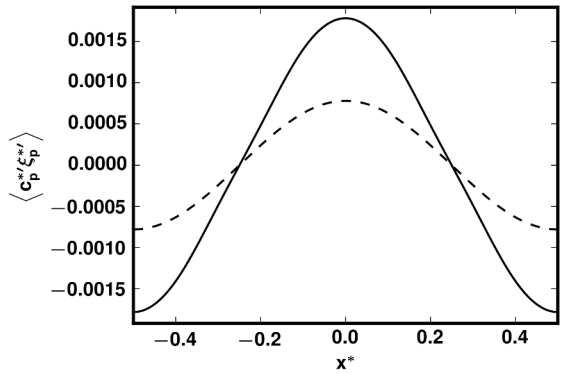

(c) Dimensionless particle velocity-charge covariance

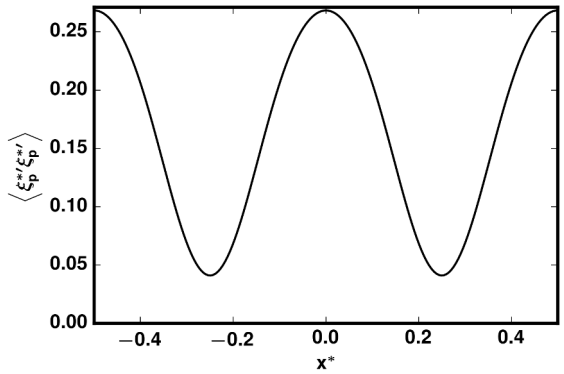

(d) Dimensionless particle electric charge variance

Figure 3.6: Comparison between the full 3 transport equations model and the 2 transport equations models where the variance in neglected.

3.7 Coupled algebraic model

A simpler approach could be to try to extend the algebraic model proposed by Montilla et al. (2020) to take into account the electric charge variance. This will reduce the model to a single partial differential equation with 2 algebraic expression for the charge velocity-covariance and the charge variance. In order to obtain this more general algebraic model, we can follow the methodology used to derive the previous algebraic model. First, we simplify the charge-velocity covariance and the charge variance equations neglecting the contributions of the Lagrangian derivative, the velocity gradient, the third order moments and the dispersion terms. This reduces the covariance transport equation (equation 3.1) and the variance transport equation (equation 3.11) to the following system of algebraic equations:

$$\begin{cases} D_1 \langle c'_{p,i} \xi'_p \rangle + D_{2,i} \langle \xi'_p \xi'_p \rangle = D_{3,i} \\ F_{1,i} \langle c'_{p,i} \xi'_p \rangle + F_2 \langle \xi'_p \xi'_p \rangle = F_3 \end{cases} \tag{3.36}$$

where

$$D_1 = \frac{1 + e_c}{3} \frac{1}{\tau_c} + \frac{1}{\tau_p} + \frac{2\,(3 - e + c)}{5} \frac{1}{\tau_\xi} \tag{3.37}$$

$$D_{2,i} = -\frac{n_p}{m_p} E_i \tag{3.38}$$

$$D_{3,i} = -\left(1 + \lambda_{2.2} e_c \frac{\sqrt{\Theta_p}}{d_p} D_p^{coll} \right) n_p \frac{\partial Q_p}{\partial x_i} + \lambda_{2.1} e_c \frac{\sqrt{\Theta_p}}{d_p} \sigma_p^{coll} E_i \tag{3.39}$$

$$F_{1,i} = 2 n_p \frac{\partial Q_p}{\partial x_i} \tag{3.40}$$

$$F_2 = n_p \left(\frac{1}{\tau_{xi}} - \lambda_{3.1} \left(D_p^{coll} \right)^2 \frac{\tau_c}{d_p^4} \right) \tag{3.41}$$

$$F_3 = \lambda_{3.2} \left(\sigma_p^{coll} \right)^2 \frac{\tau_c}{n_p d_p^2} E_i E_i \tag{3.42}$$

This system of equation can be solved to find an algebraic model coupling the velocity-charge covariance and the charge variance

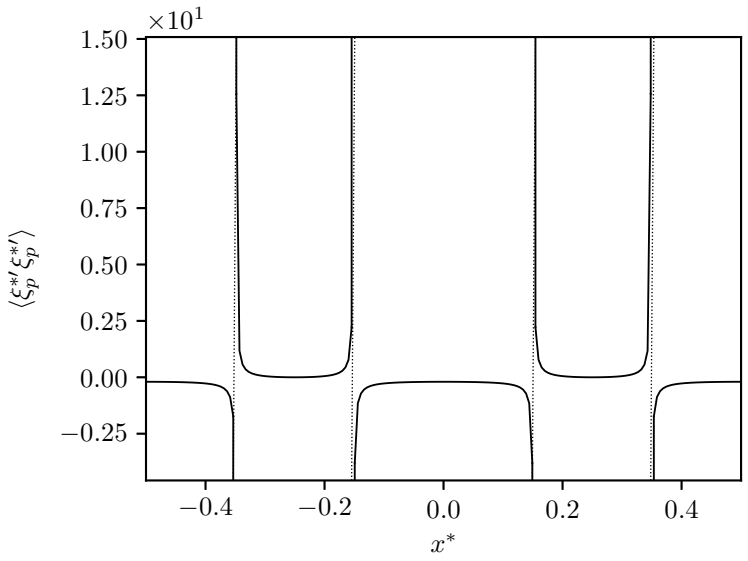

Figure 3.7: Example of a non-physical variance prediction obtained with the coupled algebraic model.

$$\langle c'_{p,i}\xi'_p\rangle = \frac{D_{3,i}}{D_1} - \frac{D_{2,i}}{D_1}\langle \xi'_p\xi'_p\rangle \tag{3.43}$$

$$\langle \xi'_p\xi'_p\rangle = \frac{F_3D_1 - F_{1,i}D_{3,i}}{D_1F_2 - D_{2,j}F_{1,j}} \tag{3.44}$$

Equations 3.43 and 3.44 give us a set of algebraic expression that can be used to close the mean particle electric charge transport equation. With these expressions, we no longer have to solve a system of multiple PDEs. We would also like to remark that this model reduces to the aforementioned simpler algebraic model if $\langle \xi'_p\xi'_p\rangle = 0$. So this model is indeed a more general algebraic model including the effects of the charge variance.

Before testing this model in our test configuration, we would like to note that this algebraic closure law could produce nonphysical results. In particular, the positive sign in equation 3.44 cannot be guaranteed. In addition to this, the denominator of this equation could also approach to zero, leading to indeterminate variance values in some regions. An example of this is shown in figure 3.7. This figure correspond to the initial prediction of the charge variance given by equation 3.44 with the following dimensionless parameters: $Pe = 10^5$, $\tau^*_\sigma = \infty$, $\tau^*_c = 10^{-4}$, ${}^{u_e}/_{u_k} = 300$, $\tau^*_p = \infty$, $e_c = 1$ and ${}^{L}/_{d_p} = 192$. As we can observe, the model leads to some regions with negative variance, and some indeterminate points. This shows that, although it is mathematically possible to derive an algebraic model adding the variance effects, the resulting expressions can lead to meaningless results.

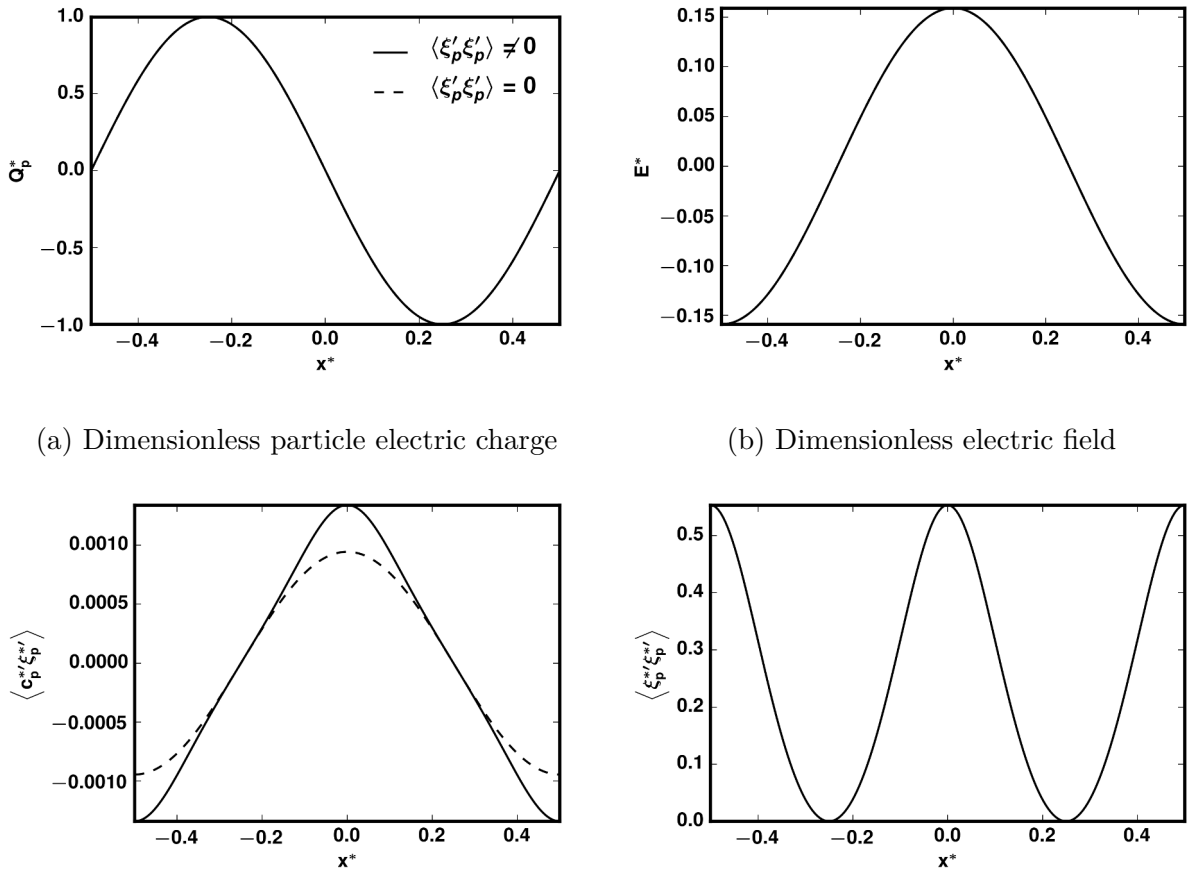

(a) Dimensionless particle electric charge

(b) Dimensionless electric field

(c) Dimensionless particle velocity-charge covariance

(d) Dimensionless particle electric charge variance

Figure 3.8: Comparison of the initial states given by the coupled algebraic model and the algebraic model neglecting the charge variance.

In our tests, we remarked that this problem is more prone to occur when the electric-kinetic energy ratio is high. For example, an acceptable initial condition can be obtained if we decrease this ratio to $u_e/u_k = 30$. Figure 3.8 compares the initial prediction of this more general algebraic model against the initial prediction of the algebraic model neglecting the variance. First of all, we remark that the regions with high variance also correspond to the regions with high covariance and high mean charge gradients. These results are similar to the dynamics observed when solving the complete model. Also, we observe that the initial covariance profile is also modified. Similar to the results obtained with the full model, the covariance profile is stretched in the regions with high electric field and high variance. This shows that this coupled algebraic model does capture the same general dynamics observed in the solution of the complete model.

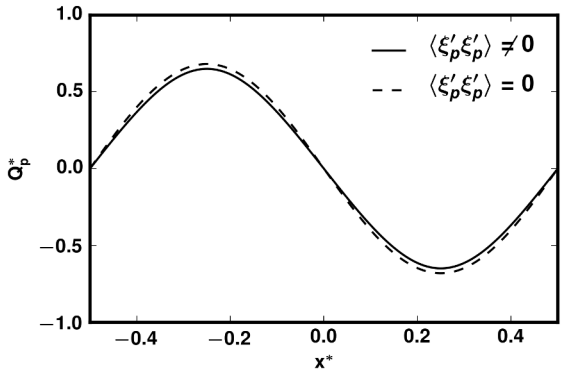

(a) Dimensionless particle electric charge

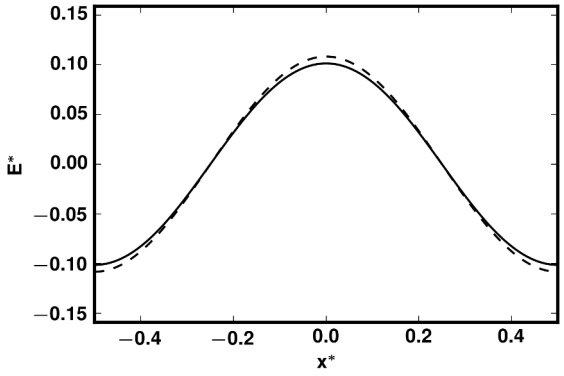

(b) Dimensionless electric field

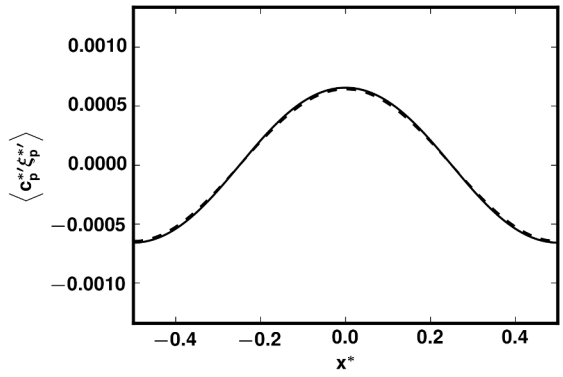

(c) Dimensionless particle velocity-charge covariance

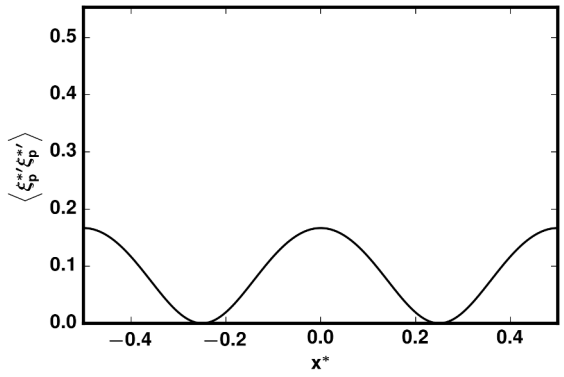

(d) Dimensionless particle electric charge variance

Figure 3.9: Comparison between the coupled algebraic model and the algebraic model neglecting the charge variance term.

We can also study the evolution of the system using this coupled algebraic model. Figure 3.9 shows the state of the system at $t^* = 60$, we can see that this model also seeks the equilibrium state for all the variables. Although difficult to observe, there is a small difference in the mean electric charge profile. As observed when solving the three transport equations, the higher absolute values in the charge-velocity covariance increase the kinetic dispersion of the mean electric charge. Unfortunately, we could not find a configuration where this difference was more visible. We noted that, even with a high order solver, we cannot keep a stable solution for high potential electric energy density configurations.

This results show that, although simpler and mathematically possible, this coupled algebraic model presents two important drawbacks. First, in some configurations, the model can predict negative or infinite variance values. Second, even if the model predicts a reasonable

profile for the electric charge variance, the numerical solution can be highly unstable, especially when the potential electric energy is high. In conclusion, this model generalizes the algebraic model proposed by Montilla et al. (2020), but, it fails to produce useful results in configuration where the effects of the electric charge variance are dominant, which was the main objective of this model.

3.8 Semi-Algebraic model

The previous section presented an attempt to simplify the full coupled transport equations model to a simpler model with only one transport equation for the mean charge and an algebraic expression for the two remaining variables. However, we observed that such approach is very limited. Another possible simplification approach could be to derive the algebraic expression for one of the variables while keeping the full transport equation for the others. In this case, we propose to use an algebraic expression for the charge-velocity covariance (equation 3.43) and solve the full transport equation for the charge variance (equation 3.11). The reason behind this choice is that the covariance term is a vector quantity that could add up to three PDEs to the system. Therefore, by simplifying the covariance, we are also minimizing the number of equations that need to be solved.

We tested this approach using the same parameters for which the algebraic model fails to provide a physical prediction, as shown in figure 3.7. The solution obtained using this semi-algebraic model is shown in figure 3.10. In this figure we compare the results of this model with the solution obtained solving the full model. As we can see, the solution produced by the semi-algebraic model is not only perfectly physical, but it is identical to the solution of the full model for all the 4 profiles. According to these results, the semi-algebraic model proposed in this section can be considered as an effective closure law for the charge-velocity covariance term.

3.9 Conclusions

In this chapter, we have extended the Eulerian modeling of the mean electric charge transport equation. The simple algebraic gradient model for the electric charge flux term was replaced with a more complete model using the full charge-velocity covariance transport equation. The charge variance term, which was neglected in the algebraic model, was closed using also the transport equation obtained with the kinetic theory of rapid granular flow. We have also proposed closure laws for two of the third order moments appearing in the covariance and variance transport equations.

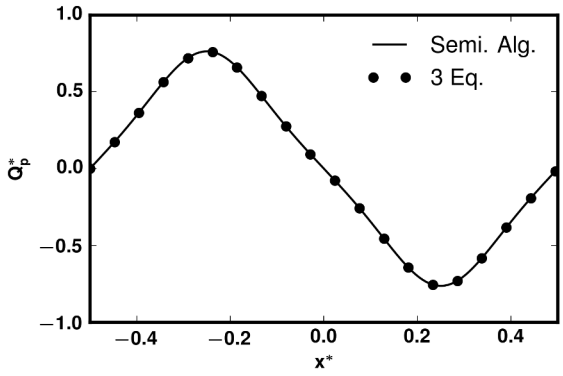

(a) Dimensionless particle electric charge

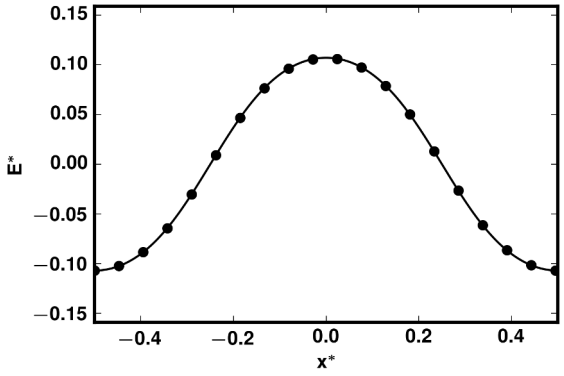

(b) Dimensionless electric field

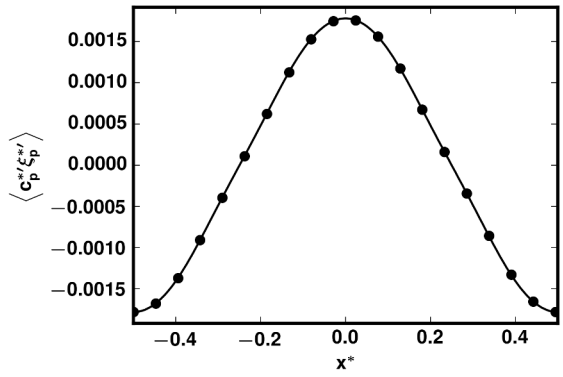

(c) Dimensionless particle velocity-charge covariance

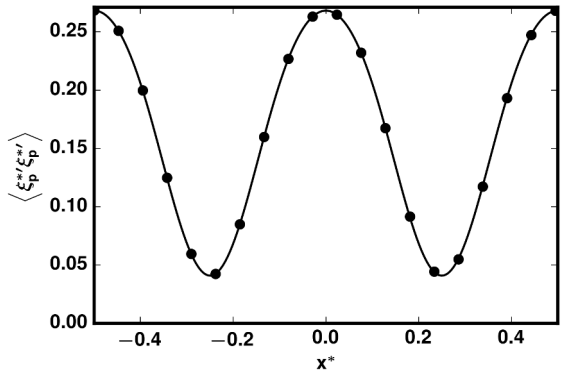

(d) Dimensionless particle electric charge variance

Figure 3.10: Comparison between the full 3 transport equations model and the semi-algebraic model).

This more accurate modeling approach revealed the limitations of the algebraic model. Firstly, even if the variance term is neglected, the algebraic model could fail to capture the correct covariance dynamics if characteristic time of the covariance transport equation is large enough to invalid the quasi-equilibrium hypothesis assumed in the algebraic model. Secondly, the three transport equations model showed that the charge variance term cannot be neglected when the electric potential energy of the system is high. This charge variance term induces an extra charge flux due to the charge transport generated by the electrostatic force. Therefore, neglecting the charge variance could lead to an underestimation of the charge flux in the regions with high electric field.

Because we are aware that adding and solving these additional transport equations can be very costly, we also proposed and tested some possible simplifications. Our first attempt was to derived a coupled algebraic model that takes into account the electric charge variance. Although, mathematically feasible, the final result proved to be nonphysical under some conditions, especially when the electric potential energy is high. This means that this coupled algebraic model cannot be used when the variance term is dominant. Which goes against the main objective of the model. Due to this important shortcoming, we propose a different alternative in which the charge-velocity covariance retains the algebraic form including the variance term. But the charge variance is obtained solving its transport equation. This intermediary model showed excellent agreement compared with the full model. This approach also solved the non-physicality problem we encountered in the coupled algebraic model.

Appendix

3.A Algebraic gradient closure model for the third order moment $\langle \xi'_p c'_{p,i} c'_{p,j} \rangle$

The transport equation of the particle velocity-charge covariance $\langle \xi'_p c'_{p,i} \rangle$ depends on a higher order statistical moment $\langle \xi'_p c'_{p,i} c'_{p,j} \rangle$. In order to close the 3rd order statistical moment, we can use the same strategy employed to approximate the 2nd order statistical moments: an algebraic model. For this, we write the transport equation for this 3rd order moment using the general mean transport equation with $\phi = \xi'_p c'_{p,i} c'_{p,j}$:

$$
\begin{aligned}
& n_p \frac{D\left\langle \xi'_p c'_{p,i} c'_{p,j} \right\rangle}{Dt} + n_p S_{p,ijk} \frac{\partial Q_p}{\partial x_k} + n_p \left\langle \xi'_p c'_{p,k} \right\rangle \frac{\partial R_{p,ij}}{\partial x_k} + n_p R_{p,ik} \frac{\partial \left\langle \xi'_p c'_{p,j} \right\rangle}{\partial x_k} \\
& + n_p R_{p,jk} \frac{\partial \left\langle \xi'_p c'_{p,i} \right\rangle}{\partial x_k} + n_p \frac{2}{\tau_p} \left\langle \xi'_p c'_{p,i} c'_{p,j} \right\rangle - \frac{n_p}{m_p} \left\langle \xi'_p c'_{p,j} \xi'_p \right\rangle E_i \\
& - \frac{n_p}{m_p} \left\langle \xi'_p c'_{p,i} \xi'_p \right\rangle E_j + n_p \left\langle c'_{p,m} c'_{p,j} \xi'_p \right\rangle \frac{\partial U_{p,i}}{\partial x_m} + n_p \left\langle c'_{p,m} c'_{p,i} \xi'_p \right\rangle \frac{\partial U_{p,j}}{\partial x_m} \\
& = \mathcal{C}\left(\xi_p c'_{p,i} c'_{p,j} \right) - Q_p U_{p,i} \mathcal{C}\left(c_{p,j} \right) - Q_p U_{p,j} \mathcal{C}\left(c_{p,i} \right) - \left\langle \xi'_p c'_{p,i} \right\rangle \mathcal{C}\left(c_{p,j} \right) \\
& - \left\langle \xi'_p c'_{p,j} \right\rangle \mathcal{C}\left(c_{p,i} \right) - R_{p,ij} \mathcal{C}\left(\xi_p \right),
\end{aligned}
\tag{3.45}
$$

with $S_{p,ijk} = \langle c'_{p,i} c'_{p,j} c'_{p,k} \rangle$

Here the equations of $\langle \xi_p \rangle$, $\langle c_{p,i} \rangle$ $\langle \xi'_p c'_{p,i} \rangle$, and $\langle c'_{p,i} c'_{p,j} \rangle$ have been used to further simplify the final expression. We have also treated the force term in the same way as we did in the covariance equation: the undisturbed flow properties and the macroscopic electric field are assumed to be uncorrelated to the particles fluctuant electric charge.

In order to derive an algebraic model, we need to close the collision terms, in particular the term involving the 3rd order moment. To be able to derive an algebraic model we need a more general model to take into account the particle velocity-charge correlation in the collision integrals. We, therefore, propose an extension of the collision model proposed by Montilla et al. (2020). In this work, we suppose that the conditional mean $\langle \xi_{p_1} \mid \mathbf{c_{p_1}} \rangle$ can be written as:

$$
\langle \xi_p \mid \mathbf{c_{p_1}} \rangle = A + B_i c'_{p,i} + C_{ij} c'_{p,i} c'_{p,j} \tag{3.46}
$$

The tensors A, B_i and C_{ij} are calculated so the first three statistical moments are satisfied:

$$\int_{\mathbb{R}^3} \langle \xi_p \mid \mathbf{c_{p_1}} \rangle f d\mathbf{c_p} = n_p \langle \xi_p \rangle \tag{3.47}$$

$$\int_{\mathbb{R}^3} c'_{p,i} \langle \xi_p \mid \mathbf{c_{p_1}} \rangle f d\mathbf{c_p} = n_p \langle c'_p \xi_p \rangle \tag{3.48}$$

$$\int_{\mathbb{R}^3} c'_{p,i} c'_{p,j} \langle \xi_p \mid \mathbf{c_{p_1}} \rangle f d\mathbf{c_p} = n_p \langle c'_{p,i} c'_{p,j} \xi_p \rangle \tag{3.49}$$

If we assume that the particle velocity probability density function follows a Gaussian distribution, the 4th order tensor $\langle c'_{p,i} c'_{p,j} c'_{p,k} c'_{p,l} \rangle$ can be written as:

$$\langle c'_{p,i} c'_{p,j} c'_{p,k} c'_{p,l} \rangle = R_{p,ij} R_{p,kl} + R_{p,ik} R_{p,jl} + R_{p,il} R_{p,jk}, \tag{3.50}$$

Assuming an isotropic kinetic stress tensor, we obtain:

$$\langle c'_{p,i} c'_{p,j} c'_{p,k} c'_{p,l} \rangle = \Theta_p^2 \left(\delta_{ij} \delta_{kl} + \delta_{ik} \delta_{jl} + \delta_{il} \delta_{jk} \right), \tag{3.51}$$

This allows us to deduce the expressions for the tensors A, B_i and C_{ij}

$$A = \langle \xi_p \rangle - \frac{1}{2\Theta_p} \langle \xi_p c'_{p,i} c'_{p,j} \rangle \tag{3.52}$$

$$B_i = \frac{1}{\Theta_p} \langle c'_{p,i} \xi_p \rangle \tag{3.53}$$

$$C_{ij} = \frac{1}{\Theta_p^2} \langle c'_{p,i} c'_{p,j} \xi_p \rangle \tag{3.54}$$

This non-linear model reduces exactly to the already published linear model if we assume $\langle \xi_p c'_{p,i} c'_{p,j} \rangle = 0$

With this model, we can now compute the RHS of equation 3.45. For this term, we will assume a isotropic kinetic stress tensor . We also neglect any velocity and granular temperature gradient, as well as any cross product term between Q_p, E_i, $\langle c'_{p,i}\xi'_p\rangle$, $\langle\xi'_p\rangle$, $\langle\xi'_p\xi'_p c_{p,i}\rangle$:

$$\begin{aligned}
RHS = &-\frac{n_p}{\tau_c}\left[\lambda_{2.4}\left(1+e_c\right)-\lambda_{2.5}\left(1+e_c\right)^2\right]\left\langle\xi'_p c'_{p,i}c'_{p,j}\right\rangle \\
&+\frac{n_p}{\tau_c}\left[-\lambda_{2.7}\left(1+e_c\right)+\lambda_{2.8}\left(1+e_c\right)^2\right]\left\langle\xi'_p c'_{p,m}c'_{p,m}\right\rangle\delta_{ij} \\
&-\lambda_{2.6}\frac{n_p}{\tau_\xi}\left\langle\xi'_p c'_{p,i}c'_{p,j}\right\rangle \\
&-n_p d_p\Theta_p^{1/2}\left(1+e_c\right)\frac{1}{\tau_\xi}\left[\lambda_{2.9}\frac{\partial\left\langle\xi'_p c'_{p,i}\right\rangle}{\partial x_j}+\lambda_{2.9}\frac{\partial\left\langle\xi'_p c'_{p,j}\right\rangle}{\partial x_i}+\lambda_{2.10}\frac{\partial\left\langle\xi'_p c'_{p,n}\right\rangle}{\partial x_n}\delta_{ij}\right] \\
&-\lambda_{2.11}n_p d_p\Theta_p^{1/2}\left(1+e_c\right)^2\frac{1}{\tau_\xi}\left[\frac{\partial\left\langle\xi'_p c'_{p,n}\right\rangle}{\partial x_n}\delta_{ij}+\frac{\partial\left\langle\xi'_p c'_{p,i}\right\rangle}{\partial x_j}+\frac{\partial\left\langle\xi'_p c'_{p,j}\right\rangle}{\partial x_i}\right]
\end{aligned} \tag{3.55}$$

with $\lambda_{2.4}\approx 6.667$, $\lambda_{2.5}\approx 1.387$, $\lambda_{2.6}\approx 3.201$, $\lambda_{2.7}\approx 0.2667$, $\lambda_{2.8}\approx 0.2607$, $\lambda_{2.9}\approx 10.68$, $\lambda_{2.10}\approx 208.2$, and $\lambda_{2.11}\approx 0.2048$

Equations 3.45 and 3.55 give the form of a simple governing equation for the 3rd order moment $\langle\xi'_p c'_{p,i}c'_{p,j}\rangle$. To extract an algebraic closure model, we simplify the left hand side of equation 3.45 by neglecting the contribution of the Lagrangian time derivative, the velocity and kinetic stress gradient, and the third order tensors $S_{p,ijk}$ and $\langle\xi'_p\xi'_p c'_{p,i}\rangle$. With these assumptions, we can write equation 3.45 as:

$$K_1\langle\xi'_p c'_{p,i}c'_{p,j}\rangle + K_2\langle\xi'_p c'_{p,m}c'_{p,m}\rangle\delta_{ij} = D_{ij}, \tag{3.56}$$

with

$$K_1 = n_p \left[\frac{1}{\tau_c} \left(\lambda_{2.4} \left(1 + e_c\right) - \lambda_{2.5} \left(1 + e_c\right)^2 \right) + \frac{1}{\tau_p} + \lambda_{2.6} \frac{1}{\tau_\xi} \right], \tag{3.57}$$

$$K_2 = -\frac{n_p}{\tau_c} \left[-\lambda_{2.7} \left(1 + e_c\right) + \lambda_{2.8} \left(1 + e_c\right)^2 \right], \tag{3.58}$$

$$\begin{aligned} D_{ij} = & -n_p R_{p,jk} \frac{\partial \langle \xi_p c'_{p,i} \rangle}{\partial x_k} - n_p R_{p,ik} \frac{\partial \langle \xi_p c'_{p,j} \rangle}{\partial x_k} \\ & - n_p d_p \Theta_p^{1/2} \left(1 + e_c\right) \frac{1}{\tau_\xi} \left[\lambda_{2.9} \frac{\partial \left\langle \xi'_p c'_{p,i} \right\rangle}{\partial x_j} + \lambda_{2.9} \frac{\partial \left\langle \xi'_p c'_{p,j} \right\rangle}{\partial x_i} + \lambda_{2.10} \frac{\partial \left\langle \xi'_p c'_{p,n} \right\rangle}{\partial x_n} \delta_{ij} \right] \\ & - \lambda_{2.11} n_p d_p \Theta_p^{1/2} \left(1 + e_c\right)^2 \frac{1}{\tau_\xi} \left[\frac{\partial \left\langle \xi'_p c'_{p,n} \right\rangle}{\partial x_n} \delta_{ij} + \frac{\partial \left\langle \xi'_p c'_{p,i} \right\rangle}{\partial x_j} + \frac{\partial \left\langle \xi'_p c'_{p,j} \right\rangle}{\partial x_i} \right]. \end{aligned} \tag{3.59}$$

In a 3D flow, equation 3.56 can be solved for the third order moment:

$$\langle \xi'_p c'_{p,i} c'_{p,j} \rangle = \frac{1}{K_1} D_{ij} - \frac{K_2}{K_1 \left(K_1 + 3K_2\right)} D_{mm} \delta_{ij} \tag{3.60}$$

3.B Algebraic gradient closure model for the third order moment $\langle \xi'_p \xi'_p c'_{p,i} \rangle$

Similarly to the particle velocity-charge covariance equation, the particle charge variance equation is function of a higher statistical moment $\langle \xi'_p \xi'_p c'_{p,i} \rangle$. To close this term, we follow the same methodology used to close the previous third order moment. First, we write the full transport equation for this third order moment using the general mean transport equation with $\phi = \xi'_p \xi'_p c'_{p,i}$:

$$\begin{aligned} & n_p \frac{D \left\langle \xi'_p \xi'_p c'_{p,i} \right\rangle}{Dt} + 2 n_p \left\langle \xi'_p c'_{p,i} c'_{p,j} \right\rangle \frac{\partial Q_p}{\partial x_j} + n_p \left\langle c'_{p,i} c'_{p,j} \right\rangle \frac{\partial \left\langle \xi'_p \xi'_p \right\rangle}{\partial x_j} \\ & + 2 n_p \left\langle \xi'_p c'_{p,j} \right\rangle \frac{\partial \left\langle \xi'_p c'_{p,i} \right\rangle}{\partial x_j} + \frac{n_p}{\tau_p} \left\langle \xi'_p \xi'_p c'_{p,i} \right\rangle - \frac{n_p}{m_p} \left\langle \xi'_p \xi'_p \xi'_p \right\rangle E_i \\ & + n_p \left\langle \xi'_p \xi'_p c'_{p,j} \right\rangle \frac{\partial U_{p,i}}{\partial x_j} = \mathcal{C} \left(\xi'_p \xi'_p c'_{p,i} \right) - 2 \left\langle \xi'_p c'_{p,i} \right\rangle \mathcal{C} \left(\xi'_p \right) - \left\langle \xi'_p \xi'_p \right\rangle \mathcal{C} \left(c'_{p,i} \right). \end{aligned} \tag{3.61}$$

Here, the force term was treated using the same methodology as before.

Assuming isotropic kinetic stress tensor and neglecting the particle mean velocity gradient and the granular temperature gradient, we obtain a simplified form for the right hand side of equation 3.61

$$\begin{aligned}&\mathcal{C}\left(\xi_p'\xi_p'c_{p,i}'\right)-2\left\langle\xi_p'c_{p,i}'\right\rangle\mathcal{C}\left(\xi_p'\right)-\left\langle\xi_p'\xi_p'\right\rangle\mathcal{C}\left(c_{p,i}'\right)\\&\quad=-\left[\frac{1}{3}\left(1+e_c\right)\frac{1}{\tau_c}+\left(2.806-1.017\gamma\Theta_p^{2/5}\right)\frac{1}{\tau_\xi}\right]n_p\left\langle\xi_p'\xi_p'c_{p,i}'\right\rangle\end{aligned}\tag{3.62}$$

Similarly to the previous algebraic gradient model, we simplify the left hand side of equation 3.61 by neglecting the contribution of the Lagrangian time derivative, the velocity and kinetic stress gradient, and the third order tensors $S_{p,ijk}$ and $\langle\xi_p'c_{p,i}'c_{p,j}'\rangle$. We will also drop any nonlinear term involving $\langle\xi_p'c_{p,i}\rangle$, E_i or Q_p. These assumptions lead us to the following closure model for the third order moment:

$$n_p\langle\xi_p'\xi_p'c_{p,i}'\rangle=-\frac{n_pR_{p,ij}}{\frac{1}{3}\left(1+e_c\right)\frac{1}{\tau_c}+\frac{1}{\tau_p}+\left(\lambda_{3.4}-\lambda_{3.5}\gamma\Theta_p^{2/5}\right)\frac{1}{\tau_\xi}}\frac{\partial\langle\xi_p'\xi_p'\rangle}{\partial x_j}\tag{3.63}$$

with $\lambda_{3.4}\approx 2.806$ and $\lambda_{3.5}\approx 1.017$

Chapter 3 Bibliography

E. Fehlberg. Classical fifth-, sixth-, seventh-, and eight-order Runge-Kutta Formulas with stepsize control. Technical report, 1968.

J. Kolehmainen, A. Ozel, and S. Sundaresan. Eulerian modelling of gas-solid flows with triboelectric charging. *Journal of Fluid Mechanics*, 848(June):340–369, 2018.

C. Montilla, R. Ansart, and O. Simonin. Modelling of the mean electric charge transport equation in a mono-dispersed gas-particle flow. *Journal of Fluid Mechanics*, 902:(A12)1–26, 2020.

M. Ray, F. Chowdhury, A. Sowinski, P. Mehrani, and A. Passalacqua. An Euler-Euler model for mono-dispersed gas-particle flows incorporating electrostatic charging due to particle-wall and particle-particle collisions. *Chemical Engineering Science*, 197:327–344, 2019.

M. Sakiz and S. Olivier. Numerical experiments and modelling of non-equilibrium effects in dilute granular flows. In *21st Int. Symp. on Rarefied Gas Dynamics*, pages 287–294, 1999.

O. Simonin, E. Deutsch, and M. Boivin. Large Eddy Simulation and Second-Moment Closure Model of Particle Fluctuating Motion in Two-Phase Turbulent Shear Flows. In *Turbulent Shear Flows 9*, pages 85–115. Springer, 1995.

Q. Wang, K. D. Squires, and O. Simonin. Large eddy simulation of turbulent gas-solid flows in a vertical channel and evaluation of second-order models. *International Journal of Heat and Fluid Flow*, 19(5):505–511, 1998.

Chapter 4

ECVT Image reconstruction algorithms for fluidized beds

As we have stated in the introductory chapter, there have been more than 70 years worth of experimental research on the electrostatic effects on fluidized bed dynamics. This research can be divided into two types: characterization of the electrodynamics of the solid phase, and characterization of the hydrodynamics of the bed. The former is usually done using Faraday's cups and electrostatic probes to measure the electrical properties of the bed. While the latter have relied mainly on probes and pressure tabs to estimate the hydrodynamic behavior of the system. However, these techniques only provide local intrusive measurements that could affect the dynamics of the bed. Especially given that the charging dynamics is heavily influenced by solid-solid contacts. To overcome these shortcomings, tomographic devices can be employed as an alternative to obtain an approximate 2D or 3D representation of the solid volume fraction distribution inside the bed, without introducing any foreign material. In this chapter, we explore the use of the Electrical Capacitance Volume Tomography as a way to examine the dynamics inside the reactor.

4.1 Experimental setup

The main objective of our experimental research is to obtain the most accurate spatial representation possible of the solid volume fraction distribution inside a fluidized bed reactor. To accomplish this, we acquired a state-of-the-art ECVT device from the American company Tech4Imaging. The system consists of a cylindrical tomograph wit 36 square electrodes organized in 4 concentric rows with 9 electrodes per row. The sensing region is a cylinder of 11 cm diameter and 10 cm height. The measuring frequency can be adjusted between 10 and 100 Hz. The 36 electrodes are connected to a Data Acquisition System (DAS) using 36 coaxial cables. The DAS is attached to a computer via an USB cable. Using a proprietary software, we can start and stop the data acquisition process. The program also provides simple tools to visualize and explore the reconstructed solid volume fraction distribution. We can also export either the raw measurements or the reconstructed image for further analysis. The final reconstructed 3D image is composed of 8000 cubic voxels of 5 mm. At the time of purchase, this system was superior to any of the ECVT devices used in published literature that had between 12 and 24 sensors. A detailed explanation of how the ECVT technology works is provided in the next section.

The design of the experimental fluidized bed was largely influenced by the previous Ph.D. thesis done by Nasro Allah (2019) in our same research group. His project aimed primarily at characterizing the charging dynamics of different types of powders inside a fludizied bed under different conditions. To accomplish this, he built a laboratory scale fluidized bed using a PMMA column of 1 m height and 10 cm internal diameter. The system counted with 2 Faraday's cups, one installed below the windbox allowing him to measure the net charge of the particles in the bed (inspired from Sowinski et al. (2009)). And another Faraday's cup to measure the net charge of the entrained fine particles. He also installed pressure sensors along the column to monitor the pressure fluctuation along the column. It is the presence of these pressure sensors that does not allow us to correctly fit the ECVT device around the fluidized bed.

For this reason, we built an identical fluidized bed using a 1 m height and 10 cm diameter PMMA column. However, we did not install any pressure sensor, nor any Faraday's cup. Similarly to Nasro-Allah's setup, the inlet gas is evenly distributed to the column using a porous plate of 3 mm width. To ensure a good fluidization quality, the porosity quality was chosen so the pressure drop through the distributor is at least equal to 30% of the pressure drop through the bed. Figure 4.1 shows the fluidized bed column with the ECVT system installed.

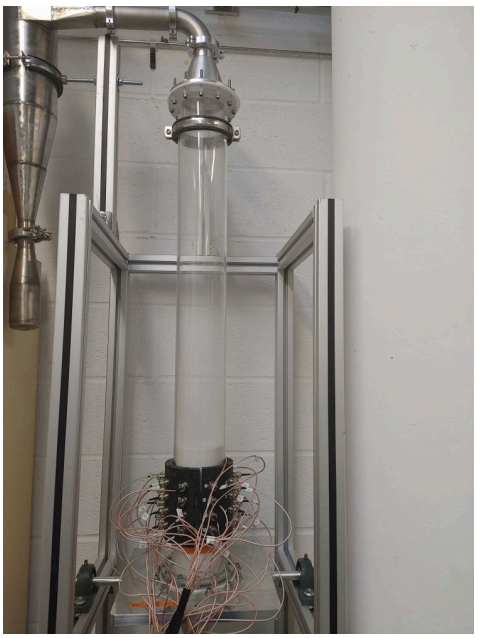

Figure 4.1: Laboratory scale fluidized bed column used with the acquired ECVT device.

Previous experimental studies have shown that the gas humidity plays a major role in the build up of electrostatic charges inside the bed. Therefore, a humidification control system was placed before the distributor. This system is composed of two pairs of wet and dry air lines. One pair can supply the fluidized bed with high volume flow rates as it is equipped

with a flow meter that can go up to 25 Nm^3/h. While the other pair is limited to 2 Nm^3/h and it is used to feed the bed with low volume flow rates. Both flow meters have a precision of 0.2% if the flow rate is above 20% the maximum value. If it goes below this threshold, the precision drops to 1%.

The system schematics is shown in figure 4.2. The inlet gas comes from the laboratory compressed air line. This line delivers dry air at ambient temperature and at a pressure equal to 5 bar. This air is then divided into the wet lines and the dry lines. The wet lines are injected into a distilled water tank. After this, the wet air is mixed with the dry air, and the output is fed to the fluidized bed. The computer installed in the humidification system is connected to the flow meters and a humidity sensor. Using a PID controller, the computer can regulate the flow rate passing through each one of the 4 lines to obtain the desired volume flow rate and humidity. All this is adjusted and monitored through a graphical user interface.

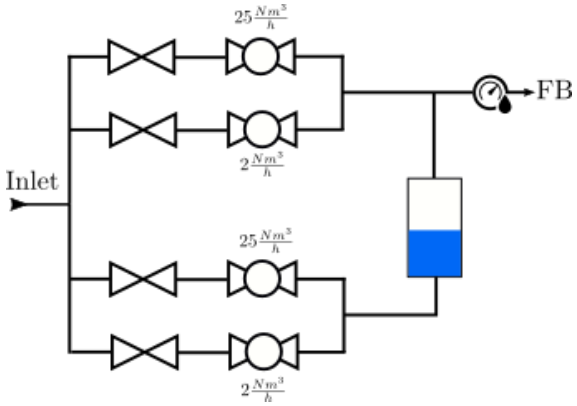

(a) Scheme of the humidification system used.

(b) Photograph of the humidification system used.

Figure 4.2: Humidification system used.

4.2 Electrical Tomography Volume Capacitance

The Electrical Capacitance Volume Tomography (ECVT) is a non-invasive measurement technique that allows us to reconstruct an approximated three-dimensional representation of the volume fraction of phases in a two phase flow. The ECVT was developed by Marashdeh (2006) as an improvement over Electrical Capacitance Tomography (ECT) that could only reconstruct a two-dimensional image.

This measurement device is composed of a series of electrodes that are located around a sensing region. These sensors are then connected to the data acquisition system (DAS) that samples and processes the signals coming from the plates. Finally, the DAS is connected to a computer where, using a special reconstruction software, the capacitance measurements are transformed into a full 3D representation of the volume fraction of the phases inside the volume of interest. Figure 4.3 shows the scheme of how this system works.

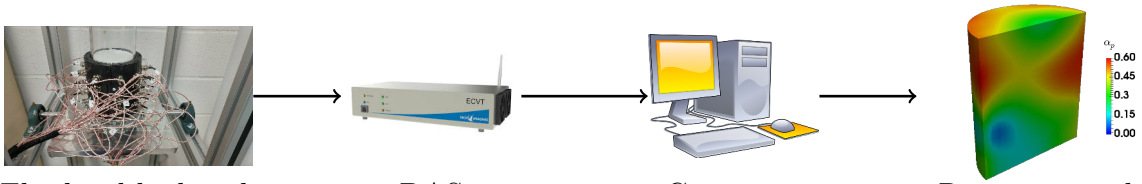

Figure 4.3: Electrical capacitance volume tomography system.

The main advantages of this device is that it is easy to build and it can be made to fit complex non regular shapes (Taruno et al., 2013; Wang et al., 2012). In addition to this, the whole ECVT equipment (tomograph + data acquisition system) is a relative small and it can be easily transported to different locations. This device also does not rely on high electric field nor any radioactive technology, which makes this system very safe and easy to install without requiring any special security measures. Finally, this device is capable of delivering a high enough acquisition frequency to accurately capture most of the temporal dynamics in a two phase flow.

As one might expect, the ECVT technology fits perfectly to study the dynamics of a fluidized bed reactor in a non-intrusive way. One of the first study was performed by Du et al. (2007), they compared the volume fraction inside a fluidized bed with the data obtained from an optical fiber probe located inside the bed. They concluded that the ECVT system was as accurate as the probe, not only for the volume fraction, but for the bubble size as well. We can also find the work of Weber and Mei (2013) and Weber et al. (2013). They used a system of 24 sensors to study the bubble size and frequency in a laboratory scale fluidized bed. The ECVT system allowed them to study the growth and breakup of bubbles inside a fluidized bed. They also compared their data to numerical simulation, showing that the inlet boundary condition can have a big impact on the quality of the simulations.

4.2.1 Physical principle and the sensitivity matrix approach

The ECVT/ECT technology is based on the idea that the capacitance between two electrodes is a function of the internal composition of the medium between the plates. In particular, capacitance between a pair of electrode is given by:

$$C_i = \frac{1}{V_i} \oiint_A \varepsilon\left(x, y, z\right) \nabla\phi\left(x, y, z\right) dA. \tag{4.1}$$

Where C_i is the capacitance between the electrode pair i, A is the area enclosing one of the electrodes, V_i is the potential difference between the electrodes, ϕ is the electric potential and ε is the medium permittivity distribution.

Given a tomograph with x electrodes, we can measure $M = {}^{x(x-1)}/_{2}$ inter-plate capacitance values. To find the spatial permittivity distribution, we would need to solve the system of M integral equations given by 4.1. However, this approach is extremely difficult to implement. A more common methodology is based on the sensitivity matrix model. We know that the capacitance between two plates is a function of the permittivity distribution, $\vec{C} = f\left(\varepsilon\left(x, y, z\right)\right)$. Therefore, by doing a Taylor expansion around some reference state, we obtain:

$$\vec{C} - \vec{C}_{\text{ref}} = \left(\varepsilon - \varepsilon_{\text{ref}}\right) \left.\frac{df}{d\varepsilon}\right|_{\varepsilon_{\text{ref}}} + \mathcal{O}\left[\left(\varepsilon - \varepsilon_{\text{ref}}\right)^2\right]. \tag{4.2}$$

Here, ε_{ref} and C_{ref} are a reference permittivity distribution and its corresponding reference inter-plate capacitances.

Neglecting the higher order terms, we can write:

$$\Delta\vec{C} \approx \Delta\varepsilon \left.\frac{df}{d\varepsilon}\right|_{\varepsilon_{\text{ref}}}. \tag{4.3}$$

Assuming that the changes in the medium permittivity are proportional to the volume fraction α, and taking the reference state as the empty state $\alpha = 0$:

$$\Delta\vec{C} \approx s\alpha. \tag{4.4}$$

If we divide the sensing region into N voxels, we can relate the M inter-plate capacitance values to the N volume fraction values in each voxel using the following matrix equation:

$$\Delta\vec{C} \approx S\vec{\alpha}. \tag{4.5}$$

S is known as the sensitivity matrix and it measures the changes in the capacitance value on the electrode pair i given an unitary change on the volume fraction in voxel j. We notice that the dimensions of the matrix S are automatically given by the number of measurements M and the number of voxels in the target image N, more specifically $S \in \mathbb{R}^{M \times N}$. This sensitivity matrix is known for a given tomograph, and it is usually calculated solving equations 4.1.

Therefore, if we have a set of M inter-plate measurements, the volume fraction distribution should satisfy equation 4.5. However, given that usually $M \neq N$, equation 4.5 cannot be explicitly solved by multiplying by S^{-1}, because non-square matrices do not have an inverse. This constitutes one of the main drawbacks of the ECVT technology: the image reconstruction problem is ill-posed.

4.2.2 Image reconstruction algorithms for ECVT devices

Over the years, many studies have proposed different approaches to try to find an approximated solution to the image reconstruction problem in ECT/ECVT systems (equation 4.5). However, due to the ill-posedness nature of the problem, none of these algorithms can guarantee a 100% accurate reconstruction process. In other words, only an approximate volume fraction distribution can be obtained. In the following section, we will describe some of the available options found the literature.

Linear BackProjection Algorithm (LBP)

The Linear BackProjection algorithm (LBP) is the simplest approach available (Xie et al., 1989). The LBP algorithm assumes that the solid volume fraction in one voxel can be explained as a linear combination of the sensitivity coefficients weighted by the capacitance measurements. This can be expressed as:

$$\vec{\alpha} \approx S^T \Delta \vec{C}. \tag{4.6}$$

This method is easy to implement and it can be even hard-coded into hardware to produce very fast results in real-time. This was also the algorithm provided by Tech4Imaging for our ECVT system.

In order to test the spatial accuracy of this approach, we designed a series of simple static test cases, where an object of known shape and volume fraction was inserted inside the sensing region. The output of our ECVT system was then compared with the expected

output. To place ourselves in fluidized bed-like configurations, our test cases were composed of a single empty sphere of known diameter placed inside a fixed bed of glass beads ($d_p = 250\,\mu$m). Figure 4.4 shows a vertical slice of the reconstructed and expected images for the two extreme cases: the biggest sphere available ($d_{\text{sphere}} = 55\,$mm) and the smallest sphere available ($d_{\text{sphere}} = 27\,$mm). As we can see, the reconstructed solid volume fraction distribution is not satisfactory at all. The small sphere is not seen, and the big sphere is completely blurred. This kind of images will make very difficult to detect and capture the shape of bubbles inside a fluidized bed. Given this limitation, we chose to study more complex and accurate image reconstruction algorithms.

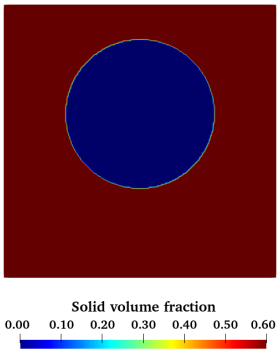

(a) True distribution $d_{\text{sphere}} = 55\,$mm.

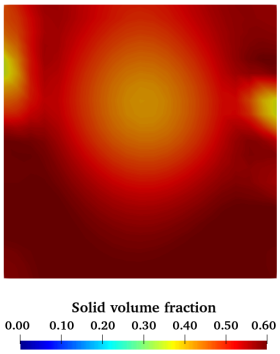

(b) Reconstructed distribution.

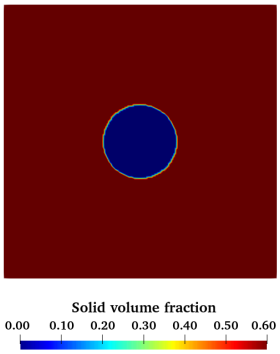

(c) True distribution $d_{\text{sphere}} = 27\,$mm.

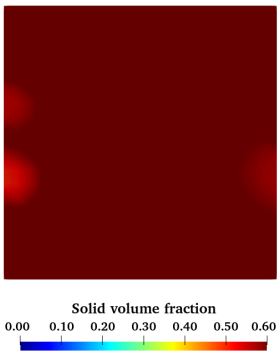

(d) Reconstructed distribution.

Figure 4.4: Static test case of a single void sphere in the middle of a fixed bed of glass beads. Vertical slice comparison between the true solid volume fraction distribution and the reconstructed image using the LBP algorithm.

Iterative Linear BackProjection Algorithm (ILBP)

The ILBP was first proposed by Yang et al. (1999). This algorithm uses a Landweber iteration scheme to improve the solution of the LBP method. This methodology can be seen as finding the closest volume fraction distribution that satisfies equation 4.5:

$$\text{Minimize: } \|\Delta\vec{C} - S\vec{\alpha}\|^2. \tag{4.7}$$

It can be shown that this minimization problem has a simple iterative algorithm where an approximation of the volume fraction for iteration k can be obtained as:

$$\vec{\alpha}_k = \vec{\alpha}_{k-1} + S^T\left(\Delta\vec{C} - S\vec{\alpha}_{k-1}\right). \tag{4.8}$$

Where, $\vec{\alpha}_0$ is chosen to be the solution of the LBP algorithm.

We implemented and tested this approach with the test cases described above. Figure 4.5 shows the reconstructed images obtained with this algorithm. We can see that there is a significant improvement over the LBP. The reconstructed images clearly show 2 void sphere-like objects inside a fixed bed of particles. Likewise, the boundaries between the bed and the objects seem to be well defined.

Given that the objects are now well defined, we can try to calculate the diameter of the reconstructed objects. For this, we need to establish the boundary between the solid particles and the sphere. We chose this boundary to be located at $\alpha_p = 0.3$. With this threshold value, we can compute the 3D surface area of the object A_{object}. Then, the object's diameter is defined as the diameter of the sphere having the same surface area:

$$d_{\text{object}} = \sqrt{\frac{A_{\text{object}}}{\pi}} \tag{4.9}$$

For the big sphere of 55 mm, the reconstructed object had an equivalent diameter of 57 mm. And for the small sphere of 27 mm, the obtained equivalent diameter was of 18 mm. Table 4.1 compares the equivalent diameter of the reconstructed object against the expected diameter for all test cases. This result shows that the ILBP algorithm can reconstruct very well big objects, however the accuracy reduces as the object's size goes down.

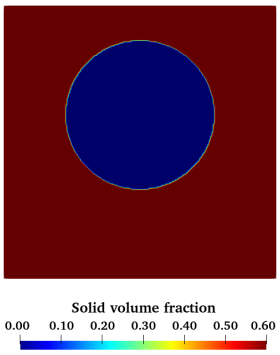

(a) True distribution $d_{\text{sphere}} = 55\,\text{mm}$.

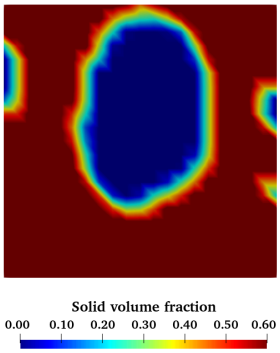

(b) Reconstructed distribution.

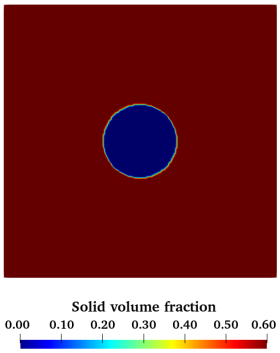

(c) True distribution $d_{\text{sphere}} = 27\,\text{mm}$.

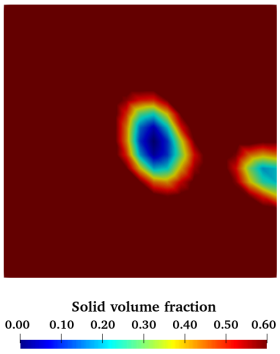

(d) Reconstructed distribution.

Figure 4.5: Static test case of a single void sphere in the middle of a fixed bed of glass beads. Vertical slice comparison between the true solid volume fraction distribution and the reconstructed image using the ILBP algorithm.

Multi-Objective Image Reconstruction Technique (MOIRT)

Given that the ILBP scheme was not 100% satisfactory, we tried a third different and more complex approach. This algorithm is called the Multi-Objective Image Reconstruction Technique (MOIRT) and it was developed by Warsito and Fan (2001). The MOIRT is based on a similar minimization problem as the previous approach. However, the objective function is much more complex as it tries to minimize 3 different aspects:

1. The residual error between the reconstructed image and the capacitance measurements:

Table 4.1: Equivalent diameter of the reconstructed objects using the classical reconstruction algorithms.

d_{obj}	55 mm	50 mm	44 mm	40 mm	27 mm
LBP	×	×	×	×	×
ILBP	57 mm	53 mm	49 mm	42 mm	18 mm

$$f_1 = \|\Delta\vec{C} - S\vec{\alpha}\|^2. \tag{4.10}$$

2. The negative Shannon's image entropy:

$$f_2 = \sum_i^N \alpha_i \ln(\alpha_i). \tag{4.11}$$

3. The image peakedness

$$f_3 = \vec{\alpha} X \vec{\alpha}^T + \vec{\alpha}\vec{\alpha}^T. \tag{4.12}$$

Where X is called the non-uniformity matrix.

Finally, the reconstruction problem is stated as:

$$\text{minimize: } \sum_{i=1}^{3} \lambda_i f_i \tag{4.13}$$

where λ_i is a specific weight given to each one of the functions.

Figure 4.6 shows the reconstructed images for the test cases obtained using the MOIRT algorithm. We notice that we are able to recognize 2 spherical objects in the sensing region. However, the small sphere looks blurred and the void region inside the sphere is not accurately captured. We can still calculate the equivalent diameter using the methodology described above. Table 4.2 summarizes our results. We can see that the MOIRT approach performs better for small object, but without losing accuracy for big objects.

Although the last two algorithms seemed capable of accurately reconstructing the three dimensional solid volume fraction distribution inside the sensing region, they rely on an iterative process to minimize their cost functions. For comparison, the ILBP algorithm takes in average 2.2 s to converge to a solution for a single image, while the MOIRT scheme takes 25 min. However, for a fluidized bed application, we are interested in gathering images over a significant amount of time to be able to obtain accurate statistical results. At this rate,

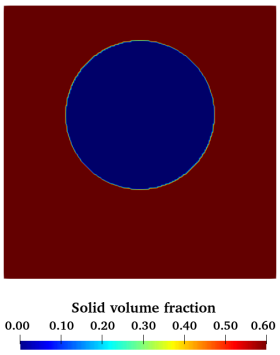

(a) True distribution $d_{\text{sphere}} = 55\,\text{mm}$.

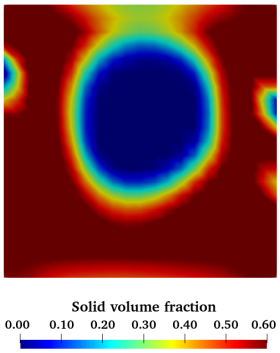

(b) Reconstructed distribution.

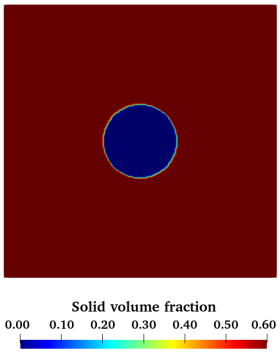

(c) True distribution $d_{\text{sphere}} = 27\,\text{mm}$.

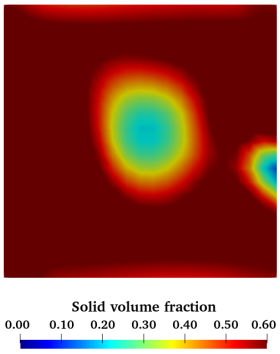

(d) Reconstructed distribution.

Figure 4.6: Static test case of a single void sphere in the middle of a fixed bed of glass beads. Vertical slice comparison between the true solid volume fraction distribution and the reconstructed image using the MOIRT algorithm.

reconstructing 1 minute of a fluidized bed dynamics at a acquisition frequency of 100 images per second could take around 4 hours for the ILBP algorithm and more than 3 months for the MOIRT algorithm. Given that neither of the approaches studied was 100% accurate, and that the reconstruction time is very high, we decided to explore a new approach using artificial intelligence-based algorithms.

Table 4.2: Equivalent diameter of the reconstructed objects using the classical reconstruction algorithms.

d_{obj}	55 mm	50 mm	44 mm	40 mm	27 mm
LBP	×	×	×	×	×
ILBP	57 mm	53 mm	49 mm	42 mm	18 mm
MOIRT	56 mm	54 mm	49 mm	43 mm	23 mm

4.3 Machine learning image reconstruction algorithms for ECVT systems

Machine learning techniques aim at developing a self-tuning mathematical model able to classify their input into known categories or to predict a likely output of a system given a set of inputs. The key requirement to implement a machine learning algorithm is a training dataset. This database is used to adjust the internal parameters of the mathematical model, so the algorithm can correctly predict the output of a given input. Nowadays, Artificial Neural Networks (ANN), a type of machine learning algorithm, have attracted significant attention due to their remarkable performances. ANNs allow to easily build highly non-linear models, allowing us to predict very complex phenomena. Many fields have already benefited from this approach: image recognition (He et al., 2016; Krizhevsky et al., 2012), natural language processing (Mikolov et al., 2013), bioinformatics (Alipanahi et al., 2015), and even chemical engineering (Venkatasubramanian, 2019).

4.3.1 Artificial neural networks

An ANN is a set of nodes, called neurons, organized in inter-connected layers (figure 4.7). In a feed-forward ANN, a signal transits through the network from the input layer to the output layer. Each connection between two neurons i and j has a weight w_{ij} associated to it. A single neuron receives the inputs from all the neurons in the previous layer and then computes the sum of all these values. After this, the final results is passed through a predefined activation function. The result from that activation function is the output of the neuron that is propagated into the next layer (figure 4.8).

The network can be trained so that the last layer outputs a desired signal for a given input signal in the first layer. To do so, a training database containing pairs of input and output vectors of values is used. An input vector is propagated through the network, and the error between the observed and expected output vector is measured via a loss function. The weights of the networks are subsequently modified by back-propagation so that the loss function is minimized.

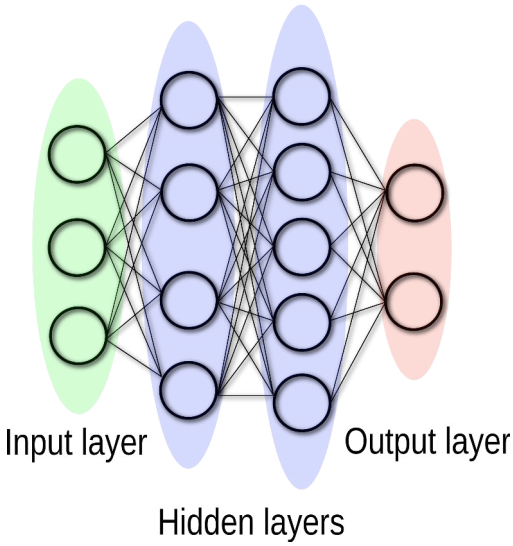

Figure 4.7: Illustration of a feed-forward artificial neural network with one input layer, two hidden layers and one output layer.

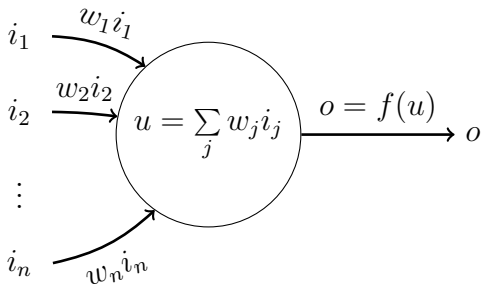

Figure 4.8: Illustration of how a single neuron works in an artificial neural network

Recently, ANN-based approach algorithms have been applied to the tomography image reconstruction problem. In the medical field there have already been some attempts to obtain more accurate images for the different imaging techniques. PET (Gong et al., 2019), X-ray CT (Cierniak, 2009; Gupta et al., 2018), MRI (Schlemper et al., 2018), and SPECT (Floyd, 1991), are some of the systems that have explored the pertinence of deep learning algorithms for the image reconstruction problem. The results show that a deep learning approach might be suitable for this type of problem; even in some cases outperforming the classical reconstruction algorithms.

In the last years, some efforts have been made towards the use of deep learning strategies for the image reconstruction problem in 2D ECT systems. Some approaches have used the raw capacitance data to try to predict the key hydrodynamics parameters: the average volume fraction, flow patters and bubble diameter (Garbaa et al., 2014; Guo et al., 2019; Zainal-Mokhtar and Mohamad-Saleh, 2013). These studies, however, did not tackle the

image reconstruction problem directly.

Recently, some works have been conducted to use artificial neural networks to address the image reconstruction problem of ECT devices. The ANN takes the capacitance measurements as input and it aims to predict the 2D volume fraction distribution. This technique has been very successful, with results that can compare with the most performing algorithm already found in the literature. As we mentioned, machine learning algorithms require a training database from which to learn. In our case, this database should be composed by pairs of capacitance measurements and their corresponding solid volume fraction. Nevertheless, previous studies on the topic do not offer a satisfactory methodology to build this training database. Lei et al. (2018) proposed to use images reconstructed with classical algorithms. However, the ANN risks of learning the shortcomings of the algorithm used. A different approach was taken by Zheng et al. (2018). They build a software that creates random 2D volume fraction distribution resembling patterns found in liquid-gas systems (stratified, annular and core flows). Then, using an electrodynamics simulation software, they calculated the capacitance values associated to the volume fraction distribution. The main drawback of this approach is that generating random volume fraction distribution for fluidized beds applications is much more difficult. Unlike the liquid-gas patterns, the 3D solid volume fraction distribution inside a fluidized bed is much more complex and unpredictable. Also, we would need an additional software and knowledge to perform the electrodynamics simulations. The proposed methodologies and training databases in these previous works are very difficult to apply to research groups that just acquired a new ECT/ECVT device with a different geometry or number of sensors. In the following sections we will propose two different strategies to generate a training database that can be easily implemented in any ECVT device.

4.4 CFD-Generated training database

The first strategy we used to generate the training dataset is based on CFD simulations. As mentioned before, previous works have already trained ANNs using artificially generated volume fraction distributions and computing the associated capacitance values using electrodynamics simulations (Zheng et al., 2018). Although this approach might be suitable for some patterns present in gas-liquid system, it is difficult to generalize to more complex configurations. For example, fluidized beds are known to have very complicated and chaotic behaviors, like bubbles breakup and coalescence or turbulent dynamics. These volume fraction distributions are much harder to generate artificially due to their complexity and unpredictability. Therefore, an artificially generated database with structured patterns might not be suitable for fluidized bed applications.

Nevertheless, modern CFD packages are very capable of accurately reproducing the inter-

nal dynamics of fluidized bed reactors, including these complex patterns. These simulations provide us with information about the instantaneous solid volume fraction distribution at each time step. We can couple this data with the sensitivity matrix approach and calculate the inter-plate capacitance values associated with the 3D distribution (equation 4.5). If we do this for different time steps, we can build a database containing 3D solid volume fraction distributions and their corresponding inter-plate capacitance measurements (figure 4.9).

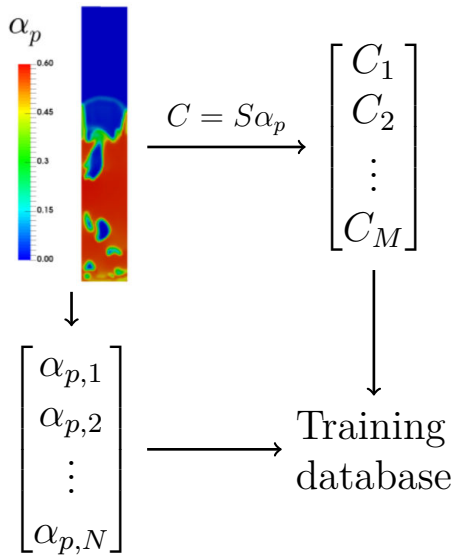

Figure 4.9: Strategy used to generate the training database for the artificial neural network.

Using this $\{\vec{C}; \vec{\alpha}\}$ training database, we then can fit our neural network using a supervised learning approach. In this approach, the training algorithm works as follows:

1. The structure of the neural network must be defined (i.e. number of layers, number of neurons per layer and activation functions for each neuron).

2. The connection weights are randomly initialized.

3. A capacitance vector in the training database is chosen and fed to the neural network.

4. The output of the neural network $\vec{\alpha}'$ is compared against the expected output in the training database.

5. The error between the expected output and the ANN's output is used to modify the weights by back propagation.

6. If the error is small enough, we can stop the process and we have a trained neural network, if not we go back to step 3.

This algorithm is repeated until the error is below some threshold or until the error does not decrease further. Figure 4.10 visually summarizes the training algorithm.

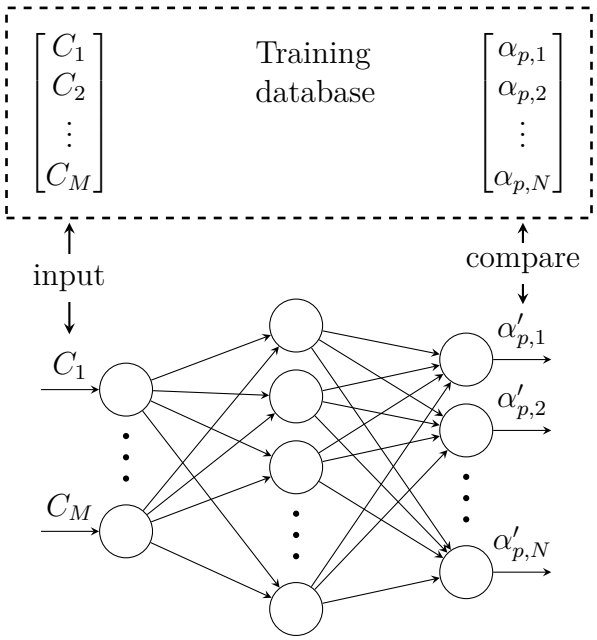

Figure 4.10: Training strategy using CFD generated data.

4.4.1 Implementation

To achieve this idea, we established a collaboration with the Computer Science Institute of Toulouse (IRIT by its acronym in French). They have the sufficient knowledge and equipment to efficiently design, train and evaluate machine learning algorithms. They proposed to build an feed-forward artificial neural network using Keras and TensorFlow, two Python libraries developed at Google (Abadi et al., 2015; Chollet and Others, 2015). The objective was to train a model to be able to reconstruct the images associated to our ECVT device.

The artificial neural network used is composed of an input layer of 630 neurons (corresponding to the 630 capacitance measurements in our ECVT system) followed by 3 hidden layers of 1,024, 2,048 and 4,096 neurons respectively and a final output layer of 8,000 neurons corresponding to the 8,000 values of solid volume fraction. In order to ensure that the solid volume fraction predicted by the neural network is bounded between 0 and 0.64 (the solid volume fraction at maximum packing), we enforced a scaled sigmoid activation function for the output layer of the ANN:

$$\alpha_{p,i} = 0.64 \frac{1}{1 + e^{-u_i}} \tag{4.14}$$

Meanwhile, the intermediate layers have a standard ReLU (Rectified Linear Unit) activation function:

$$f(u_i) = \max(0, u_i) \tag{4.15}$$

4.4.2 CFD Simulations

In order to simulate our fluidized bed reactor, we used the CFD software NEPTUNE_CFD. This is a multiphase Euler-nfluid code developed in the framework of the NEPTUNE project, financially supported by CEA, EDF, IRSN and Framatome. It is capable of solving particle–laden flow problems in complex geometries using structured and non-structured meshes. This code has been extensively validated for fluidized bed configurations using very accurate experimental techniques such as PEPT and RPT (Ansart et al., 2017; Fede et al., 2016; Fotovat et al., 2015; Sabatier et al., 2020). NEPTUNE_CFD is a massively parallel code (Neau et al., 2020), which allows us to obtain enough simulated data to build our training database. The simulated geometry is a replica of our experimental column of 10 cm internal diameter and 1 m height. We used an O-grid mesh with 400,000 cells of approximately 3 mm length (figure 4.11). For the solid phase we used glass beads of 250 μm diameter with a density equal to $2,700\,\mathrm{kg/m^3}$. The gas phase is air at 20 °C and atmospheric pressure. The initial height of the fluidized bed is set to 17 cm.

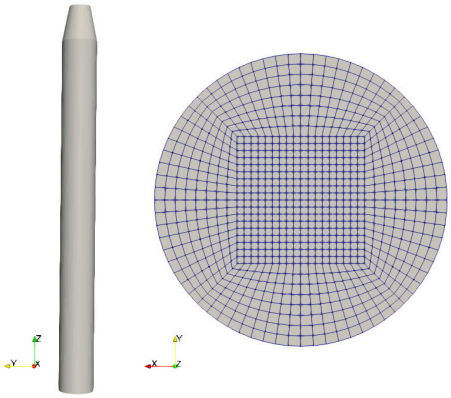

Figure 4.11: Geometry and mesh used in the numerical simulations.

If we want the neural network to generalize well, the training database must contain as much diverse information as possible. To achieve this, we simulated 4 different cases, each one with a different inlet velocity ($3U_{mf}$, $4U_{mf}$, $6U_{mf}$ and $7U_{mf}$), where $U_{mf} = 6.3\,\mathrm{cm/s}$ is the minimum fluidization velocity obtained using Ergun's correlation (Ergun and Orning, 1949). For each simulation, we recorded the solid volume fraction distribution in the 8,000 voxels

corresponding to the exact location of the voxels reconstructed by the ECVT system. For each case, we simulated 30 s of physical time. We extracted the solid volume fraction inside a 10 cm height region between $h_1 = 6$ cm and $h_2 = 16$ cm, where $h = 0$ cm represents the column inlet. The acquisition frequency was set to 100 images per second. This frequency is high enough to capture the bubbles passing through the sensing region. The final database, is, therefore, composed of 12,000 pairs of capacitance/solid volume fraction vectors.

4.4.3 Training phase

A common practice before the training phase of any machine learning algorithm is to split the training database into two smaller subsets: a training subset and a validation subset. The training subset is used to train the model using the methodology described earlier. The validation subset is used to monitor the performance of the model with data that is not present in the training subset. In our case, we split the training database into 80% for the training subset and 20% for the validation subset.

For the training phase itself, there are two key parameters to specify: the batch size and the number of epochs. The first one refers to the number of samples of the training database that will be used to compute the loss function before updating the ANN weights. For example, if our training database consists of 9,000 samples, and if we choose the batch size equal to 20, first, the entries 1-20 in the training database will be fed to our neural network and the loss function of these 20 entries will be used to change the weights w_{ij}. Then, we will feed the entries 21-40 to the updated ANN and the new loss function value is used to change again the weight values. This process is repeated until all 9,000 entries are used. A small batch size could allow us to train the database faster because the weights are updated more frequently. However, choosing a very small batch size could generate important fluctuations that could harm the convergence rate. The second parameter that has to be specified is the number of epochs. The epochs are the number of times the whole database is used during the training phase. If the number of epochs is set to 10 this means that the learning algorithm will go over the 9,000 samples 10 times. A high number of epochs can improve the quality of the ANN, but this could be also very time–consuming. In our example we chose the batch size equals to 20 and we trained for 3,000 epochs.

In order to monitor the convergence of the ANN, we can calculate the Root Mean Squared Error (RMSE) between the predicted (α'_p) and the expected (α_p) solid volume fractions values (equation 4.16)

$$\mathrm{RMSE}_{\alpha_p} = \sqrt{\frac{1}{n}\sum_{i=1}^{n}\left(\alpha_{p,i} - \alpha'_{p,i}\right)^2} \tag{4.16}$$

Where n is the total number of voxels in the sensing region.

In figure 4.12, we can see the RMSE during the training phase using the training and the validation subsets. As we can observe, the RMSE decreases as the number of epochs increases for the training subset. This means that for each epoch the output predicted by the neural network is closer to the expected output. We observe the same trend when we evaluate the accuracy of the neural network using the validation subset. This highlights that the trained ANN generalizes well for data outside the training subset. After 3,000 epochs, we see that RMSE is decreasing slowly which means that the training algorithm has converged. Now, we can take the neural network obtained in the last epoch and use it to reconstruct images using new data.

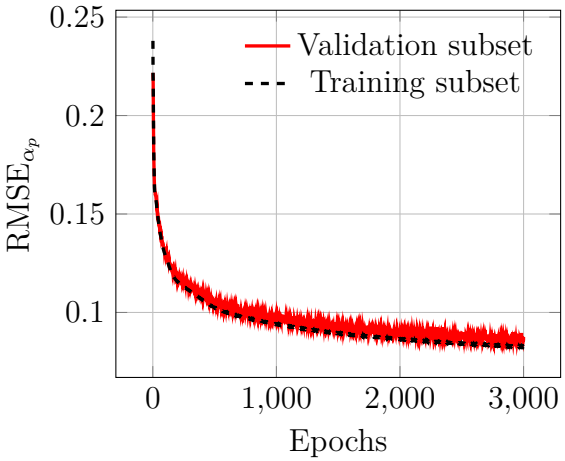

Figure 4.12: Root mean square error as a function of the training epochs.

4.4.4 Neural network evaluation

Once the training stage was completed, we can evaluate the performance of the model. First, we analyzed the neural network using simulated data. Using NEPTUNE_CFD, we performed another numerical simulation for a gas inlet velocity different to those present in the training database ($5U_{mf}$). From this simulation, we extracted the solid volume fraction distribution and we computed the capacitance values associated to those distributions. Then, we fed these capacitance values to the trained ANN, and we compared the output against the numerical simulation. This is done in figure 4.13, where we contrast a 2D axial slice in the middle of the column at three different time steps. The first 2 images corresponds to the first moments after fluidization started, where we have two symmetrical bubbles rising. The second pair of images is the moment where a big air bubble rises and finally the last 2 images correspond to a more complex structure appearing in the reactor. We remark that for all three cases, the reconstructed images are very close to the output of the numerical simulation. These results show that our ANN is capable of accurately reconstructing ECVT images of a fluidized bed.

We can extend our analysis further by looking at the RMSE between the ANN's output and the numerical simulation (which is the expected distribution). Figure 4.14 shows exactly this. The black line represent the instantaneous error of the ANN's prediction, while the blue dashed line is the average over all time. As a comparison, we also drew in dashed lines the mean RMSE of the images obtained with the classical algorithms. This shows that the ANN is very close to the most accurate algorithms. If we compute the mean absolute error between the simulated values and the predicted values, we get that the ANN predictions have an error in α_p of 0.06. Given that the average α_p value in a fluidized bed is of the order of 0.40, our ANN model has a prediction error of 15%.

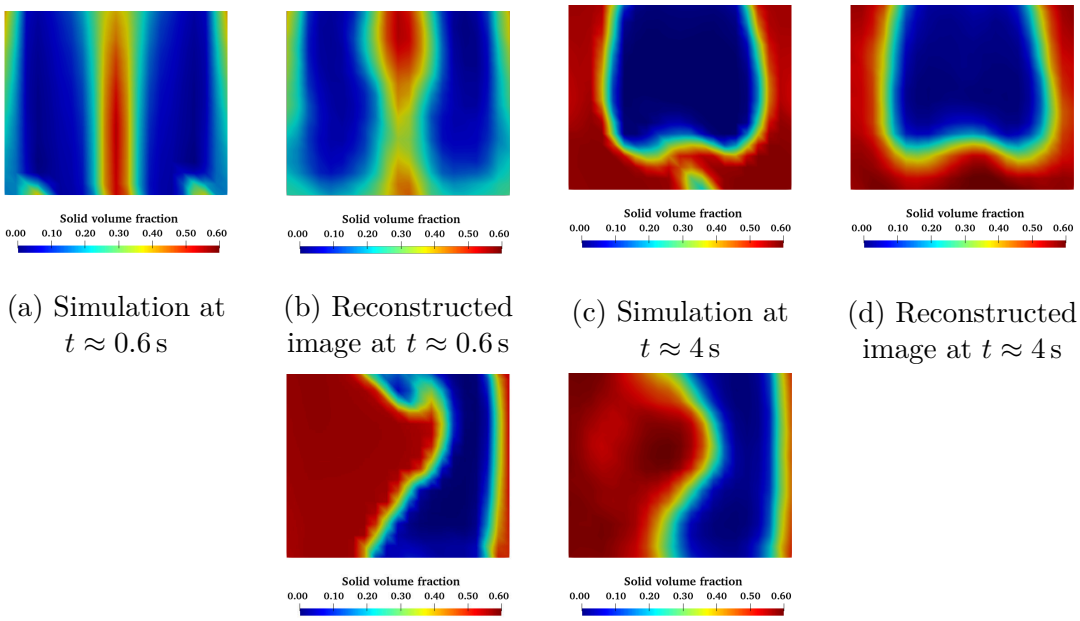

(a) Simulation at $t \approx 0.6\,\mathrm{s}$

(b) Reconstructed image at $t \approx 0.6\,\mathrm{s}$

(c) Simulation at $t \approx 4\,\mathrm{s}$

(d) Reconstructed image at $t \approx 4\,\mathrm{s}$

(e) Simulation at $t \approx 12\,\mathrm{s}$

(f) Reconstructed image at $t \approx 12\,\mathrm{s}$

Figure 4.13: Comparison of some instantaneous solid volume fraction distributions between the numerical simulations and the reconstructed image using an ANN (2D axial slice representation).

We can also test this neural network using the experimental data obtained with the void spheres in a fixed bed of glass beads. Figures 4.15 and 4.16 show a slice of the reconstructed volume for both the small and the big sphere. These images show that the ANN was able to detect a spherical object inside the volume. Like for the classical algorithms, the big sphere is much easier to recognize than the small sphere. We can characterize the diameter of all test spheres using the same criteria as before (see table 4.3). As we can see, we have an overestimation for every object. However, these values are still close to the real expected value.

Once the neural network has been trained, the reconstruction process is very fast because

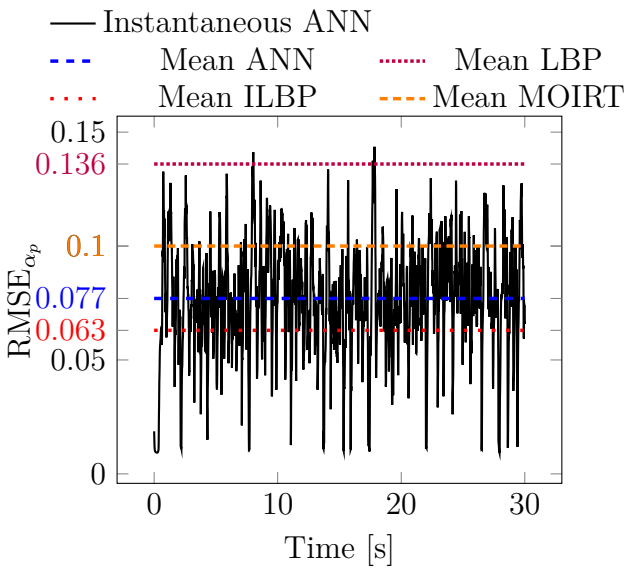

Figure 4.14: Root mean square error as a function of time between the numerical simulation and the image reconstructed by the ANN. The blue dashed line represent the time average, and the rest of colored dashed lines represent the time average of the RMSE using the classical algorithms.

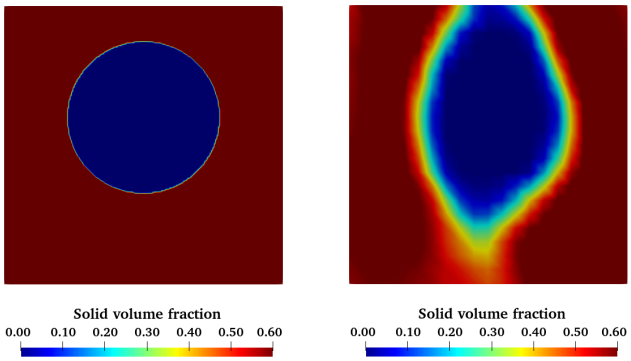

(a) True distribution (b) Reconstructed image

Figure 4.15: Comparison between the expected solid volume fraction distribution and the reconstructed solid volume fraction distribution for a void sphere of $d_{\text{sphere}} = 55\,\text{mm}$ (2D axial slice representation).

it only requires to propagate the capacitance signal through the network. This makes this strategy much more efficient than the traditional iterative algorithms. However, the training phase can be computationally expensive depending on the size and complexity of the network, the number of epochs, and the size of the training database. Our neural network took around 10 hours to perform the entire training phase, for the same computing power described above.

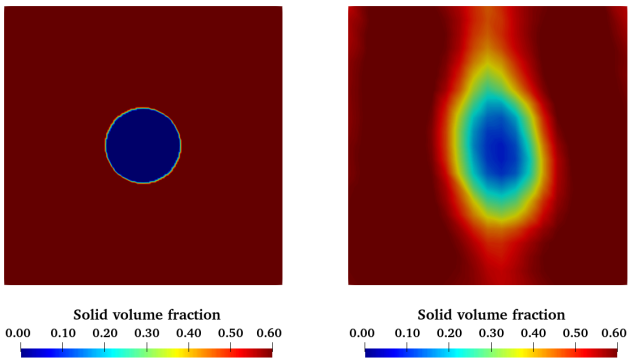

(a) True distribution (b) Reconstructed image

Figure 4.16: Comparison between the expected solid volume fraction distribution and the reconstructed solid volume fraction distribution for a void sphere of $d_{\text{sphere}} = 27\,\text{mm}$ (2D axial slice representation).

Table 4.3: Equivalent diameter of the reconstructed objects using the classical algorithms and an artificial neural network trained using a supervised learning technique.

d_{obj}	55 mm	50 mm	44 mm	40 mm	27 mm
LBP	×	×	×	×	×
ILBP	57 mm	53 mm	49 mm	42 mm	18 mm
MOIRT	56 mm	54 mm	49 mm	43 mm	23 mm
ANN	60 mm	59 mm	55 mm	50 mm	31 mm

Nevertheless, this neural network can reconstruct 1 image in around 50 ms. This shows, that ANN-based reconstruction models can be very accurate and very fast at the same time.

Our results prove that an artificial neural network trained using CFD-generated data is a valid approach to address the ECVT reconstruction problem. Our system was tested against dynamic simulated and real static data for which the expected solid volume fraction distributions are known. In both cases the ANN performed as well as the already known approaches. However, we observe a significant gain in post-processing time without loosing accuracy. This makes this approach suitable for system where an instantaneous feedback is needed, or when we need to reconstruct a large number of images. However, an non-negligible drawback is the necessity of a CFD software to generate the simulated data. This means that this approach depends on other simulation tools. In addition to this, we need to make sure that the simulated data represents accurately the physical phenomenon; any bias or error present in the simulated data could also be reproduced by the neural network. In the next section we present a different approach to make a standalone artificial neural network.

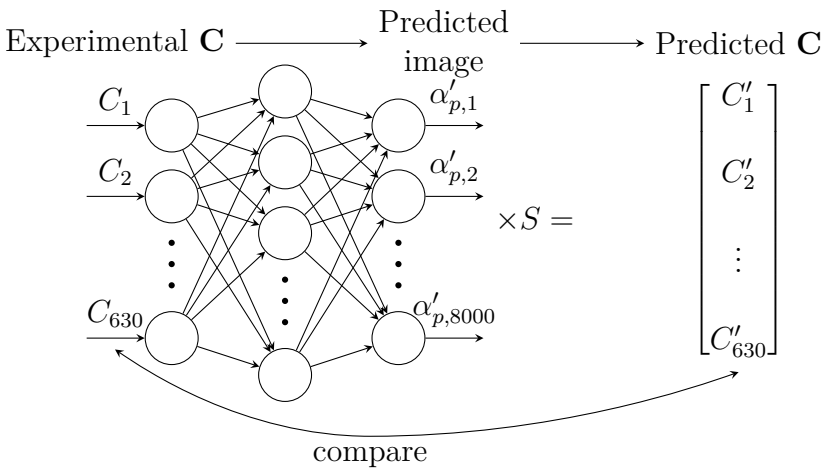

Figure 4.17: Training strategy using a training database with only experimental data.

4.5 Experimental data-generated database

In the previous section, we were able to successfully train an artificial neural network using simulated data coming from CFD software. However, this approach makes the ANN dependable on an external tool. In addition to this, doing high resolution numerical simulations can be computationally expensive and even inaccurate if the current models are not well adapted to the physical phenomenon. To remedy these problems, we propose a second strategy to build the training database needed for the training phase of the ANN. In this approach, we no longer need a database composed of input/outputs. Instead, we use directly experimental data even without knowing the solid volume fraction distribution.

The key aspect of this approach is that we know how to estimate the capacitance measurements given a solid volume fraction distribution. Therefore, during the training phase, we can directly feed experimental data $\vec{C}$ into the ANN. Instead of comparing the AAN's output $\vec{\alpha_p}'$ to some true $\vec{\alpha_p}$ distribution, we are going to use equation 4.5 to transform our predicted $\vec{\alpha_p}'$ into predicted capacitance values $\vec{C}'$. If the neural network is well trained, the values $\vec{C}$ and $\vec{C}'$ must be similar (figure 4.17). If this is not the case, then the internal weights have to be adjusted. Hence, our neural network will be trained so it minimizes the RMSE between $\vec{C}$ and $\vec{C}'$:

$$\text{RMSE}_C = \sqrt{\frac{1}{m}\sum_{i=1}^{m}(C_i - C'_i)^2} \tag{4.17}$$

This approach has the advantage of not needing computer–simulated data to train the

model. We can now directly use experimental data, even without having previous knowledge of the true solid volume fraction distribution. This makes this technique completely independent of any external tool. Another advantage is that we can use any new experimental data to simultaneously reconstruct the solid volume fraction and to train even further the neural network. In contrast with the previous approach, where the experimental data cannot be used to improve the neural network. So this technique allows us to have a self-sufficient ANN that can be in a constant learning process.

4.5.1 Experiments

To be able to compare this strategy with the previous approach, we built a training database as similar as possible to the one generated by CFD. We ran experiments in the fluidized bed column described in section 4.1. The dimensions of this column are identical to the simulated fluidized bed. The solid phase is composed of spherical glass beads. The characterization of this granular material was already performed by Nasro Allah (2019). The median diameter is equal to $d_{50} = 267\,\mu$m, the span of the particle size distribution is equal to 0.43, which allows us to consider the powder as monodisperse. Finally, the density of the material is equal to $\rho_p = 2476.1 \pm 0.3\,\mathrm{kg/m^3}$

The gas phase is air at ambient pressure and ambient temperature. Using the humidification control system, we set the relative humidity equal to 50%, to remove any electrostatic effects in the solid phase. Similarly to the numerical simulations, we performed 4 different experiments with 4 different inlet velocities ($3U_{mf}$, $4U_{mf}$, $6U_{mf}$ and $7U_{mf}$). The ECVT device was placed between $h_1 = 6\,$cm and $h_2 = 16\,$cm ($h = 0\,$cm corresponds to the inlet of the fluidized bed). The acquisition frequency was set to 50 frames per second. For each inlet velocity, we gathered 3,000 measurements of capacitance. This allows us to obtain a training composed of 12,000 capacitance vectors.

The neural network used has the exact same architecture as the one used before. To transform the solid volume fraction distribution predicted by the neural network to capacitance values, we used the sensitivity matrix associated with our ECVT device. The training parameters were also similar, we set the batch size to 20 and we ran the training for 3,000 epochs.

Figure 4.18 shows the evolution of the RMSE as a function of the training epochs. We remark that the RMSE decreases when the number of training epochs increases. This means that the neural network is converging to a better solution. This behavior is true for both the training and the validation databases. This shows that this ANN can also be used for data that was not present in the training database

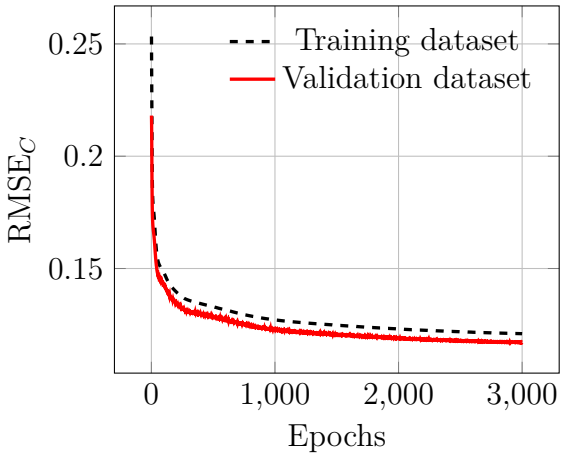

Figure 4.18: Root mean square error as a function of the training epochs.

Neural network evaluation

With this trained artificial neural network, we can perform the same analysis as we did for the previous one. First, we can feed our ANN with simulated data and compare the reconstructed images with the numerical simulation. In figure 4.19, we can see that, qualitatively, the results produced by this approach are in good agreement with the expected results. However, they are not as good as the results produced by the CFD-trained ANN. The two symmetrical bubbles rising at the start of the simulation are not well captured (figure 4.19a and 4.19b). For the big bubble (figure 4.19c and 4.19d) and the complex structure near the wall (figure 4.19e and 4.19f) we obtain a more accurate reconstruction. Nevertheless, the results are worse than the previous ANN strategy.

Figure 4.20 represents the root mean squared error between the numerical simulation and the reconstructed image as a function of the simulation time. We can see that the mean RMSE value is around 0.13, which is worse than the previous ANN. This curve also shows that this ANN is also not as good as the ILBP and MOIRT algorithms. However, it does perform better than the LBP scheme. For this approach, the mean absolute error between the predicted and the expected solid volume fraction values is equal to 0.08. This means that this approach has an error of 22% compared to the mean solid volume fraction found in a fluidized bed.

We can also test this approach using the data gathered from the real ECVT system with known object inside a fixed bed of particles. We fed the experimental data as input of the trained ANN and then we calculated the equivalent diameter of the reconstructed objects d_{obj}. We summarized our results in table 4.4. Firstly, we noticed that our new approach failed to reconstruct the two smallest objects we tested. This means that the performance of this ANN has deteriorated compared to our previous approach. Nevertheless, this technique

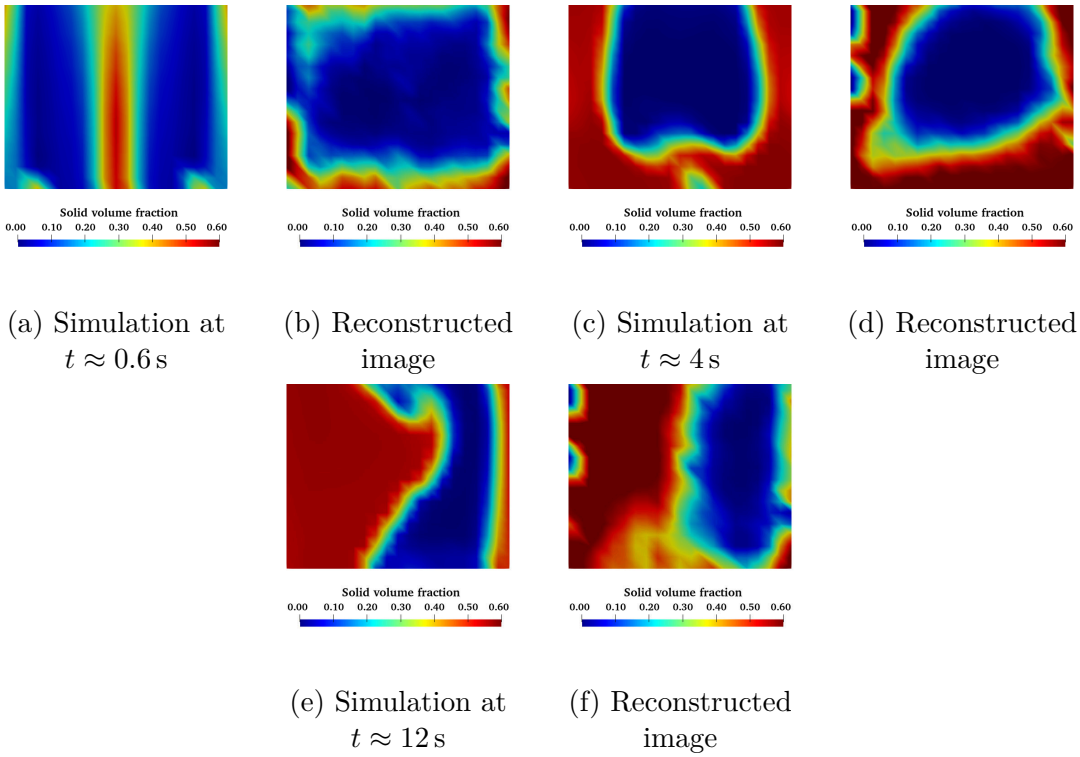

(a) Simulation at $t \approx 0.6\,\mathrm{s}$

(b) Reconstructed image

(c) Simulation at $t \approx 4\,\mathrm{s}$

(d) Reconstructed image

(e) Simulation at $t \approx 12\,\mathrm{s}$

(f) Reconstructed image

Figure 4.19: Comparison of some instantaneous solid volume fraction distributions between the numerical simulations (left) and the reconstructed image using an ANN trained with experimental data (right) (2D axial slice representation).

was able to reconstruct accurately the bigger void spheres with an equivalent diameter which is close to the real diameter. A visual comparison is made in figures 4.21 and 4.22. These images reveal that our ANN has no problem detecting big void objects inside a fixed bed of glass particles. It does however fail to reconstruct the smallest of our test objects. This shows that for a similar training database and network architecture, the ANN trained using experimental data does not perform as well as the ANN trained using CFD simulations.

These results prove that we can train an artificial neural network using solely experimental data in order to address the image reconstruction problem for 3D ECVT systems. Our ANN was tested against both simulated and real data. The results highlight that this approach is also suitable as an image reconstruction algorithm. Although the results were slightly worse compared to the first strategy, this approach is completely self-sufficient and does not need any external tool. This strategy will also benefit from any new experimental data to further learn and increase its quality.

Despite the fact that this training technique did not perform as well as the previous one, it is worth noting that there are some fundamental differences between these two approaches. The CFD data used to train our first artificial neural network was totally free from noise,

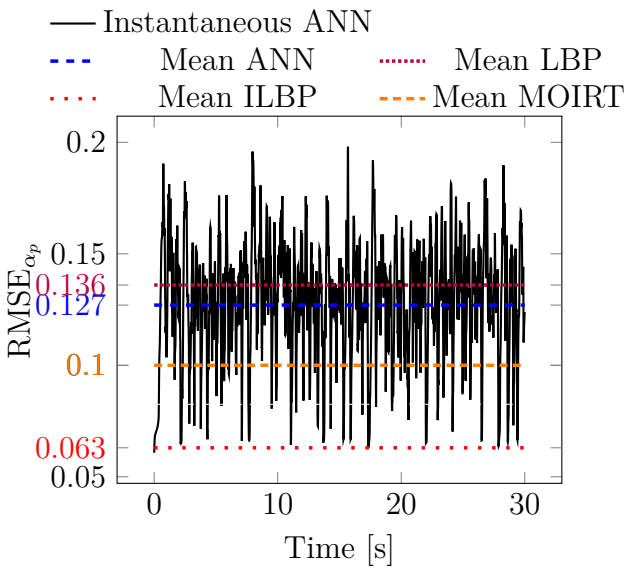

Figure 4.20: Root mean square error as a function of time between the numerical simulation and the image reconstructed by the ANN. The blue dashed line represent the time average, and the rest of colored dashed lines represent the time average of the RMSE using the classical algorithms.

while the experimental data is always convoluted with noise generated by the acquisition configuration. At this stage it is unknown the effect of this noise on the quality of the training process. This is something that should be taken into account when working with this approach, however it is unclear how this effect could be modeled.

Table 4.4: Equivalent diameter of the reconstructed objects using the classical algorithms and artificial neural network trained using CFD simulations and the artificial neural network trained using experimental data.

d_{obj}	55 mm	50 mm	44 mm	40 mm	27 mm
LBP	×	×	×	×	×
ILBP	57 mm	53 mm	49 mm	42 mm	18 mm
MOIRT	56 mm	54 mm	49 mm	43 mm	23 mm
CFD-trained	60 mm	59 mm	55 mm	50 mm	31 mm
Exp-trained	56 mm	53 mm	43 mm	×	×

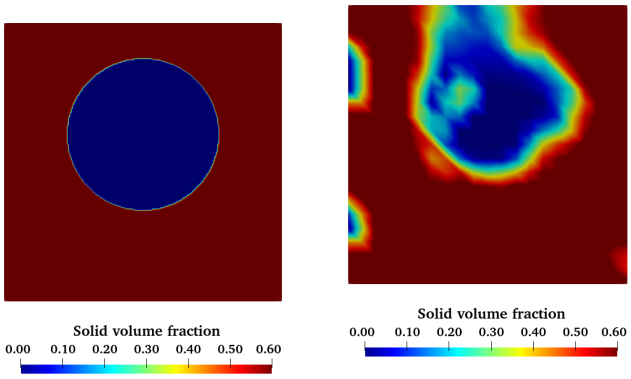

(a) True distribution.

(b) Reconstructed image.

Figure 4.21: Comparison between the expected solid volume fraction distribution and the reconstructed solid volume fraction distribution for a void sphere of $d_{\text{object}} = 55\,\text{mm}$ using a the reinforcement learning technique (2D axial slice representation).

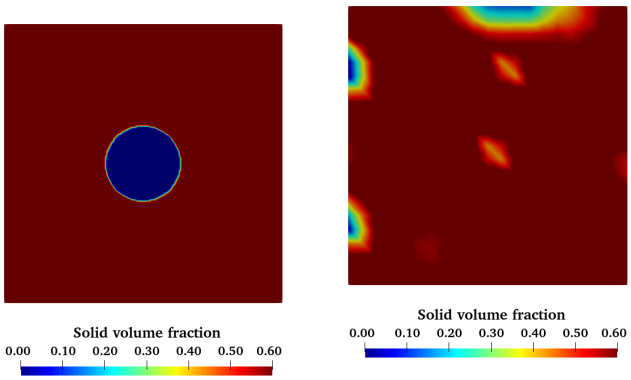

(a) True distribution.

(b) Reconstructed image.

Figure 4.22: Comparison between the expected solid volume fraction distribution and the reconstructed solid volume fraction distribution for a void sphere of $d_{\text{object}} = 27\,\text{mm}$ using a the reinforcement learning technique (2D axial slice representation).

4.6 Conclusion

In this chapter, we presented two different strategies to build a training database for a machine learning based algorithm for ECVT systems applied to fluidized beds. A first proposition is based on accurate 3D numerical simulations. From these simulations, we can extract the solid volume fraction distribution in different regimes and conditions; and we can deduce the capacitance measurements using the sensitivity matrix model. This data allowed us to train an artificial neural network that tackles the image reconstruction problem in ECVT devices. This technique performed very well compared to the classical algorithms found in the literature. We were able to accurately reconstruct images coming from both simulated and real experimental data. The reconstructed images using simulated data was as accurate as the already known algorithms. We also tested the system with real experimental data. We placed different void spheres inside a fixed bed of glass particles. Using this ANN, we reconstructed the image and we calculated the diameter of the object seen. Our results showed a slight overestimation of the diameter. Although this approach was able to successfully rebuild images of an ECVT system, it depends on an external tool to generate the simulated training data.

The second approach is based experimental data without needing a previous knowledge of the solid volume fraction distribution. In this case, we aim at getting a reconstructed image that corresponds as closely as possible to the input capacitance values. In this way, we get a self-sufficient technique that does not depend on any other tool. This approach was trained using an equivalent experimental database to the one generated for the first approach. Our results show that this methodology is not as good as the previous approach, especially for small objects. Nonetheless, we obtained acceptable results when we need to reconstruct big objects.

For the sake of simplicity, this work only studied the most simple neural network configuration: a feedforward neural network. However, a more complex solution could be studied. Recurrent neural networks models such as LSTM (Hochreiter and Urgen Schmidhuber, 1997), or attention models inspired from the recent transformer architecture (Vaswani et al., 2017) would allow us to exploit the sequential nature of the inputs, which is ignored in the feedforward model. Another perspective of this work would be to use recurrent neural networks to predict the capacitance values at time t knowing the values at times $[t_0..t_{-1}]$. These predictions could be used for capacitance captors failure detection in ECVT systems. Another important aspect that was not investigated in this study is the effect that measurement noise can have in the quality of the results. Indeed, the CFD generated data was noiseless, while the experimental data is always convoluted with noise, this could explain some of the differences between the two approaches presented in this study. Finally, this research can be regarded as a proof of concept that artificial neural networks can be used as reconstruction techniques for ECVT images in fluidized bed applications. As such, the database used was relatively small and limited. Currently, there is an ongoing study using training databases

almost 20 times bigger than the ones presented here. This allows us, not only to better characterize the quality and efficiency of ANN-based reconstruction algorithms, but also it allows to test more complex network architectures.

Chapter 4 Bibliography

M. Abadi, A. Agarwal, P. Barham, E. Brevdo, Z. Chen, C. Citro, G. S. Corrado, A. Davis, J. Dean, M. Devin, S. Ghemawat, I. Goodfellow, A. Harp, G. Irving, M. Isard, Y. Jia, R. Jozefowicz, L. Kaiser, M. Kudlur, J. Levenberg, D. Mané, R. Monga, S. Moore, D. Murray, C. Olah, M. Schuster, J. Shlens, B. Steiner, I. Sutskever, K. Talwar, P. Tucker, V. Vanhoucke, V. Vasudevan, F. Viégas, O. Vinyals, P. Warden, M. Wattenberg, M. Wicke, Y. Yu, and X. Zheng. TensorFlow: Large-Scale Machine Learning on Heterogeneous Systems, 2015. URL `https://www.tensorflow.org/`.

B. Alipanahi, A. Delong, M. T. Weirauch, and B. J. Frey. Predicting the sequence specificities of DNA- and RNA-binding proteins by deep learning. *Nature Biotechnology*, 33(8):831–838, 2015.

R. Ansart, P. García-Triñanes, B. Boissière, H. Benoit, J. P.K. Seville, and O. Simonin. Dense gas-particle suspension upward flow used as heat transfer fluid in solar receiver: PEPT experiments and 3D numerical simulations. *Powder Technology*, 307:25–36, 2017.

F. Chollet and Others. Keras, 2015.

R. Cierniak. New neural network algorithm for image reconstruction from fan-beam projections. *Neurocomputing*, 72(13-15):3238–3244, 2009.

B. Du, Q. Marashdeh, W. Warsito, A.-H. A. Park, and L. S. Fan. Development of Electrical Capacitance Volume Tomography (ECVT) and Electrostatic Tomography (EST) for 3D Density Imaging of Fluidized Bed System. In *2007 ECI Conference on The 12th International Conference on Fluidization - New Horizons in Fluidization Engineering*, pages 473–480. Curran Associates Inc, 2007.

S. Ergun and A. A. Orning. Fluid Flow through Randomly Packed Columns and Fluidized Beds. *Industrial and Engineering Chemistry*, 41(6):1179–1184, 1949.

P. Fede, O. Simonin, and A. Ingram. 3D numerical simulation of a lab-scale pressurized dense fluidized bed focussing on the effect of the particle-particle restitution coefficient and particle-wall boundary conditions. *Chemical Engineering Science*, 142:215–235, 2016.

C. E. Floyd. An Artificial Neural Network for SPECT Image Reconstruction. *IEEE Transactions on Medical Imaging*, 10(3):485–487, 1991.

F. Fotovat, R. Ansart, M. Hemati, O. Simonin, and J. Chaouki. Sand-assisted fluidization of large cylindrical and spherical biomass particles: Experiments and simulation. *Chemical Engineering Science*, 126:543–559, 2015.

H. Garbaa, L. Jackowska-Strumillo, K. Grudzien, and A. Romanowski. Neural network approach to ECT inverse problem solving for estimation of gravitational solids flow. In *Federated Conference on Computer Science and Information Systems*, pages 19–26. IEEE, 2014.

K. Gong, J. Guan, K. Kim, X. Zhang, J. Yang, Y. Seo, G. E. Fakhri, J. Qi, and Q. Li. Iterative PET Image Reconstruction Using Convolutional Neural Network Representation. *IEEE Transactions on Medical Imaging*, 38(3):675–685, 2019.

Q. Guo, M. Ye, W. Yang, and Z. Liu. A machine learning approach for electrical capacitance tomography measurement of gas–solid fluidized beds. *AIChE Journal*, 65(6):e16583, 2019.

H. Gupta, K. H. Jin, H. Q. Nguyen, M. T. McCann, and M. Unser. CNN-Based Projected Gradient Descent for Consistent CT Image Reconstruction. *IEEE Transactions on Medical Imaging*, 37(6):1440–1453, 2018.

K. He, X. Zhang, S. Ren, and J. Sun. Deep Residual Learning for Image Recognition. In *Proceedings of the IEEE conference on computer vision and pattern recognition*, pages 770–778. IEEE, 2016.

S. Hochreiter and J. Urgen Schmidhuber. Long Shortterm Memory. *Neural Computation*, 9 (8):17351780, 1997.

A. Krizhevsky, I. Sutskever, and G. E. Hinton. Imagenet classification with deep convolutional neural networks. In *Advances in neural information processing systems*, pages 1097–1105. NIPS, 2012.

J. Lei, Q. Liu, and X. Wang. Deep Learning-Based Inversion Method for Imaging Problems in Electrical Capacitance Tomography. *IEEE Transactions on Instrumentation and Measurement*, 67(9):2107–2118, 2018.

Q. Marashdeh. *Advances in Electrical Capacitance Tomography*. PhD thesis, Ohio State University, 2006.

T. Mikolov, I. Sutskever, K. Chen, G. Corrado, and J. Dean. Distributed representations ofwords and phrases and their compositionality. In *Advances in Neural Information Processing Systems*, pages 1–9. NIPS, 2013.

Y. Nasro Allah. *Experimental and numerical investigation of electrostatic charges in gas-solid fluidized beds*. PhD thesis, Toulouse-INP, 2019.

H. Neau, M. Pigou, P. Fede, R. Ansart, C. Baudry, N. Mérigoux, J. Laviéville, Y. Fournier, N. Renon, and O. Simonin. Massively parallel numerical simulation using up to 36,000 CPU cores of an industrial-scale polydispersed reactive pressurized fluidized bed with a mesh of one billion cells. *Powder Technology*, 366:906–924, 2020.

F. Sabatier, R. Ansart, H. Zhang, J. Baeyens, and O. Simonin. Experiments support simulations by the NEPTUNE_CFD code in an Upflow Bubbling Fluidized Bed reactor. *Chemical Engineering Journal*, 385(June 2019):123568, 2020.

J. Schlemper, J. Caballero, J. V. Hajnal, A. N. Price, and D. Rueckert. A Deep Cascade of Convolutional Neural Networks for Dynamic MR Image Reconstruction. *IEEE Transactions on Medical Imaging*, 37(2):491–503, 2018.

A. Sowinski, F. Salama, and P. Mehrani. New technique for electrostatic charge measurement in gas-solid fluidized beds. *Journal of Electrostatics*, 67(4):568–573, 2009.

W. P. Taruno, M. R. Baidillah, R. I. Sulaiman, M. F. Ihsan, S. E. Fatmi, A. H. Muhtadi, F. Haryanto, and M. Aljohani. 4D brain activity scanner using Electrical Capacitance Volume Tomography (ECVT). In *Proceedings - International Symposium on Biomedical Imaging*, pages 1006–1009. IEEE, 2013.

A. Vaswani, N. Shazeer, N. Parmar, J. Uszkoreit, L. Jones, A. N. Gomez, Ł. Kaiser, and I. Polosukhin. Attention is all you need. In *Advances in Neural Information Processing Systems*, pages 5999–6009. NIPS, 2017.

V. Venkatasubramanian. The promise of artificial intelligence in chemical engineering: Is it here, finally? *AIChE Journal*, 65(2):466–478, 2019.

F. Wang, Q. Marashdeh, A. Wang, and L. S. Fan. Electrical capacitance volume tomography imaging of three-dimensional flow structures and solids concentration distributions in a riser and a bend of a gas-solid circulating fluidized bed. *Industrial and Engineering Chemistry Research*, 51(33):10968–10976, 2012.

W. Warsito and L.-S. Fan. Neural network based multi-criterion optimization image reconstruction technique for imaging two- and three-phase flow systems using electrical capacitance tomography. *Measurement Science and Technology*, 12(12):2198–2210, 2001.

J. M. Weber and J. S. Mei. Bubbling fluidized bed characterization using electrical capacitance volume tomography (ECVT). *Powder Technology*, 242:40–50, 2013.

J. M. Weber, K. J. Layfield, D. T. Van Essendelft, and J. S. Mei. Fluid bed characterization using electrical capacitance volume tomography (ECVT), compared to CPFD software's barracuda. *Powder Technology*, 250:138–146, 2013.

C. Xie, A. Plaskowski, and M. Beck. 8-electrode capacitance system for two-component flow identification. Part 1: Tomographic flow imaging. *IEE Proceedings A (Physical Science, Measurement and Instrumentation, Management and Education)*, 136(4):173–183, 1989.

W. Q. Yang, D. M. Spink, T. a. York, and H. McCann. An image-reconstruction algorithm based on Landweber's iteration method for electrical-capacitance tomography. *Measurement Science and Technology*, 10(11):1065–1069, 1999.

K. Zainal-Mokhtar and J. Mohamad-Saleh. An oil fraction neural sensor developed using electrical capacitance tomography sensor data. *Sensors (Switzerland)*, 13(9):11385–11406, 2013.

J. Zheng, J. Li, Y. Li, and L. Peng. A benchmark dataset and deep learning-based image reconstruction for electrical capacitance tomography. *Sensors*, 18(11):3701, 2018.

Chapter 5

Conclusions and perspectives

The main objective of this research work was to lay the foundations for the numerical and experimental study of electrostatic forces in fluidized beds in our research group. From the numerical side, we chose to address the Eulerian modeling of the mean particle electric charge. The Eulerian approach was selected as it is the only modeling strategy capable of handling industrial size problems. Yet no work on the subject had been published when this research project started. From the experimental side, we wanted to study the effect of electrostatic forces in a laboratory scale fluidized bed using a novel technique: The Electrical Capacitance Volume Tomography (ECVT). Experimental research on the hydrodynamics of fluidized bed with electrostatic forces was mainly conducted using intrusive local probes. Therefore, the ECVT system represents a step forward as it can provide the global information about the dynamics of the bed.

The first part of this thesis was dedicated to the modeling of the mean particle electric charge transport equation. Previous works published at the beginning of this project already derived a mean electric charge transport equation using the kinetic theory of granular flow. However, these studies assumed an uncorrelated form for the particle probability density function. In this thesis, we showed a methodology to overcome this limitation. Using linear approach to model the conditional mean electric charge, we were able to derive a more general transport equations for the mean particle electric charge and particle charge-velocity covariance. This allowed us to propose a simple algebraic model for the charge velocity-covariance term. Our results showed that, using an algebraic model, the covariance term takes the form of an extra kinetic triboconductivity and dispersion coefficients. These coefficients proved to be a more general version than the ones proposed in the previous works. The early results of this work were published in the proceedings of the Fluidization XVI conference held in Guilin, China in 2019 organized by the American Institute of Chemical Engineers (AIChE). A similar work was also the subject of an oral presentation in 10^{th} International Congress of Multiphase Flow (ICMF) held in Rio de Janeiro, Brazil in 2019. Finally, a full and detailed analysis was published in the Journal of Fluid Mechanics in 2020.

With this methodology, we also extended our approach to a more complete model taking into account not only the charge-velocity covariance but also the electric charge variance, which was neglected in the previous study. We were able to derive the transport equation for both the electric charge variance and the charge-velocity covariance. To fully close these equation we proposed simple algebraic closure models for the third order moments derived from a simplification of their transport equations. This model highlighted that charge variance term

induces an additional charge flux due to the electrostatic force. Therefore, neglecting the electric charge variance results in an underestimation of the charge kinetic dispersion in the regions with a strong electric field. However, we also analyzed possible simplifications to this complex model. We were able to derived a coupled algebraic model that takes into account the variance effects. Unfortunately, the resulting model could lead to non-physical results, especially in configurations where the potential electric energy is high. Given this important drawback, we explored an intermediary model where the covariance equation was simplified to an algebraic equation but the variance transport equation is kept. This modeling approach was more successful with similar results to the full 3 transport equation model. A preliminary analysis of this work was published in the proceedings 13$^{\text{th}}$ Conference of Fluidized Bed Technology (CFB) in 2021. Finally, the main results of this chapter will soon be submitted to a peer-reviewed journal.

The second part of this thesis focused on the development of an ECVT system to experimentally study the effect of electrostatic forces in fluidized beds in our research group. To accomplish this, we acquired a state-of-the-art ECVT device and we built an laboratory-scale fluidized bed. However, the default algorithm used to reconstruct the 3D solid volume fraction, was not accurate enough to allow us to perform any meaningful analysis. For this reason, we searched and try different reconstruction algorithms found in the literature. Although, some of these algorithms were very accurate, they relied in complex minimization problems which might be very time consuming to solve for a large volume of data.

This limitation motivated us to explore a different type of reconstruction algorithm based on machine learning techniques. We sought the collaboration of 2 different research groups: the department of Process and System Engineering in our laboratory and the Computer Science Research Institute of Toulouse (IRIT). From this partnership we developed the idea of training a feed forward artificial neural network to reconstruct images coming from our ECVT system. The key aspect of any machine learning algorithm is the training database used to fit the neural network coefficients. Previous studies had proposed some strategies to build a training database, however they were not suitable for fluidized bed configurations. In this thesis, we proposed two different methods to build such database for fluidized bed applications. The first proposition used CFD-generated data to simulate the capacitance measurements. This approach was very successful achieving performance comparable to the most accurate classical algorithms. The second proposition proposed relies exclusively in real experimental measurements, and no previous knowledge of the solid volume fraction distribution is required. This method was less accurate, but still it provided satisfactory results. The main advantage of a machine learning-based algorithm is that the computing time required to reconstruct the 3D image is much faster than any of the accurate classical approaches. This can speedup the analysis pipeline of experimental results. This research was presented in 2 different posters in the Dispersed Two-Phase flow meeting in Toulouse, France in 2018 and in the French Chemical Engineering Congress in 2019 in Nantes, France. Also, the results were published in the proceedings of the 13$^{\text{th}}$ CFB Conference. This research topic was also the subject of an invited presentation in the research FERMaT federation.

Finally, the main results of this work will soon be submitted to a peer-reviewed journal.

Many questions were left unanswered in this research work and some other have been opened. First of all, although we were able to derive the governing transport equations for the particle mean electric charge and the second order moments, their corresponding boundary conditions are still an open problem. These boundary conditions could probe to be a crucial part of the mathematical model. Especially because, as experimental evidence shows, the particle motion and charging dynamics near the walls are very peculiar and they heavily influence the evolution of the system. To tackle this problem, DNS or DEM simulations, or even experimental techniques such as RPT or PEPT, could provide very useful and detailed information about the behavior of the solid particles near the solid boundaries of the domain. This information could later be used to derive accurate Eulerian boundary conditions. Once these boundary conditions have been derived, we could proceed to the validation of the whole formulation. The resulting equations should be implemented in a CFD software and the results should be compared against experimental data.

Another open problem is the extension of the modeling approach presented in this work to polydisperse configurations. However, experimental data have shown that particles of different size could lead to a bipolar charging phenomenon. In this configuration, the attractive electrostatic force between particles with different polarities can create agglomerates or non-instantaneous non-binary collisions. These two phenomena go against the main hypotheses in the kinetic theory. Therefore, we believe that the development of an accurate Eulerian polydisperse mathematical model is far from straightforward.

In the experimental part, the main objective of using the ECVT technology to analyze effects of electrostatic force in a fluidized bed was not achieved and therefore should be the logical next step. The machine learning-based algorithms presented in this should be accurate enough to detect the presence of bubbles as well as their shape and velocity. This information can be used to compare the effect of electrostatic forces in the bubble's dynamics. Another effects that can be easily quantified with this technology is the effects of the electrostatic forces in the spatial distribution of the solid volume fraction. In particular, we could be able to distinguish the radial segregation of the solid phase towards the reactor's wall. Also, the fact that ANNs can reconstruct ECVT images almost instantly will allow us to record a large amount of data to have meaningful statistical results that can be used to validate the Eulerian model developed in this work.

The machine learning-based algorithm also opened some questions. In this work, a simple feed forward neural network was used. However, we do not claim that this is the optimal architecture to reconstruct ECVT images. Recursive neural networks, long/short term memory neural networks, convolution neural networks are all types of neural networks that have been used in image processing analysis and they could be valuable to address the ECVT image reconstruction problem. In addition to this, there are several points that are still unknown at this stage: optimal size of the training database, accounting for the noise present in the

real experimental measurements, and the performance of the algorithm when extrapolating with data way outside the training database.

General Bibliography

M. Abadi, A. Agarwal, P. Barham, E. Brevdo, Z. Chen, C. Citro, G. S. Corrado, A. Davis, J. Dean, M. Devin, S. Ghemawat, I. Goodfellow, A. Harp, G. Irving, M. Isard, Y. Jia, R. Jozefowicz, L. Kaiser, M. Kudlur, J. Levenberg, D. Mané, R. Monga, S. Moore, D. Murray, C. Olah, M. Schuster, J. Shlens, B. Steiner, I. Sutskever, K. Talwar, P. Tucker, V. Vanhoucke, V. Vasudevan, F. Viégas, O. Vinyals, P. Warden, M. Wattenberg, M. Wicke, Y. Yu, and X. Zheng. TensorFlow: Large-Scale Machine Learning on Heterogeneous Systems, 2015. URL `https://www.tensorflow.org/`.

M. Abbas, E. Climent, J. F. Parmentier, and O. Simonin. Flow of particles suspended in a sheared viscous fluid: Effects of finite inertia and inelastic collisions. *AIChE Journal*, 56 (10):2523–2538, 2010.

M. R. Abbasi, A. Shamiri, and M. A. Hussain. A review on modeling and control of olefin polymerization in fluidized-bed reactors. *Reviews in Chemical Engineering*, 35(3):311–333, 2019.

J. Adanez, A. Abad, F. Garcia-Labiano, P. Gayan, and L. F. De Diego. Progress in chemical-looping combustion and reforming technologies. *Progress in Energy and Combustion Science*, 38(2):215–282, 2012.

M. F. Al-Adel, D. A. Saville, and S. Sundaresan. The effect of static electrification on gas-solid flows in vertical risers. *Industrial and Engineering Chemistry Research*, 41(25):6224–6234, 2002.

F. S. Ali, M. A. Ali, P. Castle, and I. I. Inculet. Charge exchange model of a disperse system of spherical powder particles. In *Conference Record of 1998 IEEE Industry Applications Conference. Thirty-Third IAS Annual Meeting*, pages 1884–1891. IEEE, 1998.

N. Ali, T. Al-Juwaya, and M. Al-Dahhan. An advanced evaluation of spouted beds scale-up for coating TRISO nuclear fuel particles using Radioactive Particle Tracking (RPT). *Experimental Thermal and Fluid Science*, 80:90–104, 2017.

B. Alipanahi, A. Delong, M. T. Weirauch, and B. J. Frey. Predicting the sequence specificities of DNA- and RNA-binding proteins by deep learning. *Nature Biotechnology*, 33(8):831–838, 2015.

A. H. Alissa Park and L. S. Fan. Electrostatic charging phenomenon in gas-liquid-solid flow systems. *Chemical Engineering Science*, 62(1-2):371–386, 2007.

J. A. Almendros-Ibáñez, M. Fernández-Torrijos, M. Díaz-Heras, J. F. Belmonte, and C. Sobrino. A review of solar thermal energy storage in beds of particles: Packed and fluidized beds. *Solar Energy*, 192(January):193–237, 2019.

A. Anantharaman, R. A. Cocco, and J. W. Chew. Evaluation of correlations for minimum fluidization velocity (Umf) in gas-solid fluidization. *Powder Technology*, 323:454–485, 2018.

R. Ansart, P. García-Triñanes, B. Boissière, H. Benoit, J. P.K. Seville, and O. Simonin. Dense gas-particle suspension upward flow used as heat transfer fluid in solar receiver: PEPT experiments and 3D numerical simulations. *Powder Technology*, 307:25–36, 2017a.

R. Ansart, F. Vanni, B. Caussat, C. Ablitzer, and M. Brothier. Effects of reducing the reactor diameter on the dense gas–solid fluidization of very heavy particles: 3D numerical simulations. *Chemical Engineering Research and Design*, 117:575–583, 2017b.

J. Baeyens and D. Geldart. An investigation into slugging fluidized beds. *Chemical Engineering Science*, 29(1):255–265, 1974.

M. Bafrnec, J. Bena, and J. Beňa. Quantitative data on the lowering of electrostatic charge in a fluidized bed. *Chemical Engineering Science*, 27(5):1181–1183, 1972.

T. Baron, C. L. Briens, M. A. Bergougnou, J.D.Hazlett, and J. D. Hazlett. Electrostatic effects on entrainment from a fluidized bed. *Powder Technology*, 57(1):55–67, 1987.

R. Beetstra, M. A. van der Hoef, and J. A. M. Kuipers. Drag Force of Intermediate Reynolds Number Flow Past Mono- and Bidisperse Arrays of Spheres R. *AIChE Journal*, 53(2): 489–501, 2007.

H. T. Bi and J. R. Grace. Flow regime diagrams for gas-solid fluidization and upward transport. *International Journal of Multiphase Flow*, 21(6):1229–1236, 1995.

H. T. Bi, N. Ellis, I. A. Abba, and J. R. Grace. A state-of-the-art review of gas-solid turbulent fluidization. *Chemical Engineering Science*, 55:4789–4825, 2002.

X. T. Bi, A. Chen, and J. R. Grace. Monitoring Electrostatic Charges in Fluidized Beds Monitoring Electrostatic Charges in Fluidized Beds. In *The 12th International Conference on Fluidization - New Horizons in Fluidization Engineering*, pages 1001–1008. Curran Associates Inc, 2007.

A. Boëlle, G. Balzer, and O. Simonin. Second-order prediction of the particle-phase stress tensor of inelastic spheres in simple shear dense suspensions. In *ASME-Publications*, pages 9–18. ASME, 1995.

C. L. Briens, M. A. Bergougnou, I. I. Inculet, T. Baron, and J. D. Hazlett. Size distribution of particles entrained from fluidized beds: Electrostatic effects. *Powder Technology*, 70(1): 57–62, 1992.

A. Busciglio, G. Vella, G. Micale, and L. Rizzuti. Analysis of the bubbling behaviour of 2D gas solid fluidized beds. Part I. Digital image analysis technique. *Chemical Engineering Journal*, 140(1-3):398–413, 2008.

L. Calin, L. Caliap, V. Neamtu, R. Morar, A. Iuga, A. Samuila, and L. Dascalescu. Tribocharging of granular plastic mixtures in view of electrostatic separation. *IEEE Transactions on Industry Applications*, 44(4):1045–1051, 2008.

C. Capes and A. McIlhinney. The Pseudoparticulate Expansion of Screen-Packed Gas-Fluidized Beds. *AIChE Journal*, 14(6):917–922, 1968.

A. N. Chandran, S. S. Rao, and Y. B. Varma. Fluidized bed drying of solids. *AIChE Journal*, 36(1):29–38, 1990.

S. Chapman and T. G. Cowling. *The mathematical theory of non-uniform gases*. Cambridge University Press, 1990.

A. H. Chen, H. T. Bi, and J. R. Grace. Measurement of particle charge-to-mass ratios in a gas-solids fluidized bed by a collision probe. *Powder Technology*, 135-136:181–191, 2003.

K. S. Choi, K. T. Moon, J. H. Chung, X. Bi, and J. R. Grace. Electrostatic hazards of polypropylene powders in the fluidized bed reactor. In *IEEE International Conference on Industrial Engineering and Engineering Management*, pages 995–999. IEEE, 2011.

F. Chollet and Others. Keras, 2015.

J. Ciborowski and A. Wlodarski. On electrostatic effects in fluidized beds. *Chemical Engineering Science*, 17(1):23–32, 1962.

R. Cierniak. New neural network algorithm for image reconstruction from fan-beam projections. *Neurocomputing*, 72(13-15):3238–3244, 2009.

G. M. Colver. Bubble control in gas-fluidized beds with applied electric fields. *Powder Technology*, 17(1):9–18, 1977.

F. Depypere, J. G. Pieters, and K. Dewettinck. PEPT visualisation of particle motion in a tapered fluidised bed coater. *Journal of Food Engineering*, 93(3):324–336, 2009.

A. Di Renzo and F. P. Di Maio. Homogeneous and bubbling fluidization regimes in DEM-CFD simulations: Hydrodynamic stability of gas and liquid fluidized beds. *Chemical Engineering Science*, 62(1-2):116–130, 2007.

W. Dijkhuizen, G. A. Bokkers, N. G. Deen, M. v. S. Annaland, and J. A. M. Kuipers. Extension of PIV for Measuring Granular Temperature Field in Dense Fluidized Beds. *AIChE Journal*, 53(1):108–118, 2007.

J. Ding and D. Gidaspow. A bubbling fluidization model using kinetic theory of granular flow. *AIChE Journal*, 36(4):523–538, 1990.

K. Dong, Q. Zhang, Z. Huang, Z. Liao, J. Wang, and Y. Yang. Experimental investigation of electrostatic effect on bubble behaviors in gas-solid fluidized bed. *AIChE Journal*, 61 (4):1160–1171, 2015.

B. Du, Q. Marashdeh, W. Warsito, A.-H. A. Park, and L. S. Fan. Development of Electrical Capacitance Volume Tomography (ECVT) and Electrostatic Tomography (EST) for 3D Density Imaging of Fluidized Bed System. In *2007 ECI Conference on The 12th International Conference on Fluidization - New Horizons in Fluidization Engineering*, pages 473–480. Curran Associates Inc, 2007.

A. Efhaima and M. H. Al-Dahhan. Local time-averaged gas holdup in fluidized bed reactor using gamma ray computed tomography technique (CT). *International Journal of Industrial Chemistry*, 6(3):143–152, 2015.

S. Ergun and A. A. Orning. Fluid Flow through Randomly Packed Columns and Fluidized Beds. *Industrial and Engineering Chemistry*, 41(6):1179–1184, 1949.

M. Ernst, M. Sommerfeld, and S. Laín. Quantification of preferential concentration of colliding particles in a homogeneous isotropic turbulent flow. *International Journal of Multiphase Flow*, 117:163–181, 2019.

L. T. Fan, T.-C. Ho, S. Hiraoka, and W. P. Walawender. Pressure Fluctuations in a Fluidized Bed. *AIChE Journal*, 27(3):388–396, 1981.

L. Fasso, B. T. Chao, and S. L. Soo. Measurement of Electrostatic Charges and Concentration of Particles in the Bed. *Powder Technology*, 33:211–221, 1982.

P. Fede, O. Simonin, and A. Ingram. 3D numerical simulation of a lab-scale pressurized dense fluidized bed focussing on the effect of the particle-particle restitution coefficient and particle-wall boundary conditions. *Chemical Engineering Science*, 142:215–235, 2016.

E. Fehlberg. Classical fifth-, sixth-, seventh-, and eight-order Runge-Kutta Formulas with stepsize control. Technical report, 1968.

C. E. Floyd. An Artificial Neural Network for SPECT Image Reconstruction. *IEEE Transactions on Medical Imaging*, 10(3):485–487, 1991.

K. M. Forward. *Triboelectrification of Granular Materials*. PhD thesis, Case Western Reserve University, 2009.

F. Fotovat, R. Ansart, M. Hemati, O. Simonin, and J. Chaouki. Sand-assisted fluidization of large cylindrical and spherical biomass particles: Experiments and simulation. *Chemical Engineering Science*, 126:543–559, 2015.

F. Fotovat, T. A. Alsmari, J. R. Grace, and X. T. Bi. The relationship between fluidized bed electrostatics and entrainment. *Powder Technology*, 316:157–165, 2017a.

F. Fotovat, X. T. Bi, and J. R. Grace. Electrostatics in gas-solid fluidized beds: A review. *Chemical Engineering Science*, 173:303–334, 2017b.

R. O. Fox. On multiphase turbulence models for collisional fluid–particle flows. *Journal of Fluid Mechanics*, 742:368–424, 2014.

A. Gajewski. Investigation of the electrification of polypropylene particles during the fluidization process. *Journal of Electrostatics*, 16(2-3):219, 1985.

V. Ganzha. The electrification mechanism in a fluidized bed. *Journal of Engineering Physics*, 13(3):243–249, 1967.

H. Garbaa, L. Jackowska-Strumillo, K. Grudzien, and A. Romanowski. Neural network approach to ECT inverse problem solving for estimation of gravitational solids flow. In *Federated Conference on Computer Science and Information Systems*, pages 19–26. IEEE, 2014.

R. Gatignol. Faxen Formulae for a Rigid Particle in an Unsteady Non-Uniform Stokes Flow. *Journal de mécanique theorique et appliquée*, 2(2):143–160, 1983.

D. Geldart. Types of Gas Fluidization. *Powder Technology*, 7:285–292, 1973.

K. Gong, J. Guan, K. Kim, X. Zhang, J. Yang, Y. Seo, G. E. Fakhri, J. Qi, and Q. Li. Iterative PET Image Reconstruction Using Convolutional Neural Network Representation. *IEEE Transactions on Medical Imaging*, 38(3):675–685, 2019.

J. R. Grace, X. Bi, and N. Ellis. *Essentials of Fluidization Technology*. Wiley, 2020.

H. Grad. On the kinetic theory of rarefied gases. *Communications on Pure and Applied Mathematics*, 2(4):331–407, 1949.

Q. Guo, M. Ye, W. Yang, and Z. Liu. A machine learning approach for electrical capacitance tomography measurement of gas–solid fluidized beds. *AIChE Journal*, 65(6):e16583, 2019.

H. Gupta, K. H. Jin, H. Q. Nguyen, M. T. McCann, and M. Unser. CNN-Based Projected Gradient Descent for Consistent CT Image Reconstruction. *IEEE Transactions on Medical Imaging*, 37(6):1440–1453, 2018.

B. Hage and J. Werther. The guarded capacitance probe - A tool for the measurement of solids flow patterns in laboratory and industrial fluidized bed combustors. *Powder Technology*, 93(3):235–245, 1997.

M. A. Hassani, R. Zarghami, H. R. Norouzi, and N. Mostoufi. Numerical investigation of effect of electrostatic forces on the hydrodynamics of gas-solid fluidized beds. *Powder Technology*, 246:16–25, 2013.

C. He, X. T. Bi, and J. R. Grace. Simultaneous measurements of particle charge density and bubble properties in gas-solid fluidized beds by dual-tip electrostatic probes. *Chemical Engineering Science*, 123:11–21, 2015.

K. He, X. Zhang, S. Ren, and J. Sun. Deep Residual Learning for Image Recognition. In *Proceedings of the IEEE conference on computer vision and pattern recognition*, pages 770–778. IEEE, 2016.

G. Hendrickson. Electrostatics and gas phase fluidized bed polymerization reactor wall sheeting. *Chemical Engineering Science*, 61(4):1041–1064, 2006.

S. Hochreiter and J. Urgen Schmidhuber. Long Shortterm Memory. *Neural Computation*, 9 (8):17351780, 1997.

S. S. Hsiau and M. L. Hunt. Kinetic Theory Analysis of Flow-Induced Particle Diffusion and Thermal Conduction in Granular Material Flows. *Journal of Heat Transfer*, 115(3):541, 1993.

I. I. Inculet, M. A. Bergougnou, and J. D. Brown. Electrostatic Separation of Particles Below 40 μm in a Dilute Phase Continuous Loop. *IEEE Transactions on Industry Applications*, IA-13(4):370–373, 1977.

F. Jalalinejad, X. T. Bi, and J. R. Grace. Effect of electrostatic charges on single bubble in gas-solid fluidized beds. *International Journal of Multiphase Flow*, 44:15–28, 2012.

J. T. Jenkins and M. W. Richman. Grad's 13-moment system for a dense gas of inelastic spheres. *Archive for Rational Mechanics and Analysis*, 87(4):355–377, 1985.

J. T. Jenkins and S. B. Savage. A theory for the rapid flow of identical, smooth, nearly elastic, spherical particles. *Journal of Fluid Mechanics*, 130:187, 1983.

G. Jiménez-García, R. Aguilar-López, and R. Maya-Yescas. The fluidized-bed catalytic cracking unit building its future environment. *Fuel*, 90(12):3531–3541, 2011.

H. Johnsson and F. Johnsson. Measurements of local solids volume-fraction in fluidized bed boilers. *Powder Technology*, 115(1):13–26, 2001.

M. Kashyap, B. Chalermsinsuwan, and D. Gidaspow. Measuring turbulence in a circulating fluidized bed using PIV techniques. *Particuology*, 9(6):572–588, 2011.

K. Kiared, F. Larachi, M. Cassanello, and J. Chaouki. Flow Structure of the Solids in a Three-Dimensional Liquid Fluidized Bed. *Industrial and Engineering Chemistry Research*, 36(11):4695–4704, 1997.

C. W. Kiewiet, M. A. Bergougnou, J. D. Brown, and I. I. Inculet. Electrostatic Separation of Fine Particles in Vibrated Fluidized Beds. *IEEE Transactions on Industry Applications*, IA-14(6):526–530, 1978.

F. Kleijn van Willigen, J. R. van Ommen, J. van Turnhout, and C. M. van den Bleek. Bubble size reduction in electric-field-enhanced fluidized beds. *Journal of Electrostatics*, 63(6-10): 943–948, 2005.

J. Kolehmainen, A. Ozel, C. M. Boyce, and S. Sundaresan. Triboelectric charging of monodisperse particles in fluidized beds. *AIChE Journal*, 63(6):1872–1891, 2017.

J. Kolehmainen, A. Ozel, and S. Sundaresan. Eulerian modelling of gas-solid flows with triboelectric charging. *Journal of Fluid Mechanics*, 848(June):340–369, 2018.

J. Koornneef, M. Junginger, and A. Faaij. Development of fluidized bed combustion-An overview of trends, performance and cost. *Progress in Energy and Combustion Science*, 33 (1):19–55, 2007.

S. H. Kriebitzsch, M. A. Van Der Hoef, and J. A. M. Kuipers. Fully resolved simulation of a gas-fluidized bed: A critical test of DEM models. *Chemical Engineering Science*, 91:1–4, 2013.

A. Krizhevsky, I. Sutskever, and G. E. Hinton. Imagenet classification with deep convolutional neural networks. In *Advances in neural information processing systems*, pages 1097–1105. NIPS, 2012.

G. Kulah and O. Kaya. Investigation and scale-up of hot-melt coating of pharmaceuticals in fluidized beds. *Powder Technology*, 208(1):175–184, 2011.

D. Kunii and O. Levenspiel. *Fluidization Engineering*. Butterworth-Heinemann, 2003.

S. Langford, C. Wiggins, D. Tenpenny, and A. Ruggles. Positron Emission Particle Tracking (PEPT) for Fluid Flow Measurements. *Nuclear Engineering and Design*, 302:81–89, 2016.

F. Larachi, J. Chaouki, and G. Kennedy. 3-D Mapping of Solids Flow Fields in Multiphase Reactors with RPT. *AIChE Journal*, 41(2):439–443, 1995.

J. C. Laurentie, P. Traoré, and L. Dascalescu. Discrete element modeling of triboelectric charging of insulating materials in vibrated granular beds. *Journal of Electrostatics*, 71(6): 951–957, 2013.

J. Laviéville, E. Deutsch, and O. Simonin. Large eddy simulation of interactions between colliding particles and a homogeneous isotropic turbulence field. In *ASME-Publications*, pages 347–358. ASME, 1995.

G. S. Lee and S. D. Kim. Pressure fluctuations in turbulent fluidized beds. *Journal of Chemical Engineering of Japan*, 21(5):515–521, 1988.

J. Lei, Q. Liu, and X. Wang. Deep Learning-Based Inversion Method for Imaging Problems in Electrical Capacitance Tomography. *IEEE Transactions on Instrumentation and Measurement*, 67(9):2107–2118, 2018.

T. Li, Y. Zhang, and F. Hernández-Jiménez. Investigation of particle-wall interaction in a pseudo-2D fluidized bed using CFD-DEM simulations. *Particuology*, 25:10–22, 2016.

Y. Li, M. Jahanmiri, F. S. Careaga, C. Briens, F. Berruti, and J. McMillan. Applications of electrostatic probes in fluidized beds. *Powder Technology*, 370:64–79, 2020.

J. M. Link, L. A. Cuypers, N. G. Deen, and J. A. Kuipers. Flow regimes in a spout-fluid bed: A combined experimental and simulation study. *Chemical Engineering Science*, 60 (13):3425–3442, 2005.

H. Liu, A. Elkamel, A. Lohi, and M. Biglari. Computational fluid dynamics modeling of biomass gasification in circulating fluidized-bed reactor using the eulerian-eulerian approach. *Industrial and Engineering Chemistry Research*, 52(51):18162–18174, 2013.

M. Liu, Y. Zhang, H. Bi, J. R. Grace, and Y. Zhu. Non-intrusive determination of bubble size in a gas-solid fluidized bed: An evaluation. *Chemical Engineering Science*, 65(11): 3485–3493, 2010.

L. Lu, X. Liu, T. Li, L. Wang, W. Ge, and S. Benyahia. Assessing the capability of continuum and discrete particle methods to simulate gas-solids flow using DNS predictions as a benchmark. *Powder Technology*, 321:301–309, 2017.

N. MacCuaig, J. P. K. Seville, W. B. Gilboy, and R. Clift. Application of gamma-ray tomography to gas fluidized beds. *Applied Optics*, 24(23):4083, 1985.

M. E. Mainland and J. R. Welty. Use of optical probes to characterize bubble behavior in gas-solid fluidized beds. *AIChE Journal*, 41(2):223–228, 1995.

M. Manafi, R. Zarghami, and N. Mostoufi. Effect of electrostatic charge of particles on hydrodynamics of gas-solid fluidized beds. *Advanced Powder Technology*, 30(4):815–828, 2019a.

M. Manafi, R. Zarghami, and N. Mostoufi. Fluidization of electrically charged particles. *Journal of Electrostatics*, 99(February):9–18, 2019b.

Q. Marashdeh. *Advances in Electrical Capacitance Tomography*. PhD thesis, Ohio State University, 2006.

S. Matsusaka and H. Masuda. Electrostatics of particles. *Advanced Powder Technology*, 14 (2):143–166, 2003.

M. R. Maxey and J. J. Riley. Equation of motion for a small rigid sphere in a nonuniform flow. *The Physics of Fluids*, 26(10):883–51704, 1983.

P. Mehrani, H. T. Bi, and J. R. Grace. Electrostatic charge generation in gas-solid fluidized beds. *Journal of Electrostatics*, 63(2):165–173, 2005.

T. Mikolov, I. Sutskever, K. Chen, G. Corrado, and J. Dean. Distributed representations ofwords and phrases and their compositionality. In *Advances in Neural Information Processing Systems*, pages 1–9. NIPS, 2013.

B. Milici, M. D. Marchis, G. Sardina, and E. Napoli. Effects of roughness on density-weighted particle statistics in turbulent channel flows. *Journal of Fluid Mechanics*, 739:465–478, 2014.

C. O. Miller and A. K. Logwinuk. Fluidization Studies of Solid Particles. *Industrial and Engineering Chemistry*, 43(5):1220–1226, 1951.

C. Montilla, R. Ansart, and O. Simonin. Modelling of the mean electric charge transport equation in a mono-dispersed gas-particle flow. *Journal of Fluid Mechanics*, 902:(A12)1–26, 2020.

W. O. Moughrabiah, J. R. Grace, and X. T. Bi. Effects of pressure, temperature, and gas velocity on electrostatics in gas-solid fluidized beds. *Industrial and Engineering Chemistry Research*, 48(1):320–325, 2009.

S. Movahedirad, A. M. Dehkordi, E. A. Molaei, M. Haghi, M. Banaei, and J. A. M. Kuipers. Bubble splitting in a pseudo-2D gas-solid fluidized bed for geldart B-type particles. *Chemical Engineering and Technology*, 37(12):2096–2102, 2014.

R. Mudde. Bubbles in a Fluidized Bed: A Fast X-Ray Scanner. *AIChE Journal*, 57(10): 2684–2690, 2010a.

R. F. Mudde. Time-resolved X-ray tomography of a fluidized bed. *Powder Technology*, 199 (1):55–59, 2010b.

Y. Nasro Allah. *Experimental and numerical investigation of electrostatic charges in gas-solid fluidized beds*. PhD thesis, Toulouse-INP, 2019.

H. Neau, M. Pigou, P. Fede, R. Ansart, C. Baudry, N. Mérigoux, J. Laviéville, Y. Fournier, N. Renon, and O. Simonin. Massively parallel numerical simulation using up to 36,000 CPU cores of an industrial-scale polydispersed reactive pressurized fluidized bed with a mesh of one billion cells. *Powder Technology*, 366:906–924, 2020.

A. Ozel, J. C. Brändle de Motta, M. Abbas, P. Fede, O. Masbernat, S. Vincent, J. L. Estivalezes, and O. Simonin. Particle resolved direct numerical simulation of a liquid–solid fluidized bed: Comparison with experimental data. *International Journal of Multiphase Flow*, 89:228–240, 2017.

D. J. Parker. Positron emission particle tracking and its application to granular media. *Review of Scientific Instruments*, 88(5):051803–1–8, 2017.

D. J. Parker, C. J. Broadbent, P. Fowles, M. R. Hawkesworth, and P. McNeil. Positron emission particle tracking - a technique for studying flow within engineering equipment. *Nuclear Inst. and Methods in Physics Research, A*, 326(3):592–607, 1993.

C. Pei, C. Y. Wu, D. England, S. Byard, H. Berchtold, and M. Adams. Numerical analysis of contact electrification using DEM-CFD. *Powder Technology*, 248:34–43, 2013.

C. Pei, C. Y. Wu, and M. Adams. DEM-CFD analysis of contact electrification and electrostatic interactions during fluidization. *Powder Technology*, 304(September):208–217, 2016.

M. Punčochář and J. Drahoš. Origin of pressure fluctuations in fluidized beds. *Chemical Engineering Science*, 60(5):1193–1197, 2005.

M. Punčochář, J. Drahoš, J. Cermak, and K. Selucky. Evaluation of minimum fluidizing velocity in gas fluidized bed from pressure fluctuations. *Chemical Engineering Communications*, 35(1-6):81–87, 1985.

M. Rasouli, F. Bertrand, and J. Chaouki. A multiple radioactive particle tracking technique to investigate particulate flows. *AIChE Journal*, 61(2):384–394, 2015.

M. Ray, F. Chowdhury, A. Sowinski, P. Mehrani, and A. Passalacqua. An Euler-Euler model for mono-dispersed gas-particle flows incorporating electrostatic charging due to particle-wall and particle-particle collisions. *Chemical Engineering Science*, 197:327–344, 2019.

M. Ray, F. Chowdhury, A. Sowinski, P. Mehrani, and A. Passalacqua. Eulerian modeling of charge transport in bi-disperse particulate flows due to triboelectrification. *Physics of Fluids*, 32(2):023302, 2020.

R. G. Rokkam, R. O. Fox, and M. E. Muhle. Computational fluid dynamics and electrostatic modeling of polymerization fluidized-bed reactors. *Powder Technology*, 203(2):109–124, 2010.

R. G. Rokkam, A. Sowinski, R. O. Fox, P. Mehrani, and M. E. Muhle. Computational and experimental study of electrostatics in gas-solid polymerization fluidized beds. *Chemical Engineering Science*, 92:146–156, 2013.

M. Rüdisüli, T. J. Schildhauer, S. M. Biollaz, and J. Ruud van Ommen. Bubble characterization in a fluidized bed by means of optical probes. *International Journal of Multiphase Flow*, 41:56–67, 2012.

F. Sabatier, R. Ansart, H. Zhang, J. Baeyens, and O. Simonin. Experiments support simulations by the NEPTUNE_CFD code in an Upflow Bubbling Fluidized Bed reactor. *Chemical Engineering Journal*, 385(June 2019):123568, 2020.

M. Sakiz and S. Olivier. Numerical experiments and modelling of non-equilibrium effects in dilute granular flows. In *21st Int. Symp. on Rarefied Gas Dynamics*, pages 287–294, 1999.

M. Sakiz and O. Simonin. Development and validation of continuum particle wall boundary conditions using lagrangian simulation of a vertical gas/solid channel flow. In *3rd ASME/JSME Joint Fluids Engineering Conference*, pages 1–8. ASME, 1999.

F. Salama, A. Sowinski, K. Atieh, and P. Mehrani. Investigation of electrostatic charge distribution within the reactor wall fouling and bulk regions of a gas-solid fluidized bed. *Journal of Electrostatics*, 71(1):21–27, 2013.

L. B. Schein, M. LaHa, and D. Novotny. Theory of insulator charging. *Physics Letters A*, 167(1):79–83, 1992.

J. Schlemper, J. Caballero, J. V. Hajnal, A. N. Price, and D. Rueckert. A Deep Cascade of Convolutional Neural Networks for Dynamic MR Image Reconstruction. *IEEE Transactions on Medical Imaging*, 37(2):491–503, 2018.

S. Schneiderbauer, S. Puttinger, S. Pirker, P. Aguayo, and V. Kanellopoulos. CFD modeling and simulation of industrial scale olefin polymerization fluidized bed reactors. *Chemical Engineering Journal*, 264:99–112, 2015.

Y. T. Shih, D. Gidaspow, and D. Wasan. Hydrodynamics of electroluidization: Separation of pyrites from coal. *AIChE Journal*, 33(8):1322–1333, 1987.

O. Simonin, E. Deutsch, and M. Boivin. Large Eddy Simulation and Second-Moment Closure Model of Particle Fluctuating Motion in Two-Phase Turbulent Shear Flows. In *Turbulent Shear Flows 9*, pages 85–115. Springer, 1995.

O. Simonin, P. Février, and J. Laviéville. On the spatial distribution of heavy-particle velocities in turbulent flow: from continuous field to particulate chaos. *Journal of Turbulence*, 3(40):1–18, 2002.

D. Song and P. Mehrani. Mechanism of particle build-up on gas-solid fluidization column wall due to electrostatic charge generation. *Powder Technology*, 316:166–170, 2017.

D. Song, F. Salama, J. Matta, and P. Mehrani. Implementation of Faraday cup electrostatic charge measurement technique in high-pressure gas-solid fluidized beds at pilot-scale. *Powder Technology*, 290:21–26, 2016.

A. Sowinski, F. Salama, and P. Mehrani. New technique for electrostatic charge measurement in gas-solid fluidized beds. *Journal of Electrostatics*, 67(4):568–573, 2009.

A. Sowinski, L. Miller, and P. Mehrani. Investigation of electrostatic charge distribution in gas-solid fluidized beds. *Chemical Engineering Science*, 65(9):2771–2781, 2010.

A. Sowinski, A. Mayne, and P. Mehrani. Effect of fluidizing particle size on electrostatic charge generation and reactor wall fouling in gas-solid fluidized beds. *Chemical Engineering Science*, 71:552–563, 2012.

G. Tardos and R. Pfeffer. A method to measure electrostatic charge on a granule in a fluidized bed. *Chemical Engineering Communications*, 4(6):665–671, 1980.

W. P. Taruno, M. R. Baidillah, R. I. Sulaiman, M. F. Ihsan, S. E. Fatmi, A. H. Muhtadi, F. Haryanto, and M. Aljohani. 4D brain activity scanner using Electrical Capacitance Volume Tomography (ECVT). In *Proceedings - International Symposium on Biomedical Imaging*, pages 1006–1009. IEEE, 2013.

P. Traoré, J. C. Laurentie, and L. Dascalescu. An efficient 4 way coupling CFD-DEM model for dense gas-solid particulate flows simulations. *Computers and Fluids*, 113:65–76, 2015.

O. Trnka, V. Veselý, M. Hartman, and Z. Beran. Identification of the state of a fluidized bed by pressure fluctuations. *AIChE Journal*, 46(3):509–514, 2000.

M. Van de Velden, J. Baeyens, J. P. K. Seville, and X. Fan. The solids flow in the riser of a Circulating Fluidised Bed (CFB) viewed by Positron Emission Particle Tracking (PEPT). *Powder Technology*, 183(2):290–296, 2008.

J. Van Der Schaaf, J. C. Schouten, F. Johnsson, and C. M. Van Den Bleek. Non-intrusive determination of bubble and slug length scales in fluidized beds by decomposition of the power spectral density of pressure time series. *International Journal of Multiphase Flow*, 28(5):865–880, 2002.

F. Vanni, B. Caussat, C. Ablitzer, and M. Brothier. Effects of reducing the reactor diameter on the fluidization of a very dense powder. *Powder Technology*, 277:268–274, 2015.

A. Vaswani, N. Shazeer, N. Parmar, J. Uszkoreit, L. Jones, A. N. Gomez, Ł. Kaiser, and I. Polosukhin. Attention is all you need. In *Advances in Neural Information Processing Systems*, pages 5999–6009. NIPS, 2017.

V. Venkatasubramanian. The promise of artificial intelligence in chemical engineering: Is it here, finally? *AIChE Journal*, 65(2):466–478, 2019.

K. Vollmari, R. Jasevičius, and H. Kruggel-Emden. Experimental and numerical study of fluidization and pressure drop of spherical and non-spherical particles in a model scale fluidized bed. *Powder Technology*, 291:506–521, 2016.

F. Wang, Q. Marashdeh, A. Wang, and L. S. Fan. Electrical capacitance volume tomography imaging of three-dimensional flow structures and solids concentration distributions in a riser and a bend of a gas-solid circulating fluidized bed. *Industrial and Engineering Chemistry Research*, 51(33):10968–10976, 2012.

Q. Wang, K. D. Squires, and O. Simonin. Large eddy simulation of turbulent gas-solid flows in a vertical channel and evaluation of second-order models. *International Journal of Heat and Fluid Flow*, 19(5):505–511, 1998.

S. Wang, H. Lu, F. Zhao, and G. Liu. CFD studies of dual circulating fluidized bed reactors for chemical looping combustion processes. *Chemical Engineering Journal*, 236:121–130, 2014.

W. Warsito and L.-S. Fan. Neural network based multi-criterion optimization image reconstruction technique for imaging two- and three-phase flow systems using electrical capacitance tomography. *Measurement Science and Technology*, 12(12):2198–2210, 2001.

J. M. Weber and J. S. Mei. Bubbling fluidized bed characterization using electrical capacitance volume tomography (ECVT). *Powder Technology*, 242:40–50, 2013.

J. M. Weber, K. J. Layfield, D. T. Van Essendelft, and J. S. Mei. Fluid bed characterization using electrical capacitance volume tomography (ECVT), compared to CPFD software's barracuda. *Powder Technology*, 250:138–146, 2013.

M. W. Weber and C. M. Hrenya. Computational study of pressure-drop hysteresis in fluidized beds. *Powder Technology*, 177(3):170–184, 2007.

C. Y. Wen and R. F. Hashinger. Elutriation of solid particles from a dense-phase fluidized bed. *AIChE Journal*, 6(2):220–226, 1960.

J. Werther and B. Hage. A fiber-optical sensor for high-temperature application in fluidized bed combustion. In *Fluidization VIII, International Symposium of the Engineering Foundation*, pages 577–584. Engineering Foundation, 1995.

J. Werther, B. Hage, and C. Rudnick. A comparison of laser Doppler and single-fibre reflection probes for the measurement of the velocity of solids in a gas-solid circulating fluidized bed. *Chemical Engineering and Processing: Process Intensification*, 35(5):381–391, 1996.

V. Wiesendorf and J. Werther. Capacitance probes for solids volume concentration and velocity measurements in industrial fluidized bed reactors. *Powder Technology*, 110(1-2): 143–157, 2000.

A. Wolny and W. Kaźmierczak. Triboelectrification in fluidized bed of polystyrene. *Chemical Engineering Science*, 44(11):2607–2610, 1989.

A. Wolny and W. Kaźmierczak. The influence of static electrification on dynamics and rheology of fluidized bed. *Chemical Engineering Science*, 48(20):3529–3534, 1993.

C. Xie, A. Plaskowski, and M. Beck. 8-electrode capacitance system for two-component flow identification. Part 1: Tomographic flow imaging. *IEE Proceedings A (Physical Science, Measurement and Instrumentation, Management and Education)*, 136(4):173–183, 1989.

G. Xu, T. Murakami, T. Suda, Y. Matsuzawa, and H. Tani. The superior technical choice for dual fluidized bed gasification. *Industrial and Engineering Chemistry Research*, 45(7): 2281–2286, 2006.

W. C. Yang. Modification and re-interpretation of Geldart's classification of powders. *Powder Technology*, 171(2):69–74, 2007.

W. Q. Yang, D. M. Spink, T. a. York, and H. McCann. An image-reconstruction algorithm based on Landweber's iteration method for electrical-capacitance tomography. *Measurement Science and Technology*, 10(11):1065–1069, 1999.

Y. Yang, Z. Huang, W. Zhang, J. Wang, M. Lungu, Z. Liao, F. Wang, Y. Yang, Y. Yan, and J. Yang. Effects of agglomerates on electrostatic behaviors in gas-solid fluidized beds. *Powder Technology*, 287:139–151, 2016.

Y. Yang, C. Zi, Z. Huang, J. Wang, M. Lungu, Z. Liao, Y. Y. Yang, and H. Su. CFD-DEM investigation of particle elutriation with electrostatic effects in gas-solid fluidized beds. *Powder Technology*, 308:422–433, 2017.

T. Yehuda and H. Kalman. Geldart classification for wet particles. *Powder Technology*, 362: 288–300, 2020.

J. Yerushalmi and N. T. Cankurt. Further Studies of the Regimes of Fluidization. *Powder Technology*, 24(2):187–205, 1979.

K. Zainal-Mokhtar and J. Mohamad-Saleh. An oil fraction neural sensor developed using electrical capacitance tomography sensor data. *Sensors (Switzerland)*, 13(9):11385–11406, 2013.

M. Zastawny, G. Mallouppas, F. Zhao, and B. van Wachem. Derivation of drag and lift force and torque coefficients for non-spherical particles in flows. *International Journal of Multiphase Flow*, 39:227–239, 2012.

D. Z. Zhang and A. Prosperetti. Averaged Equations for Inviscid Disperse Two-Phase Flowf. *Journal of Fluid Mechanics*, 267:185–219, 1994.

M. Zhang, H. Wu, Q. Lu, Y. Sun, and G. Song. Heat transfer characteristics of fluidized bed heat exchanger in a 300MW CFB boiler. *Powder Technology*, 222:1–7, 2012.

M. H. Zhang, K. W. Chu, F. Wei, and A. B. Yu. A CFD-DEM study of the cluster behavior in riser and downer reactors. *Powder Technology*, 184(2):151–165, 2008a.

Y. Zhang, C. Lu, and M. Shi. A practical method to estimate the bed height of a fluidized bed of fine particles. *Chemical Engineering and Technology*, 31(12):1735–1742, 2008b.

Y. F. Zhang, Y. Yang, and H. Arastoopour. Electrostatic Effect on the Flow Behavior of a Dilute Gas/Cohesive Particle Flow System. *AIChE Journal*, 42(6):1590–1599, 1996.

H. Zhao, G. S. Castle, I. I. Inculet, and A. G. Bailey. Bipolar charging of poly-disperse polymer powders in fluidized beds. *IEEE Transactions on Industry Applications*, 39(3): 612–618, 2003.

J. Zheng, J. Li, Y. Li, and L. Peng. A benchmark dataset and deep learning-based image reconstruction for electrical capacitance tomography. *Sensors*, 18(11):3701, 2018.

Y. Zhou, C. Ren, J. Wang, Y. Yang, and K. Dong. Effect of hydrodynamic behavior on electrostatic potential distribution in gas-solid fluidized bed. *Powder Technology*, 235: 9–17, 2013.